

AD-A265 129



Office of Naval Research

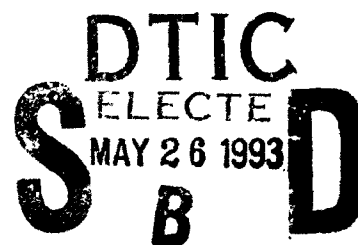
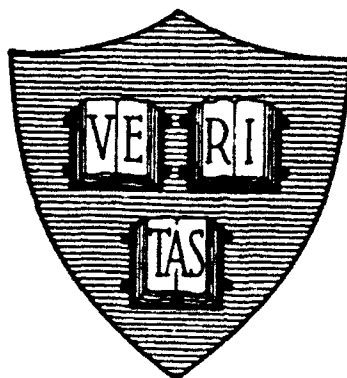
National Sciences Foundation Grant DMR-89-12927

National Sciences Foundation Grant DMR-29-07956

Grant N00014-89-J-1023

Grant N00014-89-J-1565

**MEASUREMENTS ON TWO-DIMENSIONAL ARRAYS OF
MESOSCOPIC JOSEPHSON JUNCTIONS**



By

Thomas Steven Tighe

February 1993

Technical Report No. 35

This document has been approved for public release and sale; its distribution is unlimited. Reproduction in whole or in part is permitted by the U.S. Government.

**Division of Applied Sciences
Harvard University · Cambridge, Massachusetts**

93 5 25 132

93-11694



REPORT DOCUMENTATION PAGE

Form Approved
OMB No. 0704-0188

1a. REPORT SECURITY CLASSIFICATION Unclassified			1b. RESTRICTIVE MARKINGS		
2a. SECURITY CLASSIFICATION AUTHORITY N/A			3. DISTRIBUTION/AVAILABILITY OF REPORT Unclassified/Unlimited		
2b. DECLASSIFICATION/DOWNGRADING SCHEDULE N/A					
4. PERFORMING ORGANIZATION REPORT NUMBER(S) Technical Report No. 35			5. MONITORING ORGANIZATION REPORT NUMBER(S) Office of Naval Research		
6a. NAME OF PERFORMING ORGANIZATION Harvard University		6b. OFFICE SYMBOL (if applicable)		7a. NAME OF MONITORING ORGANIZATION Office of Naval Research	
6c. ADDRESS (City, State, and ZIP Code) Division of Applied Sciences Harvard University Cambridge, MA 02138			7b. ADDRESS (City, State, and ZIP Code) 800 N. Quincy Street Arlington, VA 22217		
8a. NAME OF FUNDING/SPONSORING ORGANIZATION Office of Naval Research		8b. OFFICE SYMBOL (if applicable)		9. PROCUREMENT INSTRUMENT IDENTIFICATION NUMBER N00014-89-J-1023	
8c. ADDRESS (City, State, and ZIP Code) 800 N. Quincy St. Arlington, VA 22217			10. SOURCE OF FUNDING NUMBERS		
			PROGRAM ELEMENT NO.	PROJECT NO.	TASK NO.
			WORK UNIT ACCESSION NO.		
11. TITLE (Include Security Classification) Measurements on Two-Dimensional Arrays of Mesoscopic Josephson Junctions					
12. PERSONAL AUTHOR(S) Thomas Steven Tighe					
13a. TYPE OF REPORT Interim (Technical)		13b. TIME COVERED FROM _____ TO _____		14. DATE OF REPORT (Year, Month, Day) February 1993	
				15. PAGE COUNT 176	
16. SUPPLEMENTARY NOTATION					
17. COSATI CODES			18. SUBJECT TERMS (Continue on reverse if necessary and identify by block number)		
FIELD	GROUP	SUB-GROUP			
19. ABSTRACT (Continue on reverse if necessary and identify by block number) See reverse.					
20. DISTRIBUTION/AVAILABILITY OF ABSTRACT <input checked="" type="checkbox"/> UNCLASSIFIED/UNLIMITED <input type="checkbox"/> SAME AS RPT. <input type="checkbox"/> DTIC USERS			21. ABSTRACT SECURITY CLASSIFICATION Unclassified		
22a. NAME OF RESPONSIBLE INDIVIDUAL Prof. Michael Tinkham, Director			22b. TELEPHONE (Include Area Code) (617) 495-3735		22c. OFFICE SYMBOL

19. Abstract

We report measurements on two-dimensional arrays of Josephson junctions with junction sizes down to 60 nm. Due to their small size, these junctions belong to the class of *mesoscopic* systems; they show behavior which reveals the underlying quantum mechanical properties. Two energies characterize the junctions, the Josephson energy E_J and the charging energy E_c . Arrays in which $E_J \gg E_c$ are superconducting around zero bias and at zero temperature, while arrays in which $E_c \gg E_J$, called charging arrays, are instead insulating. This is the basis of the superconductor-to-insulator (S-I) transition.

Specifically, we measure the transport properties of arrays on both sides of the S-I transition. On the superconducting side ($E_J \gg E_c$), we study vortices and vortex motion, i.e., pinning barriers, depinning currents, vortex lattices, and vortex-vortex interactions. We experimentally discovered a new vortex damping mechanisms; moving vortices transfer energy to the junctions over which they travel in the form of a "wake."

In the charging limit ($E_c \gg E_J$), we study the array conduction properties, dominated by solitons and their motion (a soliton is a "dressed" charge). At zero temperature, we measure a Coulomb blockade, denoted by a threshold voltage V_t below which no current flows. At higher temperatures, we measure conduction within the blockade region, caused by the creation and disassociation of soliton-antisoliton pairs. Instead of the predicted Kosterlitz-Thouless-Berezinskii pair unbinding transition, we find the data to better fit a simple thermal activation model with activation barriers $0.25 E_c$ in the normal state and $0.25 E_c$ plus the superconducting energy gap in the superconducting state.

We also study arrays in which E_J is on the order of E_c , and measure a mixture of both superconducting and charging behaviors by finding a Coulomb blockade region within the "supercurrent" branch. In addition, we irradiate the charging arrays with microwaves, looking for single-electron tunneling (SET) oscillations. We did not measure any evidence for SET oscillations, but instead found a shift of the curves to lower voltages, with the amount of shift proportional to the *amplitude* of the rf signal.

Accession For		<input checked="checked" type="checkbox"/>
NTIS Grant		<input type="checkbox"/>
DTIC Tab		<input type="checkbox"/>
Unannounced		
Justification		
By	Distribution/	
	Availability Codes	
Dist	Avail and/or	
A-1	Special	

1987-01-01 0

Office of Naval Research

National Sciences Foundation Grant DMR-89-12927

National Sciences Foundation Grant DMR-92-07956

Grant N00014-89-J-1023

Grant N00014-89-J-1565

**MEASUREMENTS ON TWO-DIMENSIONAL ARRAYS OF
MESOSCOPIC JOSEPHSON JUNCTIONS**

by

Thomas Steven Tighe

Technical Report No. 35

Reproduction in whole or in part is permitted for any purpose of the United States Government. Approved for public release: distribution unlimited.

February 1993

The research reported in this document was made possible through support extended the Division of Applied Sciences, Harvard University, by the National Sciences Foundation Grants DMR-89-12927 and DMR-92-07956 and by the Office of Naval Research, under Grants N00014-89-J-1023, N00014-89-J-1565.

Division of Applied Sciences
Harvard University · Cambridge, Massachusetts

ABSTRACT

We report measurements on two-dimensional arrays of Josephson junctions with junction sizes down to 60 nm by 60 nm. Due to their small size, these junctions belong to the class of *mesoscopic* systems; they show behavior which reveals the underlying quantum mechanical properties. Two energies characterize the junctions, the Josephson energy E_J and the charging energy E_C . Arrays in which $E_J \gg E_C$ are superconducting around zero bias and at zero temperature, while arrays in which $E_C \gg E_J$, called charging arrays, are instead insulating. This is the basis of the superconductor-to-insulator (S-I) transition.

Specifically, we measure the transport properties of arrays on both sides of the S-I transition. On the superconducting side ($E_J \gg E_C$), we study vortices and vortex motion, *i.e.*, pinning barriers, depinning currents, vortex lattices, and vortex-vortex interactions. We experimentally discovered a new vortex damping mechanism; moving vortices transfer energy to the junctions over which they travel in the form of a “wake”.

In the charging limit ($E_C \gg E_J$), we study the array conduction properties, dominated by solitons and their motion (a soliton is a “dressed” charge). At zero temperature, we measure a Coulomb blockade, denoted by a threshold voltage V_t below which no current flows. At higher temperatures, we measure conduction within the blockade region, caused by the creation and disassociation of soliton-antisoliton pairs. Instead of the predicted Kosterlitz-Thouless-Berezinskii pair unbinding transition, we find the data to better fit a simple thermal activation model with activation barriers $0.25 E_C$ in the normal state and $0.25 E_C$ *plus* the superconducting energy gap in the superconducting state.

We also study arrays in which E_J is on the order of E_C , and measure a mixture of both superconducting and charging behaviors by finding a Coulomb blockade region within the “supercurrent” branch. In addition, we irradiate the charging arrays with microwaves,

looking for single-electron tunneling (SET) oscillations. We did not measure any evidence for SET oscillations, but instead found a shift of the curves to lower voltages, with the amount of shift proportional to the *amplitude* of the rf signal.

TABLE OF CONTENTS

ABSTRACT	iii
TABLE OF CONTENTS	v
LIST OF FIGURES	vii
LIST OF TABLES	xi
CHAPTER 1 INTRODUCTION	1
CHAPTER 2 THEORETICAL OVERVIEW	14
2.1 Superconducting Junctions	14
2.1.1 Single Junction Hamiltonian	
2.1.2 Single Junction Equation of Motion	
2.1.3 The RCSJ Model	
2.1.4 The Washboard Model	
2.2 Superconducting Arrays	21
2.2.1 Array Hamiltonian	
2.2.2 Eggcrate Potential	
2.2.3 Vortex Equation of Motion	
2.2.4 Commensuration Effects	
2.3 Charging Junctions	28
2.3.1 Double Junction Hamiltonian	
2.3.2 Double Junction I-V Curves	
2.4 Charging Arrays	34
2.4.1 Capacitive Energy of a 2D Array	
2.4.2 Solitons	
2.4.3 I-V Characteristics and Commensuration Effects	
CHAPTER 3 DESCRIPTION OF EXPERIMENT	39
3.1 Array Design	39
3.2 Fabrication	46
3.2.1 Photolithography	
3.2.2 Electron-beam Lithography	
3.2.3 Evaporation	
3.3 Measurement	54
3.3.1 DC Set-Up	
3.3.2 Microwave Set-Up	
3.4 Refrigeration	60

CHAPTER 4 MEASUREMENTS AND DISCUSSION ON

SUPERCONDUCTING ARRAYS	66
4.1 Basic Array Characteristics.....	66
4.1.1 I-V Curves	
4.1.2 Magnetic Field Response	
4.1.3 Junction Inhomogeneity	
4.2 Results of Measurements	79
4.2.1 Critical and Depinning Currents	
4.2.2 Thermal Activation Measurements of Eb	
4.2.3 Vortex Viscosity--Theory	
4.2.4 Vortex Viscosity--Experiment	
4.2.5 Vortex Critical Velocity	

CHAPTER 5 MEASUREMENTS AND DISCUSSION ON TRANSITIONAL

ARRAYS.....	92
5.1 General Results of Measurements.....	93
5.2 Discussion of Results	94
5.2.1 Sample #6	
5.2.2 Sample #7	
5.2.3 Comparison of the Two Samples	

CHAPTER 6 MEASUREMENTS AND DISCUSSION ON CHARGING

ARRAYS.....	108
6.1 General Results	108
6.2 Determination of Parameters	114
6.2.1 Determination of C	
6.2.2 Determination of Co	
6.3 Discussion of Results	119
6.3.1 Threshold Voltage V_t	
6.3.2 Thermal Activation--Measurements	
6.3.3 Thermal Activation--Theory	

CHAPTER 7 MICROWAVE IRRADIATION OF CHARGING ARRAYS..... 129

7.1 General Results	129
7.2 Discussion of Results	140

CHAPTER 8 CONCLUSION AND SUGGESTIONS FOR FUTURE

RESEARCH.....	145
---------------	-----

REFERENCES.....	149
-----------------	-----

APPENDIX A	SCHEMATIC DRAWINGS OF DIAMOND ARRAYS	154
APPENDIX B	LINE LOSS IN MICROWAVE INJECTION SET-UP IN DILUTION REFRIGERATOR.....	155
APPENDIX C	LIST OF NAMES USED TO IDENTIFY SAMPLES	161
ACKNOWLEDGMENTS.....		162

LIST OF FIGURES

- Fig. 1-1 Schematic drawing of Josephson junction array.
- Fig. 1-2 Schematic drawing of a Josephson junction.
- Fig. 1-3 (a) Model I-V curve for single superconducting junction.
- (b) Model I-V curve for two charging junctions in series.
- Fig. 1-4 (a) I-V curve for sample #4.
- (b) I-V curve for sample #10.
- Fig. 1-5 Schematic drawing of vortex currents.
- Fig. 1-6 Schematic drawing of soliton.
- Fig. 1-7 (a) I-V curve showing definition of R_o in superconducting arrays.
- (b) I-V curve showing definition of R_o in charging arrays.
- (c) R_o vs. T/T_c for samples #1 - #10.
- Fig. 2-1 Schematic drawing of junction in RCSJ model.
- Fig. 2-2 Washboard model and corresponding I-V curves.
- Fig. 2-3 Island phases which give rise to a vortex.
- Fig. 2-4 Eggcrate potential.
- Fig. 2-5 (a) Vortex lattice for $f = 1/2$.
- (b) Vortex lattice for $f = 1/3$.
- Fig. 2-6 Schematic drawing of voltage biased double junction system.
- Fig. 2-7 Energy level diagram for $V < V_f$.
- Fig. 2-8 Energy level diagram for $V > V_f$.
- Fig. 2-9 Model I-V curves for double junction system.
- Fig. 2-10 Soliton island voltages.
- Fig. 3-1 Array design.
- Fig. 3-2 Transition between tin and aluminum unit cells.

- Fig. 3-3 (a) Picture of array #4.
 (b) Picture of gold array which simulates aluminum arrays, #7 - #10.
- Fig. 3-4 (a) Picture of unit cell, sample #4.
 (b) Picture of gold array unit cell.
- Fig. 3-5 (a) Picture of junction, sample #4.
 (b) Picture of junction, gold array.
- Fig. 3-6 Schematic drawing of pad design.
- Fig. 3-7 E-beam resist system.
- Fig. 3-8 Top view of exposed and developed e-beam resist.
- Fig. 3-9 (a) First evaporation.
 (b) Second evaporation.
- Fig. 3-10 Schematic drawing of dilution refrigerator slug.
- Fig. 3-11 (a) Circuit diagram for current biased set-up.
 (b) Circuit diagram for voltage biased set-up.
- Fig. 3-12 Circuit diagram for voltage source.
- Fig. 3-13 Schematic drawing of microwave injection set-up.
- Fig. 4-1 I-V curve for sample #4.
- Fig. 4-2 (a) I-V curve for sample #5 at a temperature of $T = 2.6$ K.
 (b) I-V curve for sample #5 at a temperature of $T = 1.8$ K.
 (c) I-V curve for sample #5 at a temperature of $T = 1.2$ K.
- Fig. 4-3 Critical current vs. T .
- Fig. 4-4 Expanded view of "supercurrent" branch for sample #4.
- Fig. 4-5 I-V curve for sample #4 showing definition of R_0 .
- Fig. 4-6 R_0 vs. T for samples #1 - #5.
- Fig. 4-7 Change in R_0 vs. frustration for sample #4.
- Fig. 4-8 I_{c1} vs. frustration for sample #4.
- Fig. 4-9 $R_0 T$ vs. $1/T$ for sample #4.

- Fig. 4-10 Moving vortex and wake.
- Fig. 4-11 Simulated I-V curves for single vortex in an array.
- Fig. 4-12 Scaled I-V curves for sample #4 at different values of frustration.
- Fig. 4-13 Numerical simulations of vortex-antivortex generation in a wake.
- Fig. 5-1 (a) I-V curve for sample #6 at a temperature of $T < 50$ mK.
 (b) Close-up view of "supercurrent" branch, sample #6 at $T < 50$ mK.
- Fig. 5-2 (a) I-V curve for sample #7 at a temperature of $T = 15$ mK.
 (b) Close up view of Coulomb blockade region, sample #7, $T = 15$ mK.
- Fig. 5-3 R_o vs. T for sample #6.
- Fig. 5-4 R_o vs. T for sample #7.
- Fig. 5-5 Dependence of Coulomb gap on frustration, sample #7, $T = 15$ mK.
- Fig. 5-6 R_o vs. T for sample #7 at different values of frustration.
- Fig. 5-7 Superconductor-to-insulator phase diagram by Fazio and Schön (1991).
- Fig. 5-8 (a) Comparison of R_o vs. T for samples #6 and #7.
 (b) Expanded view of the low-temperature region of (a).
- Fig. 6-1 (a) I-V curve for sample #10 in the normal state at $T = 15$ mK.
 (b) I-V curve for sample #10 in the superconducting state at $T = 15$ mK.
- Fig. 6-2 Coulomb blockade regions for sample #10 in the normal and superconducting states, at a temperature of $T = 15$ mK.
- Fig. 6-3 I-V curve for sample #10 in the superconducting state at $T = 300$ mK.
- Fig. 6-4 Change in V_l vs. V_g , sample #10 at $T = 15$ mK.
- Fig. 6-5 G_o vs. $1/T$ for samples #9 and #10 in the normal state.
- Fig. 6-6 $(E_c/k_B)\ln(G_o)$ vs. $1/T$ for samples #9 and #10, as well as samples from Delsing, *et al.* (1991) and Mooij, *et al.* (1990), in the normal state.
- Fig. 6-7 G_o vs. $1/T$ for samples #8 - #10 in the superconducting state.
- Fig. 6-8 Array energy for a single soliton as a function of the soliton position.
- Fig. 7-1 I-V curves showing the reduction of V_l with applied microwaves for sample #9 in the superconducting state, $T < 300$ mK.
- Fig. 7-2 I-V curves showing the shift in voltage ΔV with applied microwaves for

sample #9 in the superconducting state, $T < 50$ mK.

- Fig. 7-3 I-V curves showing the shift in voltage ΔV with applied microwaves for sample #9 in the normal state, $T < 50$ mK.
- Fig. 7-4 I-V curves showing the shift in voltage ΔV with applied microwaves for sample #9 in the superconducting state, $T = 300$ mK.
- Fig. 7-5 Shift in current with applied microwaves as a function of frequency.
- Fig. 7-6 Shift in voltage ΔV vs. $\sqrt{\text{microwave power}}$ for sample #9 in the superconducting state, $T < 50$ mK.
- Fig. 7-7 Shift in voltage ΔV vs. $\sqrt{\text{microwave power}}$ at two values of current, sample #9 in the superconducting state, $T < 50$ mK.
- Fig. 7-8 Shift in voltage ΔV vs. $\sqrt{\text{microwave power}}$ for sample #9 in the superconducting and normal states, $T < 50$ mK.
- Fig. A-1 (a) Schematic drawing of diamond array as fabricated.
(b) Schematic drawing of diamond array in equivalent, more intuitive fashion.
- Fig. B-1 (a) Schematic drawing of upper portion of microwave injection set-up.
(b) Schematic drawing of lower portion of microwave injection set-up.
- Fig. B-2 Line losses vs. frequency for upper portion of injection set-up.
- Fig. B-3 Line losses vs. frequency for lower portion of injection set-up.

LIST OF TABLES

Table 3-1	Parameters of e-beam resists and metal layers used to form junctions.
Table 3-2	Estimated Kapitza resistances and maximum input power levels for tin and aluminum arrays.
Table 4-1	Junction parameters for samples #1 - #5.
Table 5-1	Junction parameters for samples #6 and #7.
Table 6-1	Junction parameters for samples #7 - #10.
Table 6-2	Dependence of V_I on frustration for samples #7 - #10.
Table 6-3	Junction parameters for five arrays measured by Geerligs (1990).
Table 6-4	Measured and theoretical values of V_I for samples #8 - #10.
Table 8-1	Comparison of properties of superconducting and charging arrays.
Table C-1	List of names used to identify samples.

CHAPTER ONE

INTRODUCTION

In recent decades, improved fabrication techniques have allowed scientists to make ever-smaller electronic devices. This has opened up a new field of study entitled *mesoscopic* physics: the study of bulk-matter systems with small enough physical size so that the measurements reveal underlying quantum mechanical effects. For example, scientists have used these systems to study the wave nature of the electron by measuring what are called Quantum Conductance Fluctuations [Smith, *et al.* (1991), Washburn and Webb (1986), and references therein]. In this thesis we study systems in which the discreteness of the electronic charge influences the transport conduction properties. This class of experiments is described by the term “charging effects”.

The system in which we study charging effects is the Josephson junction, named after Brian Josephson (he won the Nobel Prize in Physics in 1973 for his theoretical prediction of the properties of this junction). A Josephson junction consists of two superconducting electrodes coupled by (1) a thin insulating barrier [a superconductor-insulator-superconductor (SIS) junction], (2) a normal metal bridge [a superconductor-normal-superconductor (SNS) junction], (3) a narrow, superconducting bridge (a microbridge), or (4) any region of weak superconductivity. One remarkable property of Josephson junctions is their ability to carry supercurrent: the flow of electrons without electrical resistance. Josephson junctions have been widely studied for the physical insights to be gained from them, as well as for their technological importance [see Tinkham (1975)].

Because of the recent advances in fabrication, we can make junctions in which the region where the two superconductors touch is on the order of 1000 \AA by 1000 \AA .

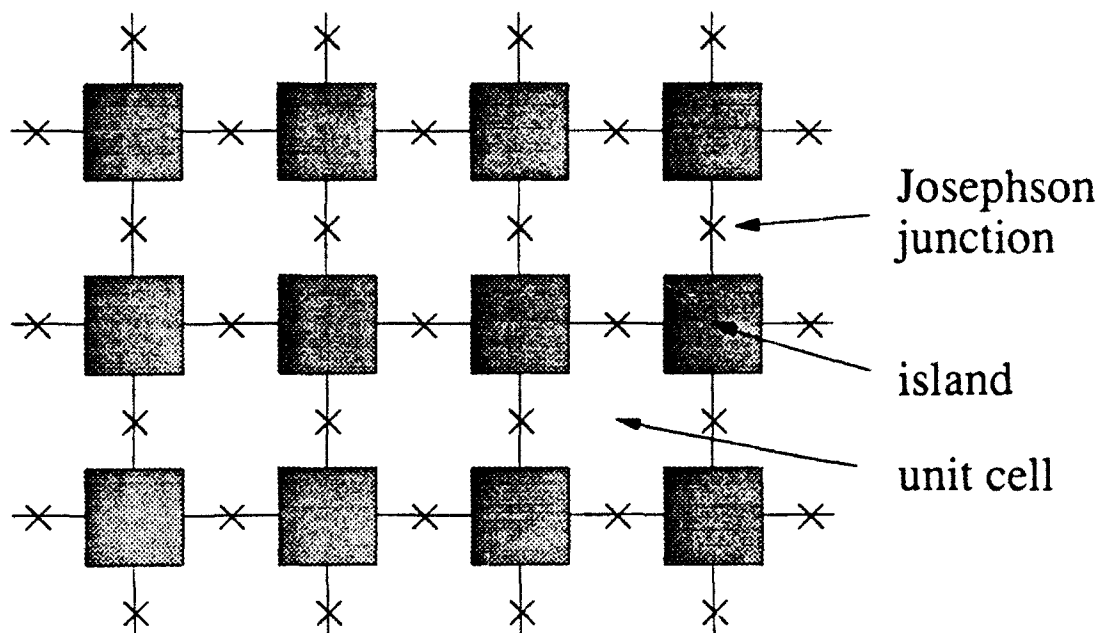


Figure 1-1.

Schematic drawing of a 2D array of Josephson junctions. The array consists of a square lattice of islands, each coupled to its nearest neighbors through a junction.

Measurements on two of these junctions in series by Fulton and Dolan (1987) showed that the discreteness of the electronic charge affected the current-voltage (I-V) characteristics: the presence or absence of a single electron on the superconducting "island" between the two junctions can greatly affect the I-V curves.¹ A considerable amount of work has gone into studying these junctions, and circuits made with them [for example, see Iansiti, *et al.* (1989a)].

In this work we study two-dimensional (2D) arrays of small Josephson junctions. Figure 1-1 shows a portion of a 2D array: a square lattice of superconducting islands, with each island coupled to its nearest neighbors through a junction (denoted as an "X").² We originally studied arrays as a means to better understand single junctions. (In single

¹Employing these junctions, scientists have made circuits, called single-electron-tunneling (SET) transistors, to use as sensitive measurement devices [LaFarge, *et al.* (1991)].

²Though not studied here, other lattices such as triangular lattices are easily fabricated.

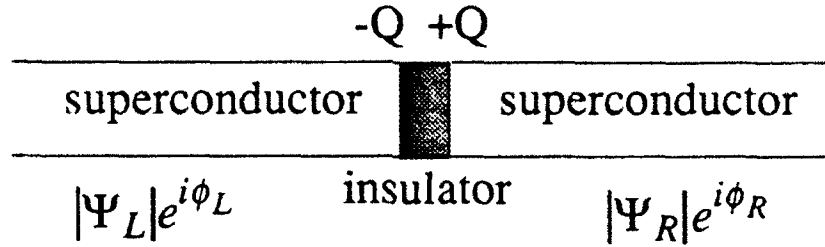


Figure 1-2.

Schematic drawing of a Josephson junction (SIS); two superconducting electrodes separated by a thin insulating barrier. Each electrode has associated with it a Ginzburg-Landau order parameter $\Psi = |\Psi|\exp(i\phi)$ and a charge Q .

junctions, close proximity to the leads largely washes out the interesting effects.¹

Junctions in the interior of an array, however, are shielded from the leads by other, high-impedance junctions.) It quickly became clear to us, however, that more interesting were traditional array phenomena (vortices, for example) in the presence of charging effects.

We begin the discussion of arrays by an introduction to the array elements: single junctions. Figure 1-2 shows a schematic drawing of an SIS junction (the type we study in this thesis): two superconducting electrodes separated by a thin, insulating barrier. The superconducting state of each electrode may be described by a Ginzburg-Landau order parameter $\Psi_{L,R} = |\Psi_{L,R}|e^{i\phi_{L,R}}$, where L and R refer to the left and right electrodes, respectively. As we use the same material for both electrodes, away from the junction $|\Psi_L| = |\Psi_R|$. What becomes important is the *phase difference* across the junction $\phi \equiv \phi_R - \phi_L$. Also shown in Fig. 1-2, as these junctions have a capacitance C associated with them, we define a junction charge Q .

To calculate the Hamiltonian, we begin with the energy associated with a Josephson junction, as derived by Ambegaokar and Baratoff (1963), $-E_J \cos \phi$. Called the Josephson energy, Ambegaokar and Baratoff give E_J as

¹See Johnson, *et al.* (1990) and Cleland, *et al.* (1992).

$$E_J = \frac{h\Delta}{8e^2 R_n} \tanh\left(\frac{\Delta}{2k_B T}\right) \quad (1.1)$$

where Δ is the superconducting gap and R_n is the normal-state resistance of the junction. The values of E_J we quote in the rest of this thesis are given in the low-temperature limit: $\tanh(\Delta/2k_B T) \approx 1 \rightarrow E_J = h\Delta/8e^2 R_n$. To $-E_J \cos\phi$ we add the energy stored in the capacitor, $Q^2/2C$. This gives the basic Hamiltonian H_0 as¹

$$H_0 = E_c \left(\frac{Q}{e}\right)^2 - E_J \cos\phi \quad (1.2)$$

where $E_c \equiv \frac{e^2}{2C}$.

The solution of this Hamiltonian is made difficult by the fact that ϕ and Q do not commute,

$$[\phi, Q] = 2ie \quad (1.3)$$

which leads to the uncertainty relation

$$\Delta\phi\Delta(Q/2e) \geq 1 \quad (1.4)$$

Therefore, in an experiment which allows us to accurately determine Q , we cannot measure ϕ (or vice versa).

This Hamiltonian has been used to solve for the junction dynamics in two limits; $E_J \gg E_c$ and $E_c \gg E_J$. Stewart (1968) and McCumber (1968) treat the first case in the

¹The full Hamiltonian, described in Chapter 2, will have additional terms representing the bias source and the dissipation mechanisms.

resistively-and-capacitively-shunted-junction (RCSJ) model. In this model, they treat ϕ as a “well-defined” variable and write Q in terms of ϕ (using $Q=CV$ and the ac Josephson equation, $V = \hbar\dot{\phi} / 2e$). We show the I-V curve given by this model in Fig. 1-3(a) (see Sec. 2.1 for the full derivation). Increasing the current from zero, it passes through the junction in the form of a supercurrent, so that no voltage develops. When the current exceeds a critical current I_c , however, the junction may no longer carry a dc supercurrent. The dc current is carried instead by quasiparticles. For the junctions we study, at I_c the voltage jumps to a value $2\Delta/e$, characteristic of quasiparticles. Sweeping the current back, for our junctions we measure a hysteretic curve: the voltage does not drop back to zero at I_c but at some lower current, called the retrapping current I_r . We call these junctions and arrays made out of them “superconducting”, as their I-V curves show a supercurrent branch.

In the other limit, $E_c \gg E_J$, we treat Q as the well-defined variable.¹ Though it is possible to write ϕ in terms of Q , we typically drop the $-E_J \cos\phi$ term in the Hamiltonian altogether. For junctions in the normal state, this is rigorously allowed as $E_J = 0$.² In fact, as it is easier to treat these junctions in the normal state than in the superconducting state, we will do so and only point out the differences between the two as they arise. In Fig. 1-3(b) we show a sample I-V curve for two of these junctions in series.³ Instead of a supercurrent branch, no current flows for voltages below a threshold voltage V_t . This region of high resistance is called the Coulomb blockade. These junctions and arrays made with them are referred to as “charging”, due to the predominance of charging effects which gives rise to this blockade region.

For junctions with E_J on the order of E_c , it is significantly more difficult to solve for the junction dynamics. Experimentally, we find these junctions to show a mixture of

¹For a review of junctions in this limit see Averin and Likharev (1991).

²We achieve normal state junctions by applying a suitably large magnetic field to eliminate the superconductivity.

³For single junctions this effect is washed out due to lead effects.

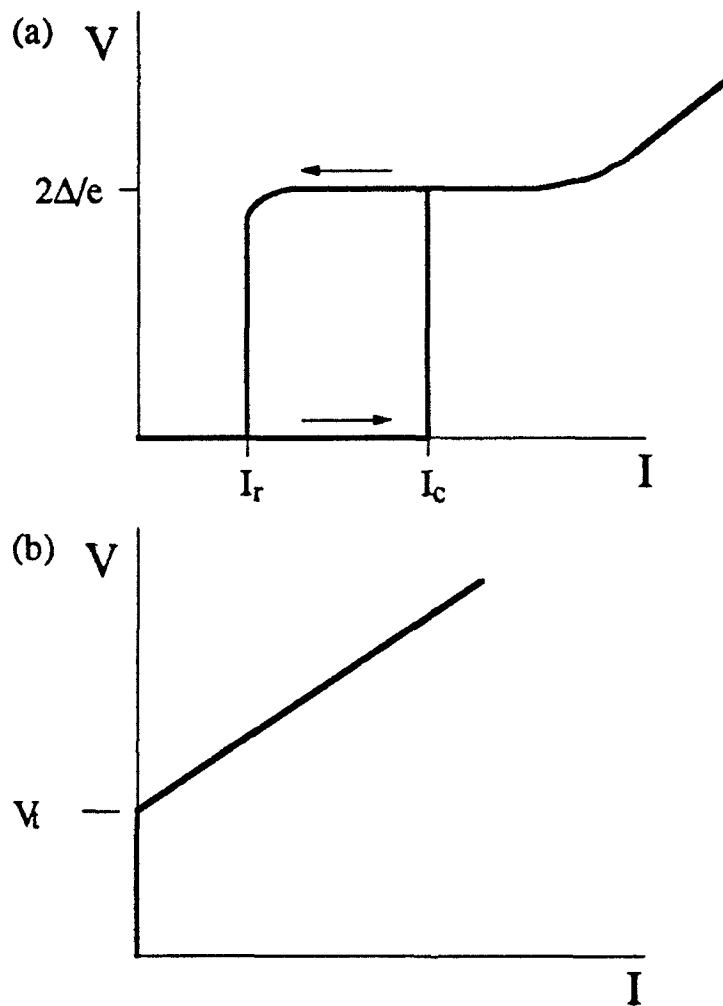


Figure 1-3.

Model I-V curves for (a) a single superconducting junction and (b) a two charging junctions in series, as described in the text. In (a), we see the supercurrent branch, the switch up to the quasiparticle branch at the critical current, and the switch back down at the retrapping current. In (b), we see the Coulomb blockade region for voltages below the threshold voltage.

superconducting and charging effects. Thus, we refer to them as “transitional”.

Figure 1-4 shows data from 2D arrays in (a) the superconducting limit and (b) the charging limit. In (a) we see the supercurrent branch and the “switch” to the quasiparticle branch. In our arrays, we do not measure one switch as with the single junction [Fig. 1-3(a)], but measure many switches. These are thought to be due to individual rows switching, as described in Chapter 4--the large spread in currents where the rows switch may be due to inhomogeneity within the array. In Fig. 1-4(a) we see that the retrapping current is roughly zero on this scale. Figure 1-4(b) shows the Coulomb blockade region of a charging array in the normal state.¹ The corner is somewhat rounded compared to that in Fig. 1-3(b). As we will discuss in Chapter 6, this rounding is expected for arrays. The differential conductance within the blockade region for this sample is greater than 10 G Ω .

These large scale properties may be viewed, in some sense, as simple extensions of single junction effects. However, more interesting are the finer scale details which can only be described by excitations in the arrays. For the superconducting arrays, the excitations are units of circulating currents called vortices. Seen in Fig. 1-5, these circulating currents are centered around a unit cell, with the strength of the currents falling off with the radial distance away from the center. A vortex may have one of two “signs”, depending on the sense of rotation. Vortices interact with a logarithmic potential; those of the same sign repel, while those of opposite signs attract and may form bound pairs. We mention four more important points about vortices. (1) Vortices are introduced into the array with an applied, external magnetic field or by a thermal activation process, in which vortex-antivortex pairs are activated out of the “vacuum”.² (2) In a model by Kosterlitz and Thouless (1973) and Berezinskii (1970) (KTB), altered to apply to Josephson junction arrays, only bound vortex-antivortex pairs exist below a

¹The steps in this figure are the result of the method used for digitizing data.

²We arbitrarily define a vortex as having counterclockwise current rotation. An antivortex has clockwise rotation.

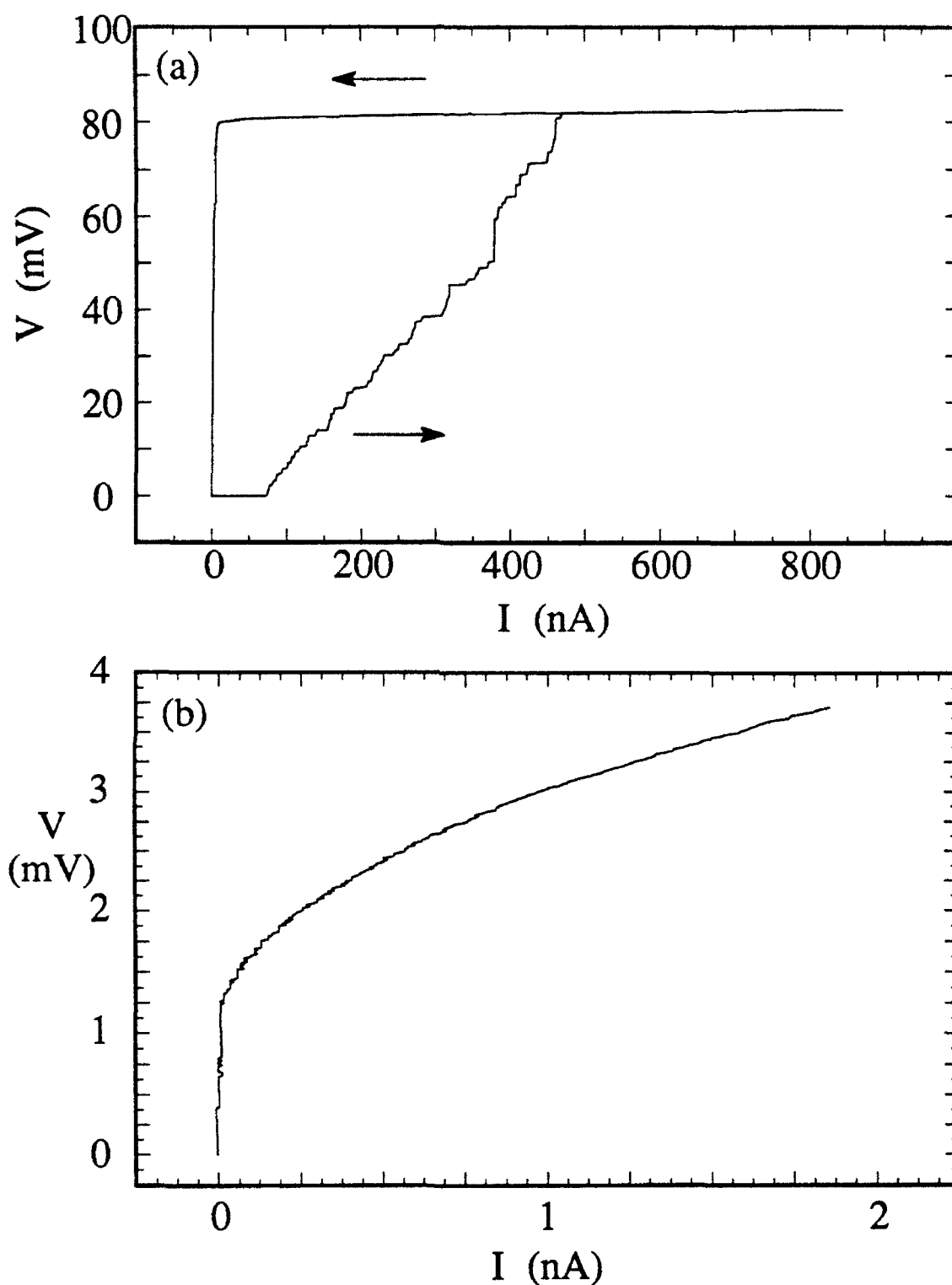


Figure 1-4.

Current-voltage (I-V) curves for (a) sample #4, a superconducting array and (b) sample #10, a charging array in the normal state. The temperature for both curves is $T = 15$ mK. The arrows in (a) show the direction of the current sweep. In (b), the curve is reversible.

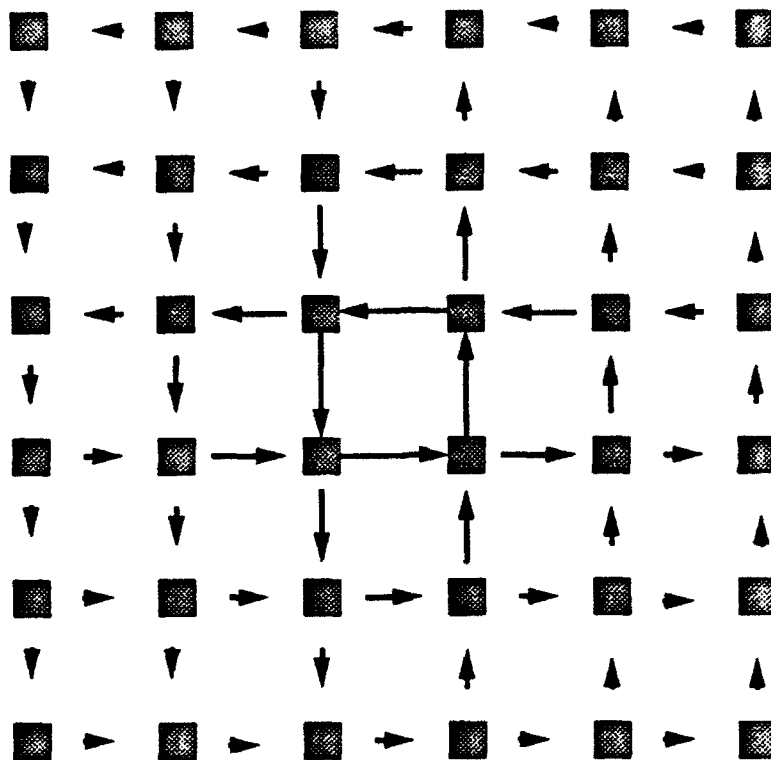


Figure 1-5.

Schematic drawing of the currents which form a vortex. Shown are the islands which form a 2D array, and arrows which represent the vortex currents (the lengths of which give the current magnitude). The junctions which connect the islands are not shown.

critical temperature T_{KTB} . For temperatures above T_{KTB} , however, enough thermal energy exists to separate the pairs, so that the system may have free vortices. (3) We measure vortex motion by applying a current bias and reading a voltage drop. The bias current applies a $\mathbf{j} \times \mathbf{B}$ force to a vortex, with the force being perpendicular to the current direction. Vortices moving across the array create a voltage drop, with the amount of drop proportional to the average vortex velocity times the vortex density. (4) At $T = 0$, the vortex density is proportional to the external magnetic field. At certain densities, the vortices form a rigid lattice commensurate with the array lattice.

In charging arrays ($E_c \gg E_J$), vortices are not present. The excitations instead are called solitons. To describe a soliton, we must first consider that each island in a

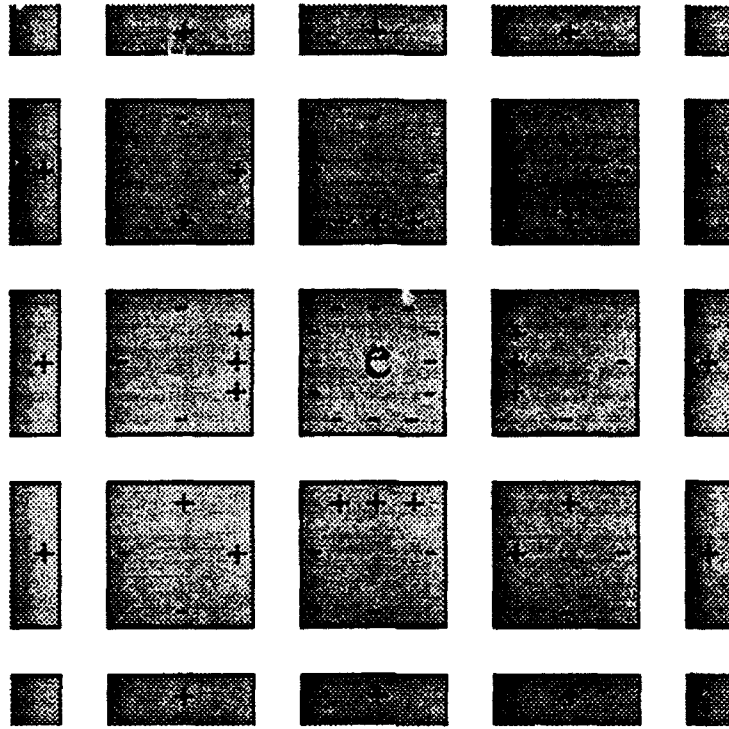


Figure 1-6.

Schematic drawing of the charge e and polarizations which form a soliton. The junctions connecting the islands are not shown.

charging array has a well-defined charge Q which changes in units of e as electrons tunnel between islands. Because of capacitive coupling, charges in the array polarize neighboring islands. A single electron added to (removed from) an island in an otherwise neutral array together with the resulting polarizations is the soliton (antisoliton), a schematic drawing of which is given in Fig. 1-6. [We follow Bakhvalov, *et al.* (1991) in using the term soliton. However, these “dressed” charges do not fit the usual definition of the term (D. S. Fisher, private communication)]. The polarizations fall off as $\sim \ln(1/r)$ with the radial distance r away from the soliton center. Solitons share many similarities with vortices: solitons interact with a logarithmic potential, and those of the same charge repel, while those of opposite charge attract and may form bound pairs. The four points made about vortices also apply to solitons. (1) Solitons are induced by a large enough

bias voltage (which pulls them from one electrode to the other), and by thermal activation, in which soliton-antisoliton pairs are activated out of the “vacuum”. Bakhvalov, *et al.* (1991) also predict that solitons may be induced with an external *electric* field, created by applying a voltage between the array and a nearby ground plane. However, this has not been confirmed experimentally. (2) Yoshikawa, *et al.* (1987) and Widom and Badjou (1988) predict the occurrence of a KTB transition for the unbinding of soliton-antisoliton pairs. However, as we will discuss in Chapter 6, for the arrays we and other groups have measured the KTB model does not appear to apply.¹ (3) We determine soliton motion by applying a force to the solitons, by a bias voltage, and measure the electrical (soliton) current. (4) Bakhvalov, *et al.* (1991) predict that solitons may form lattices commensurate with the array lattice. However, this has not yet been experimentally observed.

The data presented in Figs. 1-4(a) and (b) are taken at sample temperatures of $T \approx 15$ mK, close to the $T \rightarrow 0$ limit. At higher temperatures, we measure finite resistances in the supercurrent branch [Fig. 1-7(a)] and finite conductances in the Coulomb blockade region [Fig. 1-7(b)]. As the I-V curves around zero bias appear to be linear, we can define a zero-bias resistance R_0 . We study R_0 as a function of temperature to better understand the properties of solitons and vortices. Figure 1-7(c) shows R_0 vs. T/T_c for the ten samples presented in this thesis. The lower five curves, in which R_0 monotonically decreases with decreasing T , are for samples with $E_J > E_C$ (superconducting arrays). The upper three curves, in which R_0 monotonically *increases* with decreasing T , are for samples with $E_C > E_J$ (charging arrays). The samples which give the middle two curves (the ones which cross close to zero temperature) fall into the category of transitional arrays.

Figure 1-7(c) is a graphical representation of the superconductor-to-insulator (S-I)

¹Mooij, *et al.* (1990) and Delsing, *et al.* (1992).

transition.¹ As $T \rightarrow 0$, arrays with large E_J/E_c become superconducting around zero bias while those with small E_J/E_c become insulating. It is not our intent to study the S-I transition itself. The goal of this thesis is to study, in detail, the conduction mechanisms of arrays on both sides of the S-I transition.

The outline of this thesis is as follows. In the second chapter we give a theoretical overview of these junctions and arrays. The third chapter describes the details of the experiment: array design, fabrication, and measurement. In Chapters 4, 5, and 6 we discuss the experimental results of the superconducting, transitional, and charging arrays, respectively. Chapter 7 gives details of a side experiment in which we irradiate a charging array with microwaves. We conclude in Chapter 8. Appendices A, B, and C discuss the design of the “diamond” arrays, detailed information on the microwave line losses, and the different sample names used, respectively.

¹See Haviland, *et al.* (1989), Fisher (1990), Fisher, *et al.* (1990), and Granato and Kosterlitz (1990).

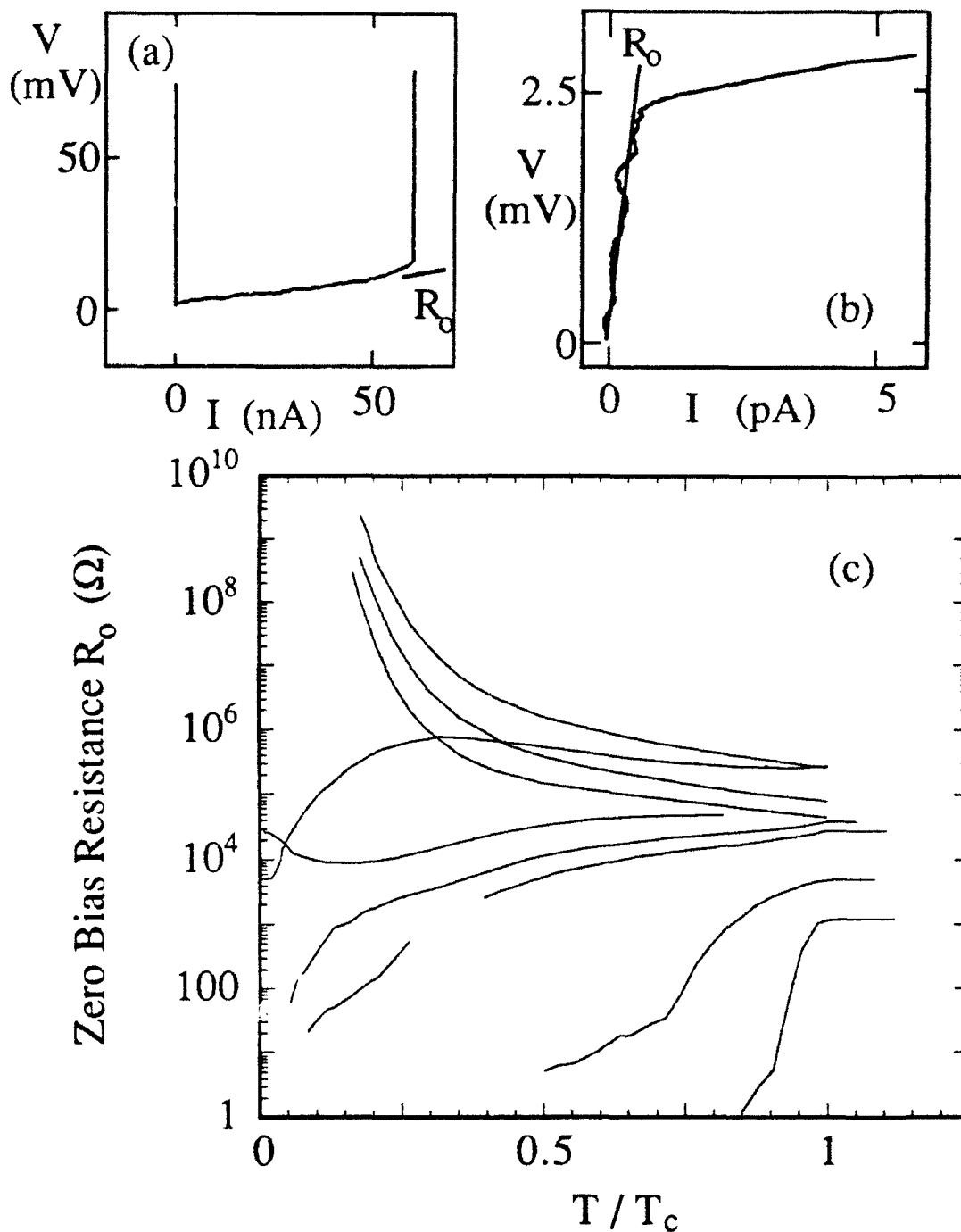


Figure 1-7.

Figures (a) and (b) are I-V curves for samples #4 and #10, respectively, showing the definition of the zero-bias resistance R_0 for both the superconducting and charging arrays. The sample temperature in both curves is $T = 300$ mK. Figure (c) shows R_0 as a function of T/T_c for the ten arrays presented in this thesis.

CHAPTER TWO

THEORETICAL OVERVIEW

In this chapter we give a theoretical overview of the array experiments. The discussion is organized as follows: Secs. 2.1 and 2.2 describe the theory for “superconducting” single junctions and arrays, respectively. Sections 2.3 and 2.4 present the theory for the “charging” junctions and arrays. All of the discussion in this chapter is in the $T = 0$ limit. We save discussion of the $T \neq 0$ results for Chapters 4, 5, and 6.

2.1 Superconducting Junctions

We begin this description of superconducting junctions by presenting the full junction Hamiltonian $H(\phi, Q)$ (Sec. 2.1.1) and using it to derive a single junction equation of motion (Sec. 2.1.2). This equation of motion forms the basis of the resistively-and-capacitively-shunted-junction (RCSJ) model, which we describe in Sec. 2.1.3. Section 2.1.4 presents the intuitive washboard model, and shows how it is used to derive junction I-V curves.

2.1.1 Single Junction Hamiltonian

In Chapter 1 we presented the basic Hamiltonian H_0 for a junction

$$H_0 = E_c \left(\frac{Q}{e} \right)^2 - E_J \cos \phi \quad (2.1)$$

The full Hamiltonian $H(\phi, Q)$ will include a term representing the bias source H_s , and a term representing dissipation H_e ,

$$H(\phi, Q) = H_o + H_s + H_e \quad (2.2)$$

To get the source term H_s , we calculate the negative of the energy fed into the junction by a current bias,

$$H_s = -\int I(t)V(t)dt \quad (2.3)$$

Using the ac Josephson equation

$$V(t) = \frac{\hbar}{2e} \frac{d\phi}{dt} \quad (2.4)$$

and integrating by parts, we get

$$H_s = -\frac{\hbar I}{2e} \phi + \frac{\hbar}{2e} \int \phi \frac{dI}{dt} dt \quad (2.5)$$

If I is constant in time, the second term gives zero and

$$H_s = -\frac{\hbar I}{2e} \phi \quad (2.6)$$

The dissipation term H_e is more difficult to quantify. We will leave this term undefined as we are more interested in damping in arrays due to vortex dissipation, than in single junction damping. [Bobbert (1992) shows numerically that for the junctions we measure, vortex dissipation is largely *independent* of single junction damping.] For more

information about single junction dissipation, we refer the reader to Iansiti (1988) (dissipation due to quasiparticle tunneling), Johnson (1990) (dissipation due to electromagnetic radiation), and Caldeira and Leggett (1981, 1983) (general formalism for addressing dissipation).

2.1.2 Single Junction Equation of Motion

As $(\hbar/2e)Q$ and ϕ are canonical variables, we can use Hamilton's equations [$\dot{\phi} = (2e/\hbar)\partial H/\partial Q$ and $\dot{Q} = -(2e/\hbar)\partial H/\partial\phi$] to write

$$\dot{\phi} = \frac{2e}{\hbar} \frac{Q}{C} \quad (2.7)$$

$$\dot{Q} = -I_c \sin\phi + I - I_e \quad (2.8)$$

where $I_c = (2e/\hbar)E_J$ and $I_e \equiv (2e/\hbar)\partial H_e/\partial\phi$ (Caldeira and Leggett show that H_e is not a function of Q). As $Q/C = V$, the first expression is just a statement of the ac Josephson relation, Eqn. (2.4). Equation (2.8) is a statement of current conservation: the bias current I gets divided up into the Josephson channel $I_c \sin\phi$, the capacitive channel \dot{Q} , and the dissipative channel I_e .

We can write Eqn. (2.8) as an equation of motion. First, we use Eqn. (2.7) to write Q in terms of ϕ . Next, if we treat the dissipation as simply resistive, then we can write I_e as $I_e \equiv V/R_e = \hbar\dot{\phi}/2eR_e$.¹ Finally, multiplying through by $2e/\hbar C$ gives

$$\frac{d^2\phi}{dt^2} + \frac{1}{R_e C} \frac{d\phi}{dt} + \frac{8}{\hbar^2} E_c E_J \sin\phi - \frac{4E_J}{\hbar e} I = 0 \quad (2.9)$$

¹ As previously mentioned, in general the dissipation channel will be far more complex than simply resistive. For the level of our discussion, however, this approximation is reasonable.

This is the equation of motion for a driven, damped pendulum; $\ddot{\phi}$ represents an inertia term, $\dot{\phi} / R_e C$ represents a damping term, $(8/\hbar^2)E_c E_J \cos\phi$ represents a restoring force term, and $-(4E_J/\hbar e)V$ represents a driving term.

2.1.3 The RCSJ Model

In the RCSJ model, we treat the junction as being shunted by a resistance and a capacitance. Figure 2-1 shows a schematic drawing of the three channels plus a current bias source. The Josephson branch, denoted with an "X", carries a supercurrent I_s given by the dc Josephson equation

$$I_s = I_c \sin \phi \quad (2.10)$$

If $V (\propto \dot{\phi}) = 0$, then I_s has a dc component. Also, I_s has a dc component in the case of Shapiro steps, where the voltage is non-zero but oscillatory [Benz (1990)]. However, for the case where V is a non-zero constant, the supercurrent has an ac component only.

As the supercurrent may be written $I_s = I_c \sin[(2e/\hbar) \int V dt]$, the Josephson channel has an inductance associated with it. We calculate this inductance by taking the derivative of the current with respect to time, $L \equiv V / (dI / dt)$. This gives the Josephson inductance L_J as

$$L_J = \frac{\hbar}{2eI_c \cos \phi} \quad (2.11)$$

Therefore, the three channels which form the junction behave similarly to an RCL circuit. Analogous to the oscillations in an RCL circuit, for a time-averaged current $\bar{I} < I_c$ the junction may show small oscillations in ϕ , called plasma oscillations, about an average value $\bar{\phi} = \arcsin(\bar{I} / I_c)$. In the limit of $I = 0$ and for low damping, these small

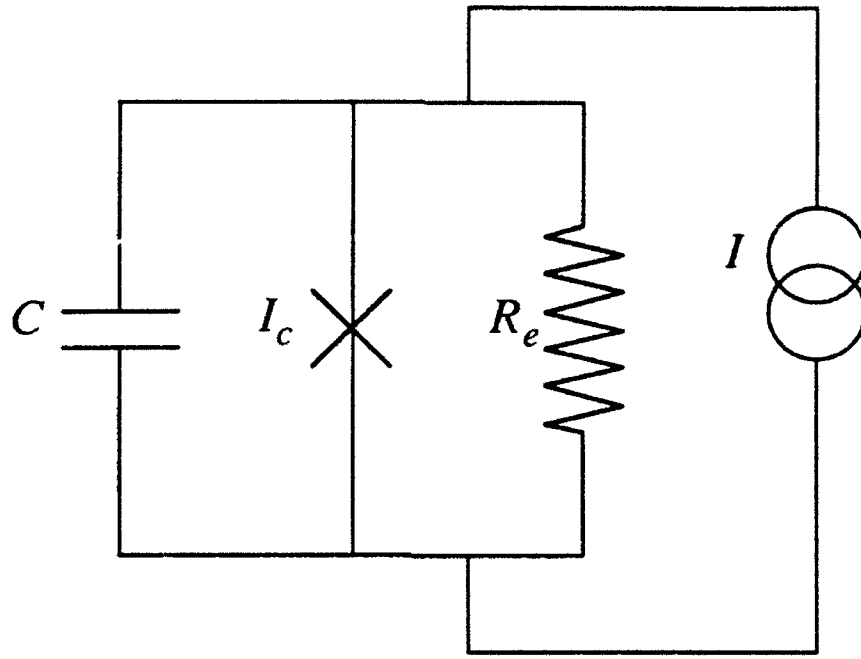


Figure 2-1.

Schematic drawing of a superconducting junction in the RCSJ model. The Josephson channel, denoted with an "X", is shunted by a resistance R_e and a capacitance C . Shown also is the current source.

oscillations in ϕ occur at the plasma frequency ω_p

$$\omega_p = \frac{1}{\hbar} \sqrt{8E_c E_J} \quad (2.12)$$

As the three channels are in parallel, the damping of these oscillations is inversely proportional to R_e . To quantify the damping, we introduce the McCumber damping parameter β_c [McCumber (1968)]

$$\beta_c = \frac{2e}{\hbar} I_c R_e^2 C \quad (2.13)$$

(large β_c means low damping and vice versa). β_c is the square of the quality factor Θ of

the circuit. For $\beta_c > 1$, the plasma oscillations are underdamped, while for $\beta_c < 1$, overdamping occurs. SIS junctions, the ones discussed in this thesis, typically have underdamped oscillations, while the oscillations for SNS junctions are usually overdamped.

2.1.4 The Washboard Model

Returning to the Hamiltonian, we write (neglecting H_e)

$$H(\phi, Q) = \frac{Q^2}{2C} - E_J \cos \phi - \frac{\hbar I}{2e} \phi \quad (2.14)$$

As described by Iansiti (1988), we can make the comparison of ϕ and Q to the mechanical variables position and momentum: ϕ plays the role of position x ; $(\hbar/2e)Q$ plays the role of momentum p ; and $(\hbar/2e)^2 C$ acts as a mass M . $H(\phi, Q)$ then resembles

$$H(x, p) = \frac{p^2}{2M} + U(x) \quad (2.15)$$

where $U(x)$ is a potential energy. In our coordinate system

$$U(\phi) = -E_J \cos \phi - \frac{\hbar I}{2e} \phi \quad (2.16)$$

Figure 2-2 shows this potential, called the washboard potential, for different values of bias current I : the larger I , the stronger the "tilt" of the washboard. We treat this system as a particle of mass $(\hbar/2e)^2 C$ sitting in this potential. The particle motion is measured by the voltage, as $\dot{\phi} \propto V$.

This figure shows four different cases which lead to different segments of the I-V curves. In (a), a small bias current is applied so that the washboard tilts, though not

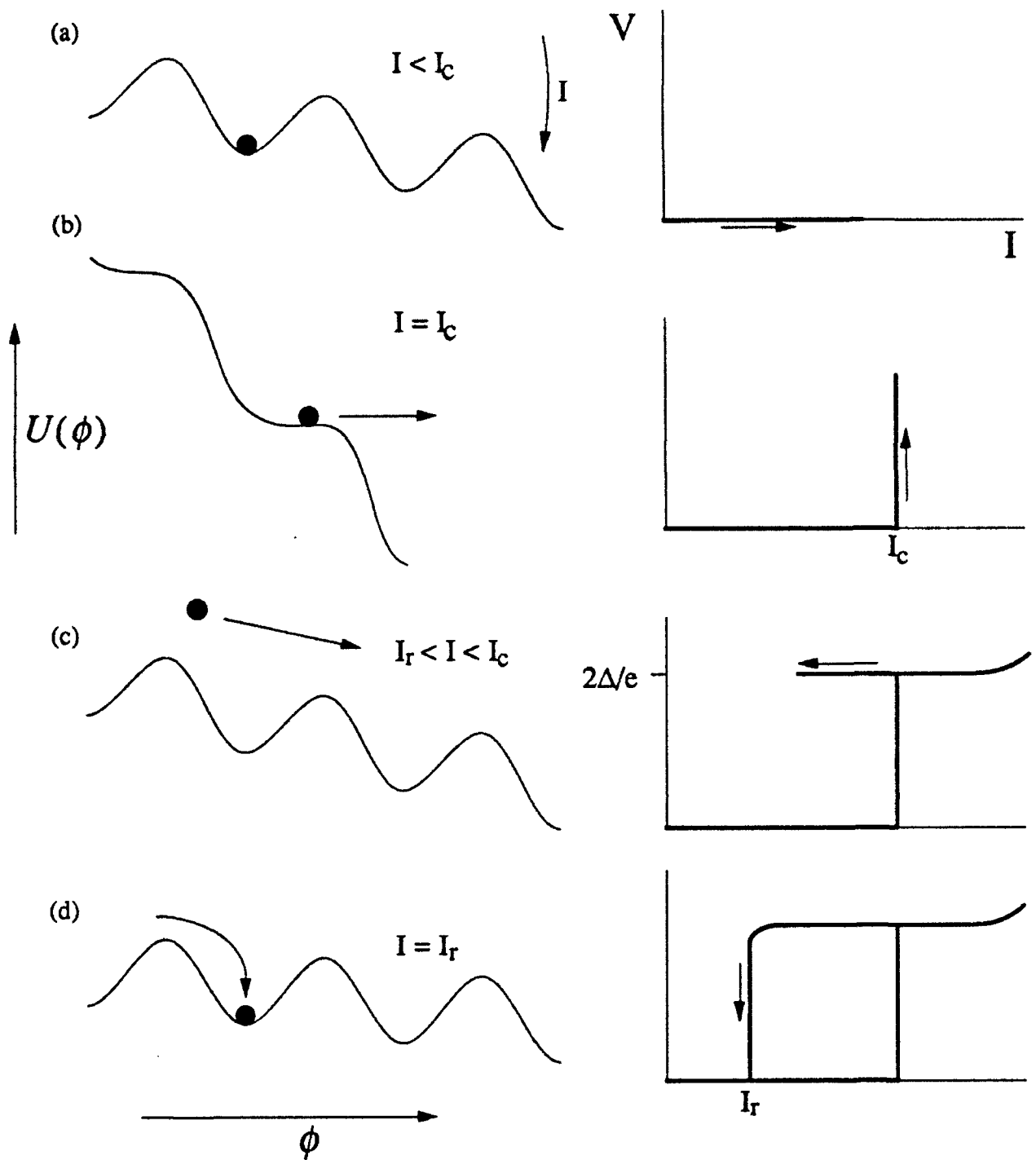


Figure 2-2.

This figure shows the washboard potential, and the corresponding segments of the junction I-V curve, for four different cases, as described in the text.

enough to let the particle escape. $\dot{\phi}$ will not have a dc component, so no dc voltage develops across the junction. As seen in the I-V curve, this is the supercurrent branch (the small oscillations of the particle in the bottom of the well are the plasma oscillations already discussed). In (b), as I is increased to I_c , the wells disappear and the particle escapes, moving down the washboard. $\dot{\phi}$ will have a dc component so that we measure a dc voltage. As our junctions are underdamped, the voltage jumps up to the quasiparticle branch. In (c), the current has been decreased to where the wells reappear. For underdamped junctions, the particle "inertia" and the low damping may enable it to continue down the washboard. The I-V curves will then be hysteretic, as the voltage remains high for currents below I_c . At the retrapping current I_r , however, the damping which does exist causes the particle to retrap into a well, and we measure the voltage dropping back to zero (d). Stewart (1968) and McCumber (1968) give the value of the theoretical retrapping current as

$$I_r = \frac{4}{\pi} \frac{I_c}{\sqrt{\beta_c}} \quad (2.17)$$

2.2 Superconducting Arrays

Having covered the relevant theory for single superconducting junctions, we can now study arrays of these junctions. Breaking this discussion into four sections, we begin with the array Hamiltonian in Sec. 2.2.1. In Sec. 2.2.2, we look at the 2D analog of the washboard potential, the eggcrate potential. Sections 2.2.3 and 2.2.4 present the vortex equation of motion and collective effects, respectively.

2.2.1 Array Hamiltonian

In a zero applied magnetic field, the basic Hamiltonian H_o for an array of junctions is just the sum of the Hamiltonians of the individual junctions,

$$H_o = \sum_{\langle i,j \rangle} \left[E_c \left(\frac{Q_{ij}}{e} \right)^2 - E_J \cos(\phi_i - \phi_j) \right], \quad B = 0 \quad (2.18)$$

where the sum $\langle i, j \rangle$ is over nearest neighbor islands, ϕ_i is the phase of the i^{th} island and Q_{ij} is the charge across the junction connecting the i^{th} and j^{th} islands.¹ With an applied magnetic field present, we must add an additional term Ψ_{ij} to the phases

$$H_o = \sum_{\langle i,j \rangle} \left[E_c \left(\frac{Q_{ij}}{e} \right)^2 - E_J \cos(\phi_i - \phi_j - \Psi_{ij}) \right], \quad B \neq 0 \quad (2.19)$$

$$\Psi_{ij} = \frac{2e}{\hbar} \int_i^j \vec{A} \cdot d\vec{l} \quad (2.20)$$

As Eqn. (2.20) shows, Ψ_{ij} is a line integral of the vector potential \vec{A} along a path from island i to island j .

The zero-temperature ground state of this Hamiltonian has been extensively studied [see Rzchowski, *et al.* (1990), and references therein]. For $B \neq 0$ the ground state consists of units of circulating currents called vortices. Figure 2-3 shows the phases ϕ_i which make up a vortex (the angle of an arrow from vertical gives its phase). In Fig. 1-5, we showed the currents which correspond to these phases.

¹We use B to denote the applied magnetic field, as H is used to denote the Hamiltonian.

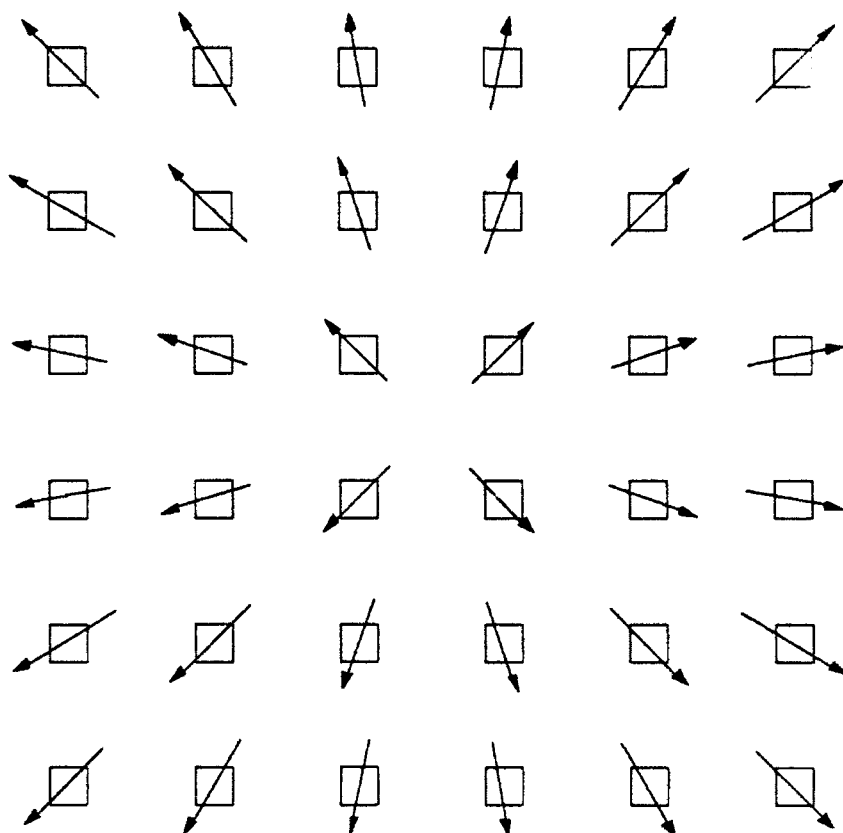


Figure 2-3.

This figure shows the configuration of phases ϕ_i which correspond to a vortex (Fig. 1-5 shows the corresponding currents). The phases are represented by the angle of the arrows from vertical (we define vertical as an arrow pointing towards the top of the page).

Though a vortex is an extended object, it is often useful to determine a position which corresponds approximately to its center. For a single vortex, we can use the “arctan” approximation: the phases of the islands ϕ_i are approximately given by

$$\phi_i = \arctan[(y_i - y_o) / (x_i - x_o)] \quad (2.21)$$

where (x_o, y_o) represents the position of the vortex center and (x_i, y_i) represents the island coordinates.

2.2.2 Eggcrate Potential

Rzchowski, *et al.* (1990), following the work of Lobb, *et al.* (1983) solved the potential energy stored in an array for a single vortex as a function of the vortex position. Figure 2-4 shows this potential energy for a portion of the array. Called an eggcrate potential, it consists of a lattice of wells commensurate with the array lattice. The well bottoms are located at the center of the array unit cells (the phase configuration in Fig. 2-3 represents this low energy position), while the high energy peaks correspond to the island centers. To cross from one well to another, a vortex must go over a saddle-like barrier, where the saddle point sits on top of a junction.

The wells are important in describing vortex motion as they act as a regular array of pinning sites. We define the pinning barrier E_b as the energy difference between the saddle point and the bottom of the well. Lobb, *et al.* (1983) numerically calculated this barrier E_b to be

$$E_b \approx 0.199E_J \quad \text{square lattice} \quad (2.22a)$$

$$E_b \approx 0.043E_J \quad \text{triangular lattice} \quad (2.22b)$$

The eggcrate potential is the 2D analog of the washboard potential pictured in Fig. 2-2. The vortex, similar to the “particle” in the washboard, sits pinned in a well unless forced out by the $\mathbf{j} \times \mathbf{B}$ force of a strong enough bias current.¹ Equivalently, we may think of the entire eggcrate tilting, with the amount of tilt proportional to the current. We refer to the current level at which the vortex can first overcome the barrier as the depinning current I_d . From Eqn. (2.22a), Lobb, *et al.* (1983) give I_d to be

¹ A vortex may also be thermally activated out of a well for non-zero temperatures, or may be forced out by the nearby presence of other vortices.

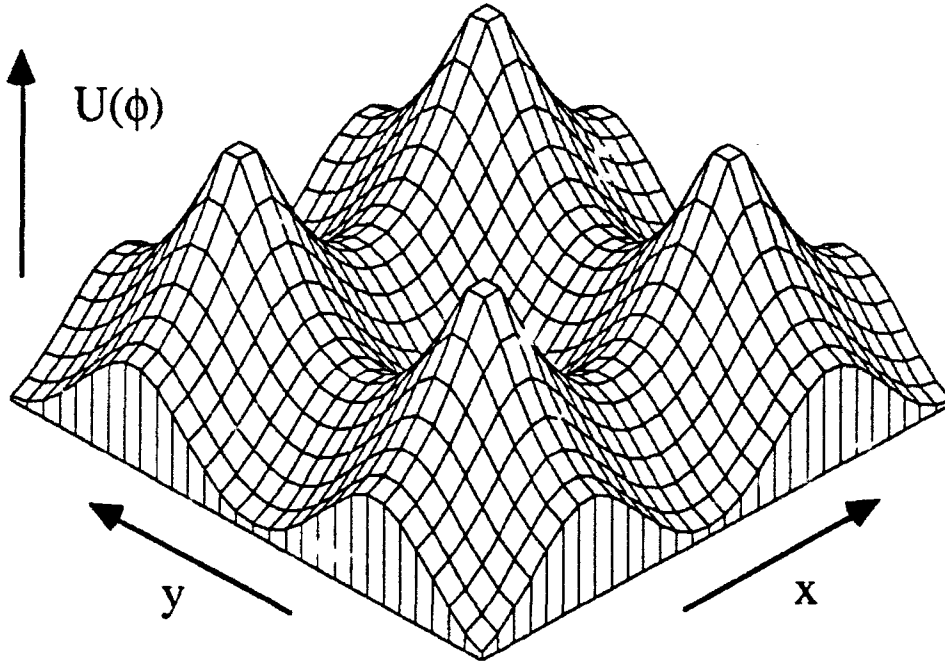


Figure 2-4.

This figure shows the potential energy $U(\phi)$ of a single vortex as a function of its position within an array [Rzchowski, *et al.* (1990)]. This potential is commonly called the eggcrate potential.

$$I_d \approx 0.199 I_c / 2 \quad (2.23)$$

Unlike the washboard potential, with its one “particle”, the eggcrate potential may be populated with *many* vortices. Vortices interact with one another logarithmically

$$U = \mu_{core} + 2\pi E_J \ln r \quad (2.24)$$

where r is the vortex-vortex separation (in units of the lattice spacing), and μ_{core} represents the energy of two vortices with separation $r = 1$ (core energy). Vortices of like rotation repel while those of opposite rotation attract. The interplay between pinning and

the vortex-vortex interaction can lead to interesting effects, such as vortex lattices commensurate with the array lattice, as discussed in Sec. 2.2.4, and “giant” Shapiro steps, as described by Benz, *et al.* (1990) and Sohn, *et al.* (1991).

2.2.3 Vortex Equation of Motion

Rzchowski, *et al.* (1990) consider a single vortex in an array with a bias current in the \hat{y} direction, so that the vortex feels a $\mathbf{j} \times \mathbf{B}$ force in the \hat{x} direction. Restricting the vortex to move only along \hat{x} , they approximate the vortex equation of motion as

$$\frac{d^2}{dt^2} \left(\frac{2\pi x}{a} \right) + \frac{1}{R_e C} \frac{d}{dt} \left(\frac{2\pi x}{a} \right) + \frac{8\kappa}{\hbar^2} E_c E_J \sin \left(\frac{2\pi x}{a} \right) - \frac{8E_J}{\hbar e} I = 0 \quad (2.25)$$

where a is the lattice spacing, and κ is given by $E_b = \kappa E_J$ [$\kappa \approx 0.199$ from Eqn. (2.22a)].

For comparison, we rewrite the single junction equation of motion [Eqn. (2.9)]

$$\frac{d^2 \phi}{dt^2} + \frac{1}{R_e C} \frac{d\phi}{dt} + \frac{8}{\hbar^2} E_c E_J \sin \phi - \frac{4E_J}{\hbar e} I = 0 \quad (2.26)$$

Equating $(2\pi x/a)$ with ϕ , the two equations are identical to within factors of order 1. Thus, the motion of a single vortex in an array, and its I-V characteristics, might be expected to match closely those for a single junction (Fig. 2-2). For example, we expect vortices to exhibit plasma oscillations, in the bottoms of their wells, at a frequency¹

$$\omega_o \approx \frac{1}{\hbar} \sqrt{8\kappa E_c E_J} \quad (2.27)$$

However, as we will discuss in Chapter 4, vortices are subject to a damping

¹Derived from Eqn. (2.25) in the limit of $I = 0$ and low damping.

mechanism not present in single junctions: a moving vortex transfers energy to the junctions over which it travels in the form of a "wake". Thus, a vortex will be more heavily damped than the similarities of Eqns. (2.25) and (2.26) might suggest.

2.2.4 Commensuration Effects

To this point we have mostly considered single vortices. However, with an applied magnetic field we can increase the density of the vortices so that the vortex-vortex interactions become important. We describe the vortex density in terms of the number of vortices per unit cell f (also called the frustration)

$$f = \frac{Ba^2}{\Phi_o} \quad (2.28)$$

where Φ_o is the flux quantum

$$\Phi_o \equiv \frac{h}{2e} = 2.07 \times 10^{-15} \text{ Tesla} \cdot \text{m}^2 \quad (2.29)$$

For frustrations $f = p/q$, where p and q are integers, vortices form lattices commensurate with the array lattice. Figure 2-5 shows commensurate lattices for (a) $f = 1/2$ and (b) $f = 1/3$. With $f = 1/2$, called the "fully frustrated" case, the vortices form a checkerboard-like pattern.

At $f = 1$, a vortex fills every unit cell in the array. Except at the array edges, the circulating currents from neighboring unit cells identically cancel, so that the array interior for $f = 1$ resembles that for $f = 0$. Therefore, features in the I-V curves dependent on f will show periodicity in f with period $\Delta f = 1$.

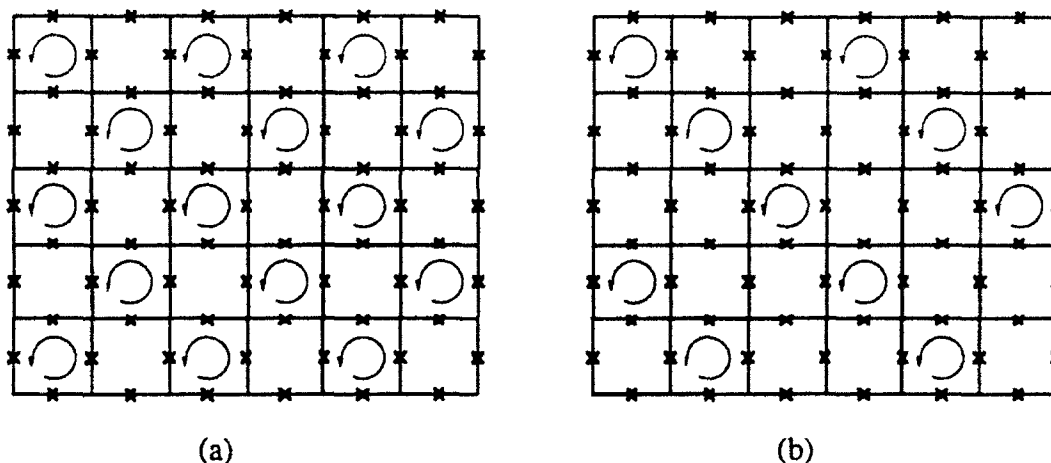


Figure 2-5.

This figure shows commensurate vortex lattices for (a) $f = 1/2$ and (b) $f = 1/3$. Vortices are represented by the circular arrows.

These commensurate lattices tend to lock vortices into specific positions with respect to the other vortices of the lattice. Thus, the lattice generally moves together as a unit. Many features common to lattices, such as shear and defects, also apply to vortex lattices.

2.3 Charging Junctions

We now study the charging limit, where E_c is the dominant energy. As mentioned briefly at the beginning of this chapter, when describing charging effects it is easier to discuss normal-insulator-normal (NIN) junctions than SIS junctions. Therefore, in this section and Sec. 2.4, we only address NIN junctions. As we will see in Chapter 6, this approach is reasonable as SIS charging arrays show similar behavior to NIN charging arrays. In that chapter we will discuss the differences as they arise.

Although it is easier in some ways to begin with a single charging junction, its I-V characteristics are strongly dependent on such complex issues as the junction's electromagnetic environment and the nature and stiffness of the bias source. We will

instead start with a double junction system (two junctions in series), as its I-V characteristics are not as sensitive to these factors. Also, a double junction may be thought of as a *single island* coupled through junctions to two leads. By studying this system, we are already looking ahead towards arrays, where the dynamics are described by the charging of islands.

We break this section into two parts. Section 2.3.1 discusses the double junction Hamiltonian and Sec. 2.3.2 derives its I-V characteristics.

2.3.1 Double Junction Hamiltonian

In the normal state, $E_J = 0$ so that the single junction Hamiltonian H_0 (which here equals the capacitive energy E_{single}) becomes

$$H_0 = E_{single} = \frac{Q^2}{2C} \quad (2.30)$$

The energy stored in a double junction, a schematic drawing of which is given in Fig. 2-6, requires only a few modifications. First, we redefine Q as the charge difference, from neutral, on the island. Specifically, $Q = en + Q_0$, where $n \equiv$ total number of electrons on island minus the total number of protons. Q_0 represents the charge "fed" into the island by a gate capacitor, $Q_0 = C_g V_g$ (see Fig. 2-6), plus any other charges induced by stray electric fields. We also replace C in Eqn. (2.30) by the sum of the capacitances $C_\Sigma \equiv 2C + C_g$.¹ The capacitive energy for a double junction E_{double} then is

$$E_{double} = \frac{(en + Q_0)^2}{2C_\Sigma} \quad V = 0 \quad (2.31)$$

¹We have taken the capacitances of the two junctions to be equal. If the junctions, labeled 1 and 2, have different capacitances, then $C_\Sigma \equiv C_1 + C_2 + C_g$

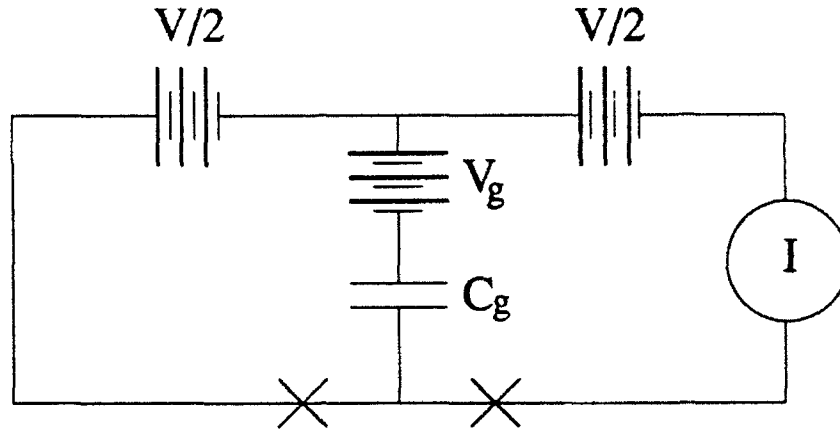


Figure 2-6.

A schematic drawing of a double junction system. A voltage V_g is applied through the gate capacitor to the island formed by the two junctions.

As noted, Eqn. (2.31) is valid for the zero-bias voltage case only. For non-zero biases the capacitive energy term is given by

$$E_{double} = \frac{(en + Q_0)^2}{2C_\Sigma} + \frac{C_1 C_2 V^2}{2C_\Sigma} \quad (2.32)$$

We will use these energies to determine the system I-V characteristics.

2.3.2 Double Junction I-V Curves

According to the "orthodox" theory of these junctions [Averin and Likharev (1991) and Hanna (1992)], the I-V curves may be calculated analytically using a Hamiltonian given by H_0 and terms which include probabilistic tunneling elements. However, we can motivate the more basic I-V features using the artifice of energy level diagrams. Figure 2-7 shows the energy levels of the two electrodes and the island for $Q_0 = 0$ and a small

bias voltage V . All states below the Fermi energy are filled and all states above it are empty. As $Q_o = 0$, the Fermi level of the island sits at $eV/2$.¹ An electron attempting to tunnel onto the island ($n = 0 \rightarrow n = 1$) will raise the Fermi level by the capacitive charging energy given in Eqn. (2.32), $e^2/2C_\Sigma$. As Fig. 2-7 shows, for bias voltages below some threshold V_t this transition is energetically forbidden. Therefore, no current may pass through the system. This corresponds to the Coulomb blockade region. However, for large enough bias voltages, as seen in Fig. 2-8, the transition $n = 0 \rightarrow n = 1$ becomes allowed and electrons may tunnel through the two junctions, giving rise to a current. Figure 2-9 shows an I-V curve for the $Q_o = 0$ case including this Coulomb blockade region.

For completeness, we need to define two voltage levels, the threshold voltage V_t and the offset voltage V_{off} . V_t is the voltage level where current first begins to flow. For $Q_o = 0$, as current will flow for $eV/2 > e^2/2C_\Sigma$, $V_t = e/C_\Sigma$. V_{off} is the voltage where the asymptote, to which the I-V curve approaches at large voltages, extrapolates back to $I = 0$, i.e., voltage axis. As Fig. 2-9 shows, for $C_1 = C_2$ and $Q_o = 0$ the threshold and offset voltages match, and have the value

$$V_{off} = \frac{e}{C_\Sigma} \quad (2.33)$$

In general, following the work of Averin and Likharev (1991), Eqn. (2.33) is true for all values of Q_o . However, as the next case will show, V_t depends strongly on Q_o .

If $Q_o \neq 0$, we get different I-V characteristics. For example, we will look at the case where $Q_o = -e/2$. For $V = 0$ and $n = 0$, Eqn. (2.31) gives the system energy as $E_{double} = e^2/8C_\Sigma$. If we tunnel an electron onto the island, i.e., $n = 0 \rightarrow n = 1$, Eqn. (2.31) again gives the system energy as $E_{double} = e^2/8C_\Sigma$. Therefore, as it costs no energy for

¹ This is true only for the symmetric junction case; $C_1 = C_2 = C$.

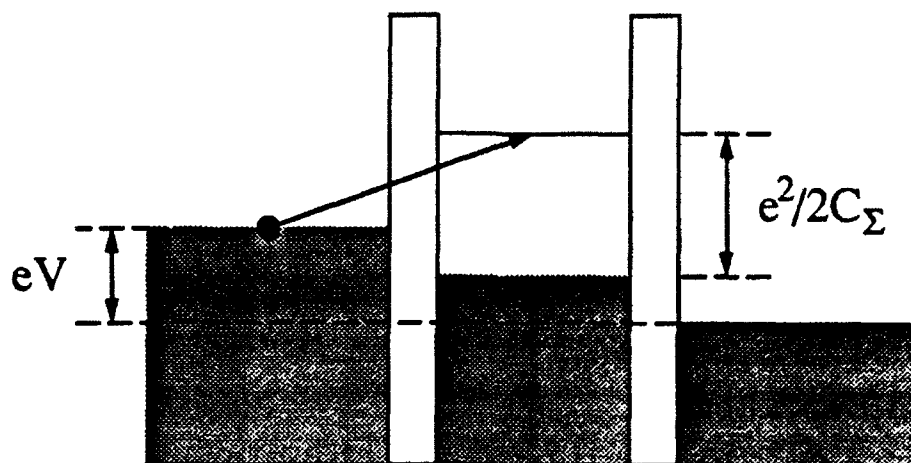


Figure 2-7.

Energy level diagram of the two junction system for $Q_0 = 0$ and $V < V_t$. The transition of an electron from the left electrode to the island is energetically forbidden, so that no current may flow. This corresponds to the Coulomb blockade region.

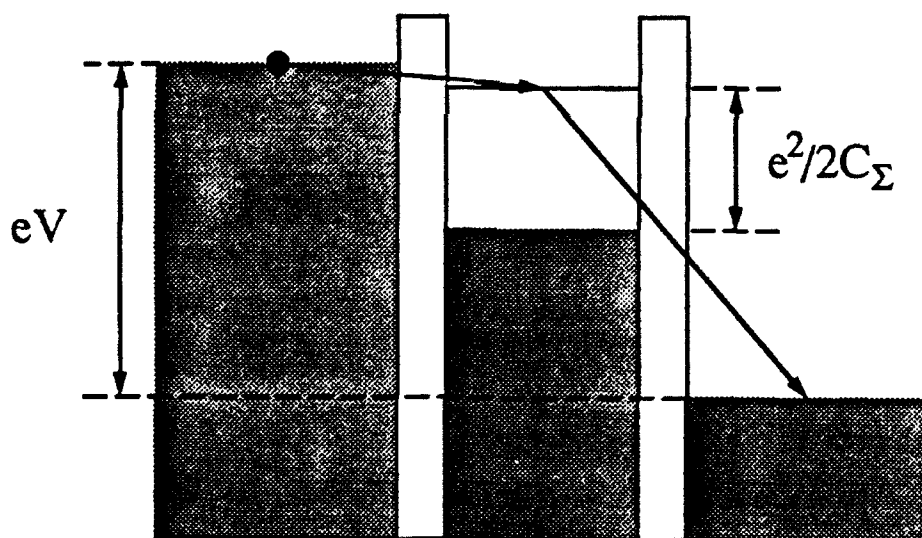


Figure 2-8.

Energy level diagram for a two junction system with $Q_0 = 0$ and $V > V_t$. For this case, it is energetically allowed for an electron to tunnel onto the center island, so that current flows.

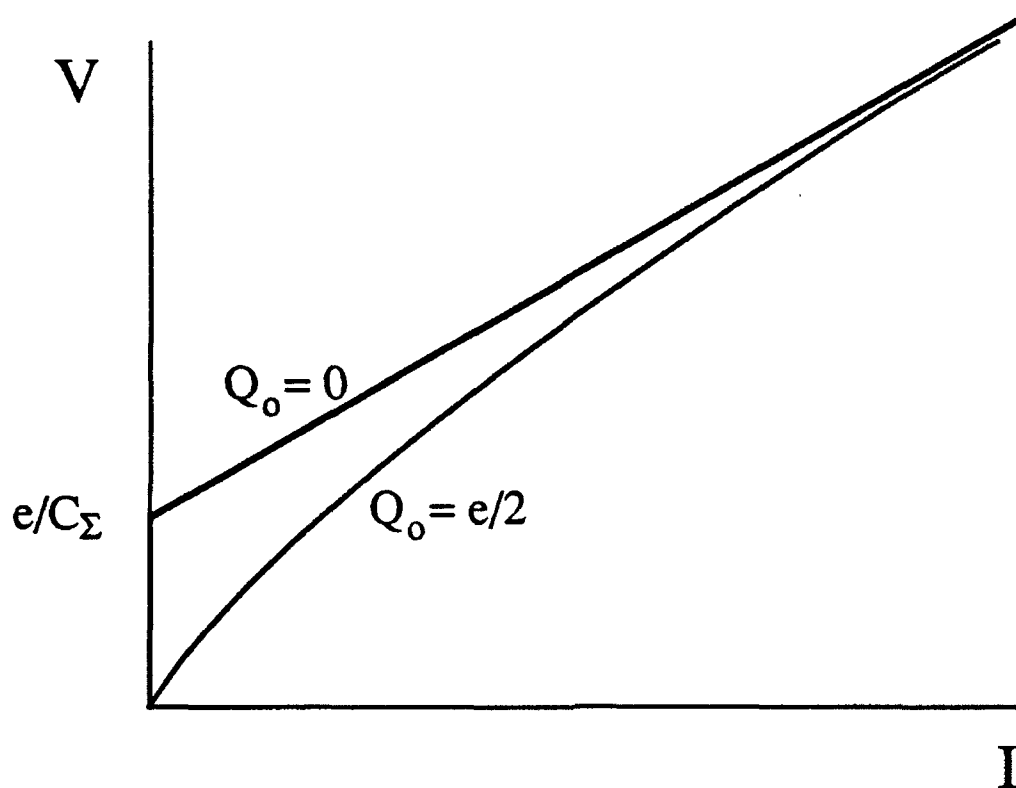


Figure 2-9.

Schematic I-V curves for the two junction system for different values of Q_0 . For $Q_0 = 0$, we see the Coulomb blockade region of zero conductance. However, for $Q_0 = -e/2$, current flows for all non-zero voltages. These curves are for the symmetric junction case, $C_1 = C_2$. For asymmetric junctions, steps in the I-V curves are measured, resulting in the so-called Coulomb staircase.

electrons to tunnel onto or off of the island ($n = 0 \rightarrow n = 1$ or vice versa), current may flow for arbitrarily small bias voltages. $V_t = 0$ in this case.

Figure 2-9 shows the I-V curve for this $Q_0 = -e/2$ case. As $V_t = 0$, there is no Coulomb blockade region. Not given by the simple formalism, however, is that the curve for $Q_0 = -e/2$ asymptotically approaches the $Q_0 = 0$ curve. This is true for all values of Q_0 .

2.4 Charging Arrays

We conclude this theoretical overview with a discussion of charging arrays. In Sec. 2.4.1 we describe the capacitive energy for the array E_{array} . Section 2.4.2 introduces solitons and Sec. 2.4.3 discusses the array I-V characteristics and possible commensurate effects.

2.4.1 Capacitive Energy of a 2D Array

The total capacitive energy of an array is simply the sum of the energies for each capacitor, $CV^2/2$

$$E_{array} = \sum_{\langle i,j \rangle} (V_i - V_j)^2 C / 2 + \sum_i (V_i - V_o)^2 C_o / 2 \quad (2.34)$$

where the sum $\langle i, j \rangle$ is over nearest neighbor pairs, C_o is the capacitance between an island and the underlying ground plane (the ground plane serves as the gate electrode for these arrays), and V_o is the ground plane voltage. V_i represents the voltage level on the i^{th} island, and can be related to the island charge Q_i by

$$\sum_{\langle j \rangle} C(V_i - V_j) + C_o(V_i - V_o) = Q_i \quad (2.35)$$

where the sum $\langle j \rangle$ is taken over the four nearest neighbor islands to island i . We can also write this in matrix form

$$\bar{Q} = \bar{C} \bar{V} \quad (2.36)$$

where \bar{Q} and \bar{V} are vectors whose elements Q_i and V_i correspond to the i^{th} island, and \bar{C}

is a tensor whose elements C_{ij} give the capacitance between the i^{th} and j^{th} island ($C_{ii} \equiv C_o$). \bar{C} can also include elements corresponding to “stray” capacitances between non-nearest neighbor islands.

Often, we wish to calculate the energy E_{array} for a given charge configuration \bar{Q} . To perform this, we rewrite Eqn. (2.36) as

$$\bar{V} = \bar{C}^{-1} \bar{Q} \quad (2.37)$$

and use the voltages \bar{V} in Eqn. (2.34) to determine E_{array} . One drawback to this method is that it involves inverting \bar{C} , which for an N by M array is an NM by NM tensor. Therefore, for all but the simplest charge configurations, this problem must be solved numerically.

2.4.2 Solitons

For the case of a single charge (electron or hole) placed into an otherwise neutral array, Bakhvalov, *et al.* (1991) showed that the resulting voltages \bar{V} may be determined analytically. For an electron or hole on island i_o , the surrounding voltages form a near axial-symmetric distribution¹

$$V_i = \begin{cases} \frac{\pm e}{2\pi C} \ln \frac{1}{r} & \text{for } 1 \ll r \ll \lambda_o^{-1} \\ \frac{\pm e}{2\sqrt{\pi} \left(C \sqrt{C_o^2 + 4CC_o} \right)^{1/2}} \frac{e^{-\lambda_o r}}{\sqrt{r}} & \text{for } r \gg \lambda_o^{-1} \end{cases} \quad (2.38)$$

where r is the radial distance away from island i_o (in units of the array lattice spacing),

¹The symmetry is distorted near islands i_o due to the array discreteness.

and λ_o^{-1} is a characteristic distance given by

$$\lambda_o = \ln \left[\left(1 + \frac{C_o}{2C} - \sqrt{\left(\frac{C_o}{2C} \right)^2 + \frac{C_o}{C}} \right)^{-1} \right] \quad (2.39)$$

For $C_o \ll C$, Eqn. (2.39) reduces to $\lambda_o \approx \sqrt{C_o/C}$. Figure 2-10 shows this potential, which graphically represents a soliton.

Unlike vortices, solitons do not have to overcome barriers to pass from island to island (sufficiently far away from the array edges), as the following argument shows. With vortices, the high energy position occurs when the vortex sits on top of a junction, *i.e.*, the saddle-point between two pinning wells. The phase difference across the junction is π , leading to the maximum junction energy of $-E_J \cos \phi|_{\pi} = E_J$. The vortex does not like to sit in this position due to this large energy (this simple argument neglects the energies of all of the other junctions, which must be taken into account in more rigorously addressing this question). With solitons we follow the same line of reasoning, though reach a different conclusion. If an energy barrier for solitons to move from island to island exists, it would occur where the soliton was “halfway between” the two islands. We can think of this in-between case as both islands sharing the soliton, *i.e.*, each having a charge of $e/2$. The charge on the junction between the two islands for this case is zero, resulting in *zero* energy. Therefore the soliton would like to sit in this position if possible, as it represents a lower energy than if it sat on one island alone (again, one must calculate the energies of all the junctions to prove this rigorously). Therefore, though solitons cannot take advantage of this position due to charge quantization, it represents a low energy configuration and does not act as a barrier.

Mooij, *et al.* (1990) predict that solitons interact logarithmically with the interaction potential U given by

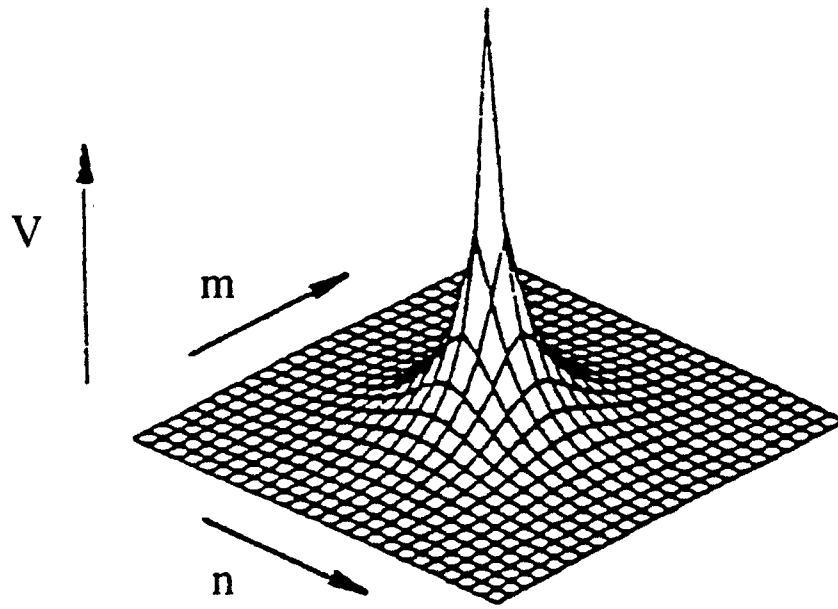


Figure 2-10.

Configuration of voltage levels as a function of position for a single charge placed on an island in an otherwise neutral array [Bakhvalov, *et al.* (1991)]. We refer to the charge and the surrounding “dressing” as a soliton. For this figure, Bakhvalov, *et al.* choose $C_o/C = 0.1$.

$$U = \mu_{core} + (E_c / \pi) \ln r \quad r \ll \lambda_o^{-1} \quad (2.40)$$

where μ_{core} represents the energy of two solitons one lattice spacing apart (core energy). For $r \gg \lambda_o^{-1}$, U falls off exponentially. Like vortices, solitons of similar charge repel while those of opposite charge attract. The logarithmic form is derived with the approximation that the system is two-dimensional, as if the solitons were line charges. However, if we allow that in the actual arrays fringing fields will make the system quasi-three dimensional, it is uncertain what form the potential U will take. D. S. Fisher (private communication) argues that the interaction will not be logarithmic, but short range in nature.

In a rectangular array, the electrostatic energy of a soliton is lowered by proximity to an edge electrode and raised by proximity to a free edge. In analogy to the Bean-Livingston surface barrier for vortices in type II superconductors [Bean and Livingston (1964)], Bakhvalov, *et al.* discuss this in terms of image charges: at an edge electrode a soliton is mirrored by an antisoliton to which it feels an attraction; at free edges a soliton is mirrored by a soliton of like charge and hence repulsion occurs.

2.4.3 I-V Characteristics and Commensuration Effects

Similar to the double junction system, these arrays show a Coulomb blockade region in which no current flows [see Fig. 1-4(b)]. For arrays, the blockade occurs because at low bias voltages, solitons cannot overcome their attraction to the edge electrodes and move through the array to contribute to a current. Above some threshold voltage V_t , however, the force due to the voltage bias is strong enough to separate the solitons from their image charges and pull them through the array. The I-V curve then approaches an asymptote which, like the case of the double junction, extrapolates back to a finite offset voltage V_{off} . We discuss the nature and theoretical estimations of V_{off} and V_t in more detail in Chapter 6.

Bakhvalov, *et al.* (1991) predict that it is possible to induce solitons to sit in an array by applying an external *electric* field (generated by applying a voltage V_g between the array and the ground plane). The density of these field-induced solitons is proportional to the strength of the electric field. As with vortices, these solitons move to form lattices which minimize the repulsive energy. At certain densities, they are predicted to form a lattice commensurate with the array lattice. For example, we might imagine a " $f = 1/2$ " state [see Fig. 2-5(a)] in which solitons occupy every other island in a checkerboard-like pattern. These lattices have not yet been observed, either numerically or experimentally. This may be due to the array sizes being too small so far, so that the soliton interaction with the array edges interferes with the formation of a commensurate lattice.

CHAPTER THREE

DESCRIPTION OF EXPERIMENT

This chapter describes the design, fabrication, and measurement of arrays. Section 3.1 discusses the array design, made unintuitive by the constraints of shadow evaporation. Section 3.2 describes the array fabrication, including photolithography, electron beam lithography, development and evaporation steps. Sections 3.3 and 3.4 detail the set-up for the electrical measurements and refrigeration, respectively. Included in Sec. 3.3 is a description of the method of feeding microwaves to the sample at cryogenic temperatures.

We study ten samples, the first six made with Sn-SnOx junctions, and #7 through #10 made with Al-AlOx junctions. Though the tin and aluminum arrays have the same general design, and are made with the same general procedures, many specific details are different. We will describe differences as they arise, but will place more emphasis on the aluminum arrays as (1) they are closer to representing the current "state of the art" and (2) much pertinent information on making tin junctions may be found in Iansiti (1988). Specific information on the ten samples may be found in Table 4-1 (samples #1 - #5), Table 5-1 (#6 and #7), and Table 6-1 (#7 - #10).

3.1 Array Design

The arrays discussed here all consist of a 2D lattice of islands, with each island connected to its nearest neighbor through a Josephson junction. The arrays have a square unit cell: every island, not at an edge, has four nearest neighbors. The majority of the arrays we measure have 50 by 70 unit cells. Two opposite sides of the array are connected

to bus bars, each connected to every island on its side through a lead. Each bus bar is then connected to a pair of pads, one for current injection and the other for voltage measurement (see Fig. 3-3). In the superconducting state, the bus bars have zero resistance so that this configuration results in "four probe" measurements. In the normal state, the bus bars will have a non-zero resistance so that the lead configuration results in "two probe" measurements. However, the sample differential resistances in the normal state are all greater than or equal to R_n , typically on the order of tens of $k\Omega$ s for our samples. As the longest and thinnest bus bar we use for the normal state measurements has an estimated resistance of $20\ \Omega$ at room temperature, we expect that these small resistances will not noticeably affect our results.

The method of fabricating the junctions using a shadow evaporation technique puts certain constraints on array design. We are restricted to having junctions along one direction; the horizontal direction, for example, if one looks straight down on the pattern. We can still achieve a square unit cell, though we have to use the brick-like pattern shown in Fig. 3-1(a).¹ As Figs. 3-1(b) and 3-1(c) show, this pattern does reduce to a square unit cell. Also indicated in Fig. 3-1(c), the principal axes of the array lie at non-horizontal and vertical angles. Thus, to achieve a 4 by 7 array which resembles that in Fig. 3-1(d), we must use a pattern like that in Fig. 3-1(f) [Figure 3-1(e) shows schematically the translation between the two]. The majority of arrays we measure have 50 rows by 70 columns, with bus bar arrangements as in Fig. 3-1(d). The current direction is along the rows, so that the current must pass through a minimum of 70 junctions. (We fabricated samples #3 and #5 before we fully understood the diagonal nature of this design and how to compensate for it. We refer to these 10 by 10 arrays as "diamond" arrays. Appendix A gives schematic drawings of their design.)

At the edges of the array, we find it important to add extra structures. In electron beam lithography the majority of the electron beam exposes only the points on which it is

¹While the aluminum arrays have a design which permits both horizontal and vertical lines, similar constraints exist that restrict us to use essentially the same brick-like pattern.

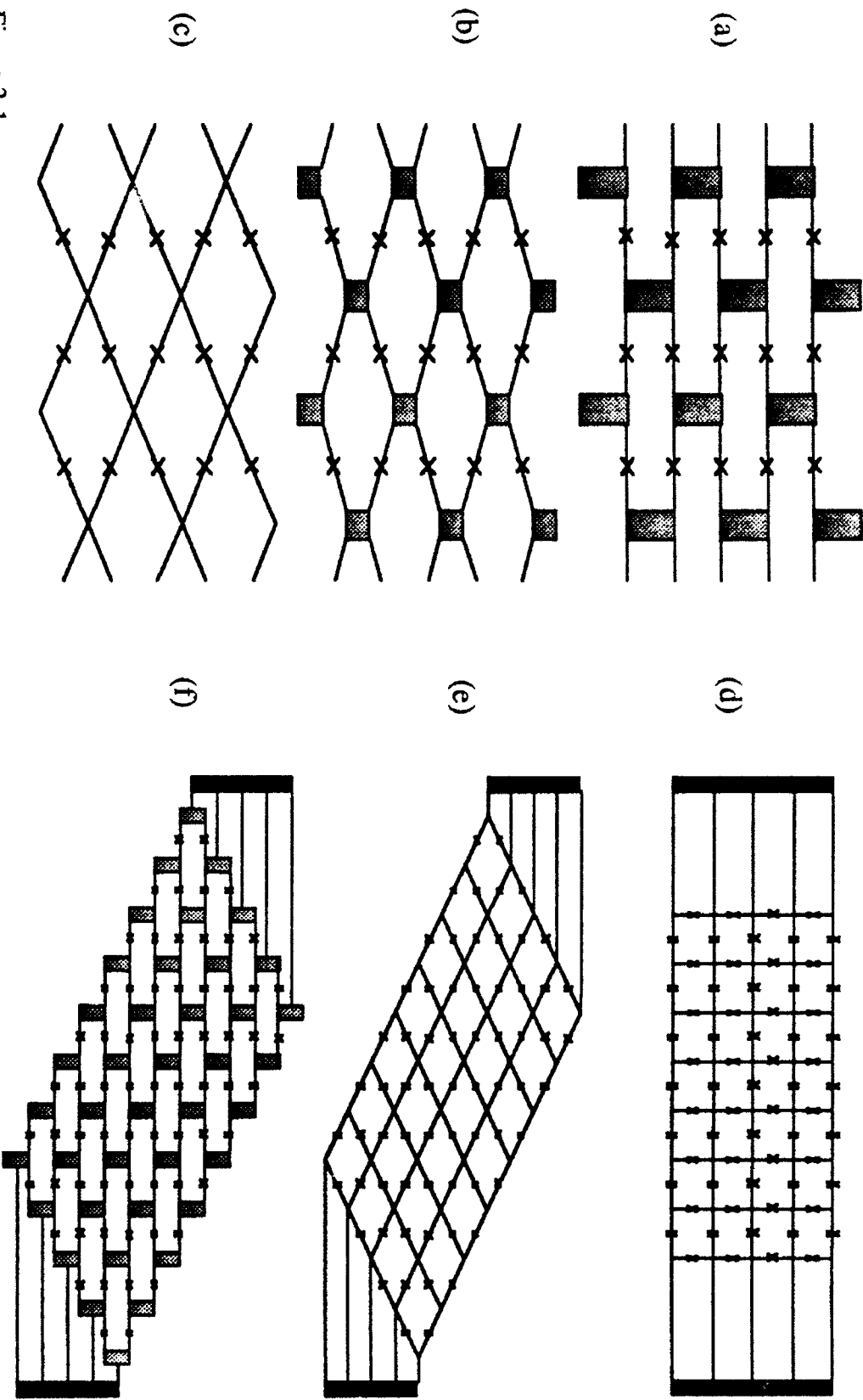


Figure 3-1.

Figures 3-1(a) through 3-1(f) show the geometry of our arrays and how they translate to a more intuitive design. In (a) we see the configuration used for the tin arrays. By squeezing the rectangles (b) we arrive at a more familiar pattern (c). Figure 3-1(d) shows a 4 by 7 rectangular array. Translating it via (e), we see how this is realized (f) using the brick-like pattern of (a).

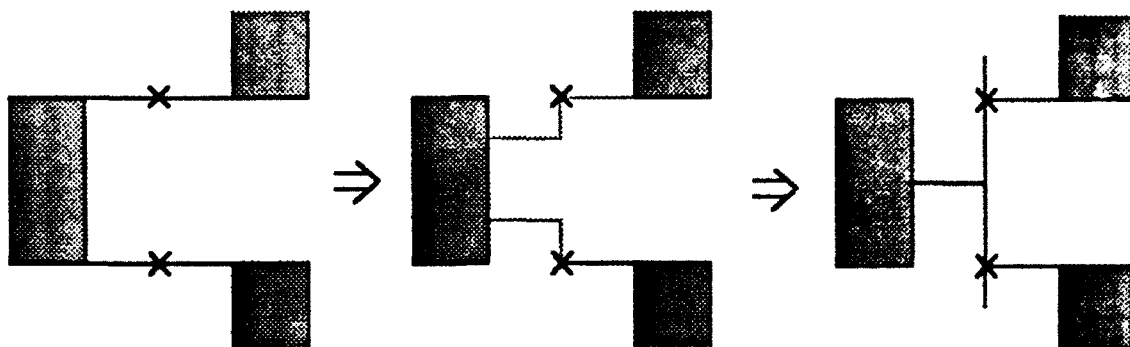


Figure 3-2.

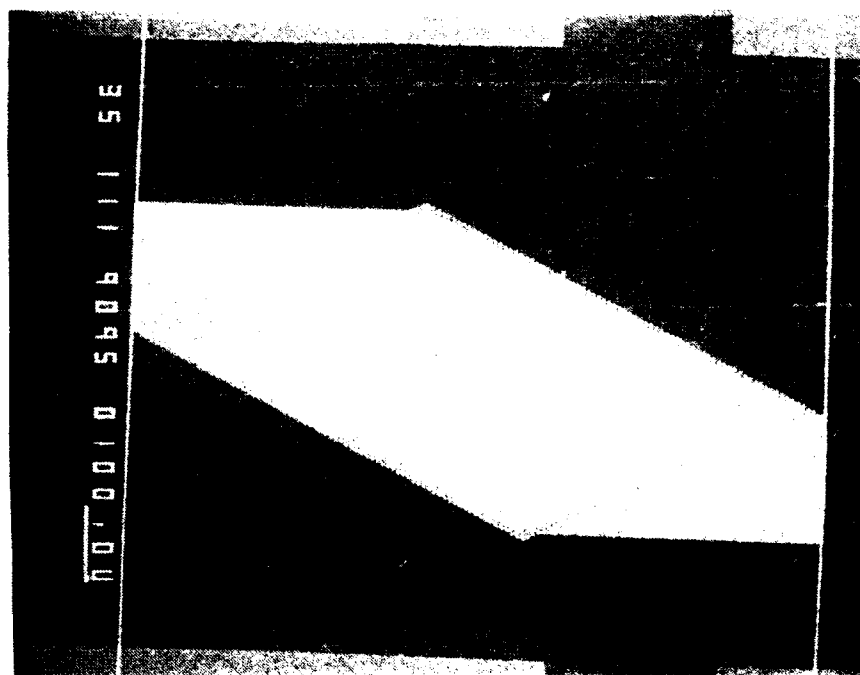
This figure shows how the pattern used for the tin arrays transforms into that used for the aluminum arrays. Electronically, the two patterns are equivalent.

focused. However, a small fraction of the beam, and electrons which have been back-scattered from the resist or substrate, expose the surrounding areas as well. This cross-exposure means that two lines exposed one micron apart will each receive a higher exposure than two lines exposed ten microns apart. Therefore, to assure that the outside edges of the array receive roughly the same amount of cross-exposure as those inside the array, we add two extra rows per side of the array. These rows mimic the array pattern, but are designed not to change the array's electrical configuration.

For the aluminum arrays, we use a slightly different unit cell. Seen in Fig. 3-2, we change two lines to get junctions formed with perpendicular lines. We will discuss the reasons for this change below. Going to this new configuration does not appreciably change the geometry of the array.

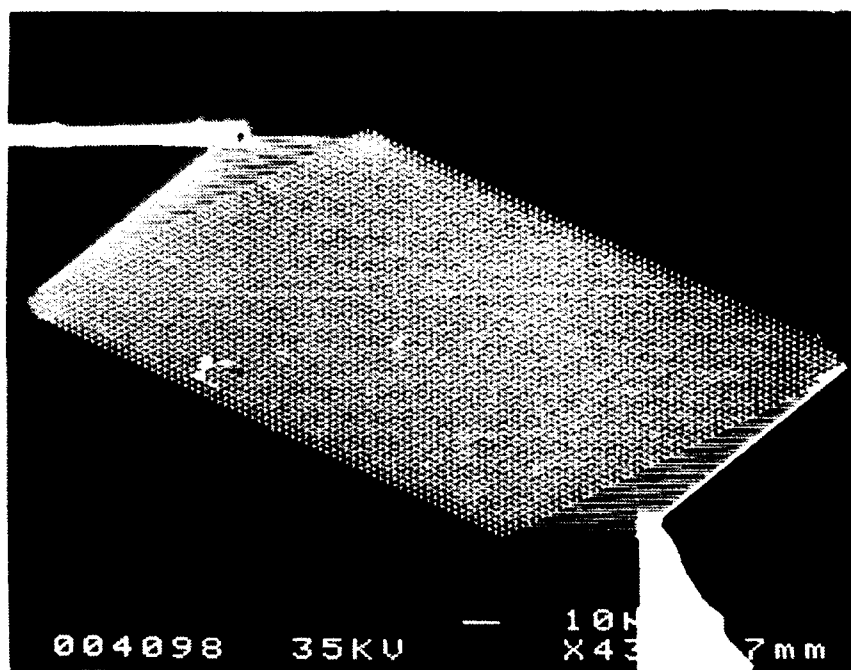
Figures 3-3, 3-4, and 3-5 show pictures of the tin and aluminum arrays. In Fig. 3-3, we see two arrays of size 50 by 70 unit cells, and the leads connecting the array to the pads-(a) shows a tin array and (b) shows one made from gold, which simulates the size and dimensions of the aluminum arrays. The substantially smaller size of the aluminum array reflects advances in our equipment and methods. In Fig. 3-4 we see the unit cells for the tin and gold (aluminum) arrays, and in Fig. 3-5 we see the individual junctions. The

(a)



— 100 μm

(b)



— 10 μm

Figure 3-3

Scanning electron microscope (SEM) micrographs showing pictures of (a) sample #4, a 50 by 70 tin array and (b) an array made out of gold with the same size and dimensions of samples #7-#10, 50 by 70 aluminum arrays (aluminum does not show up well in the SEM). Note the difference in physical dimensions of the two arrays: the bar (vertical) in (a) is 100 μm long, while the bar (horizontal) in (b) is 10 μm long.

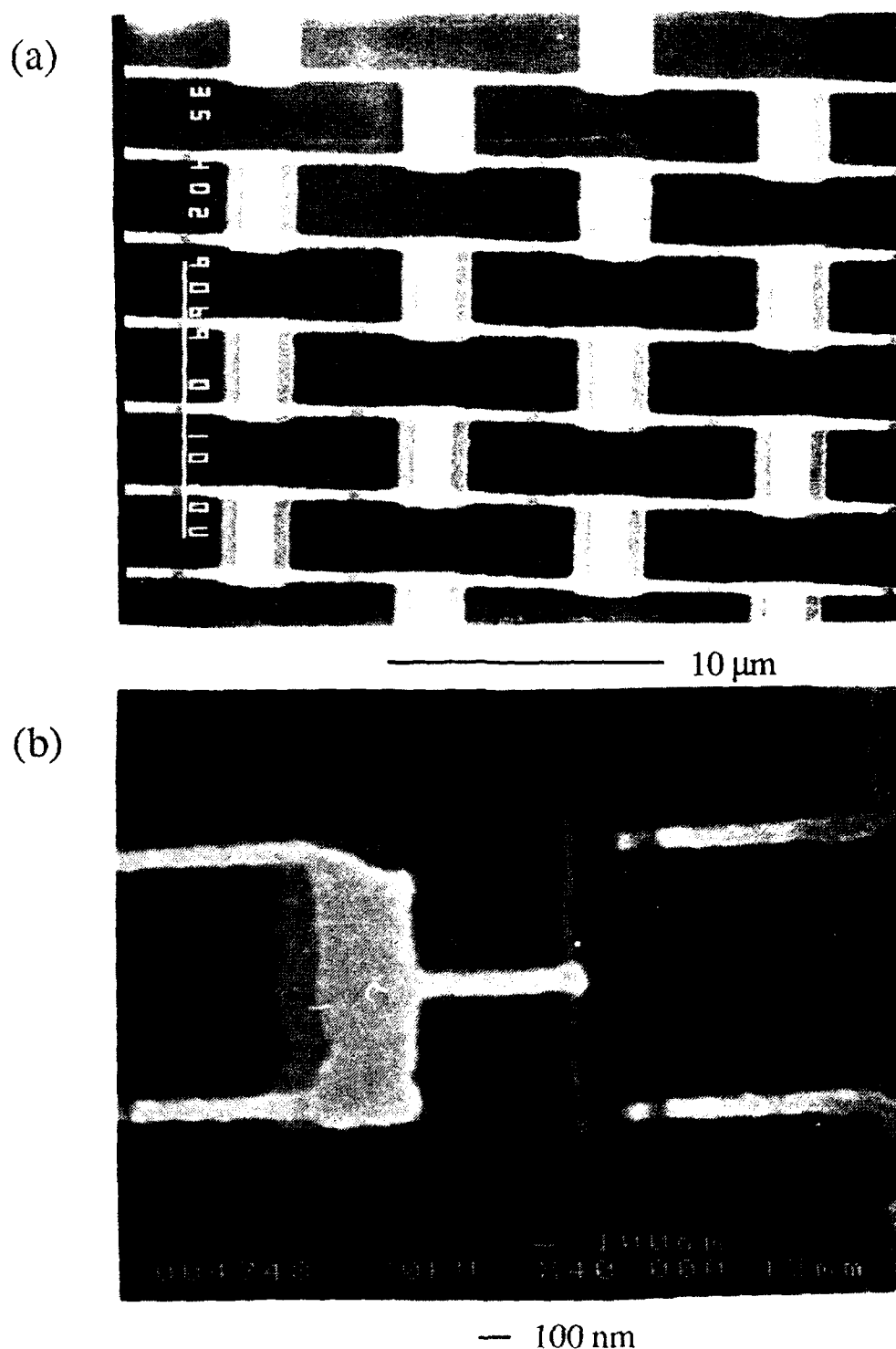


Figure 3-4

This figure shows pictures of (a) the unit cells for sample #1, a tin array and (b) an island in the gold array (which simulates the aluminum arrays, samples #7-#10). In (a), the vertical bar is 10 μm in length, while for (b), the bar is horizontal bar is 0.1 μm in length.

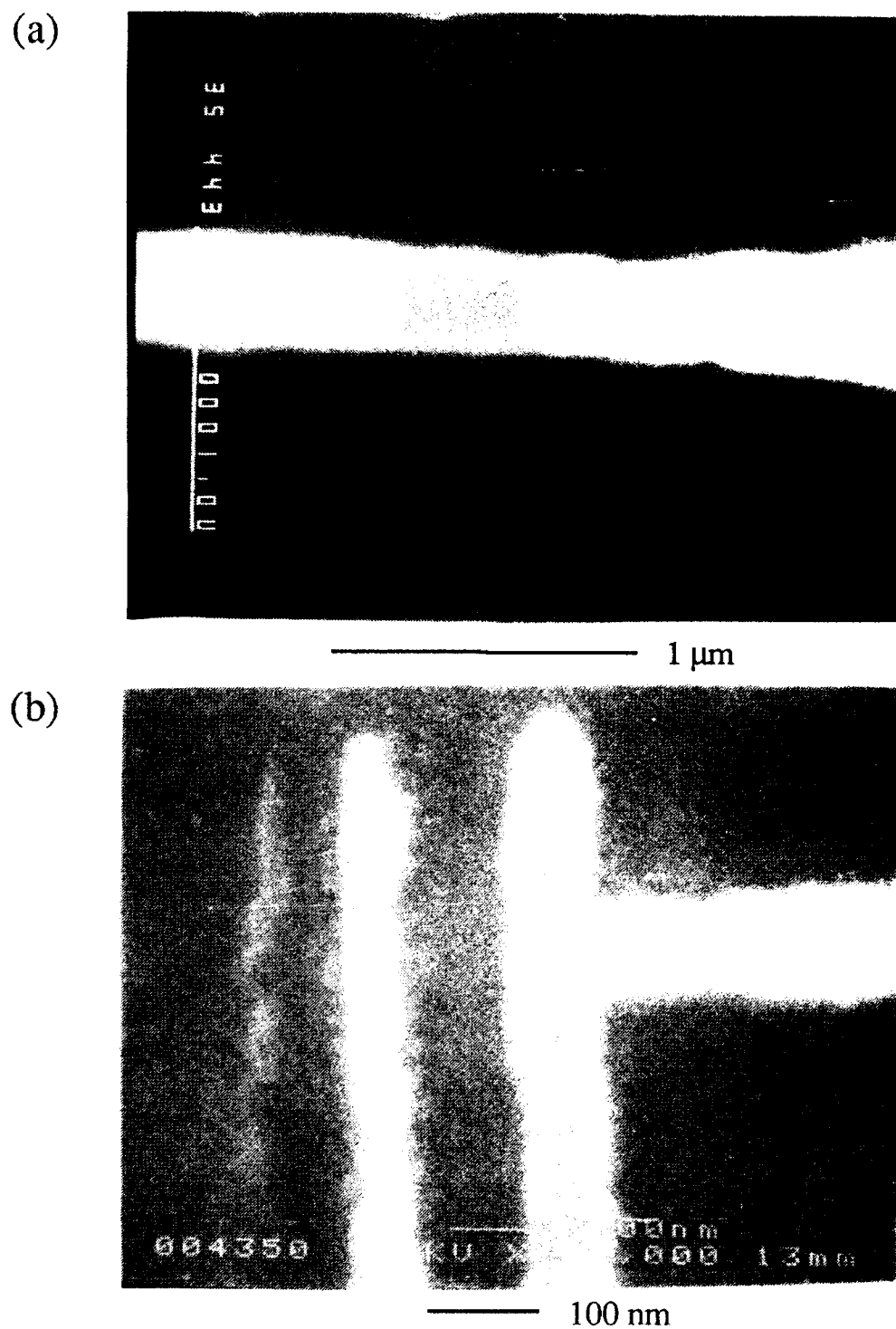


Figure 3-5

This figure shows pictures of individual junctions in (a) sample #1, a tin array and (b) the gold sample (which simulates the aluminum samples #7-#10). To the side of the pictures, the vertical bar in (a) is 1 μm long and the horizontal bar in (b) is 0.1 μm long.

gold (aluminum) junction in Fig. 3-5(b) is roughly 30 times smaller in area than the tin junction in Fig. 3-5(a).

3.2 Fabrication

At a basic level, fabricating arrays of small Josephson junctions is a simple extension of fabricating single small Josephson junctions, first pioneered at Bell Labs [see for example Dolan (1977), Dolan, *et al.* (1981), and Hu, Jackel, and Howard (1981)], and used in this group by Iansiti (1988) and Johnson (1990). These works serve as useful sources of information, much of which we will only summarize here. However, fabricating an array does present a host of specific problems, many derived from (1) problems associated with the size of the array and (2) cross-exposure, described above.

3.2.1 Photolithography

We use 2" diameter oxidized silicon wafers for our substrates. The wafers measure about 250 μm thick with an oxide cap of approximately 1000 Å. The doping of the silicon is unspecified, but should not contribute to the conduction due to both the oxide layer and the low temperatures used (the carriers from the dopants should freeze out at dilution refrigerator temperatures).

We clean the wafers before patterning the contact pads and again before patterning the array. The cleaning method consists of boiling the substrates in photoresist stripper for 5 minutes, followed with an ultrasound bath for 10 minutes. This is then repeated four more times using first soap and water, then trichloroethylene, acetone, and finally methanol. A full description of this process may be found in Smith (1989).

We pattern the electrical contact pads with a three layer, photoresist-aluminum-photoresist technique described by Danchi (1982) or with a photoresist layer soaked in chlorobenzene described by Iansiti (1988). As these two theses go into the techniques in

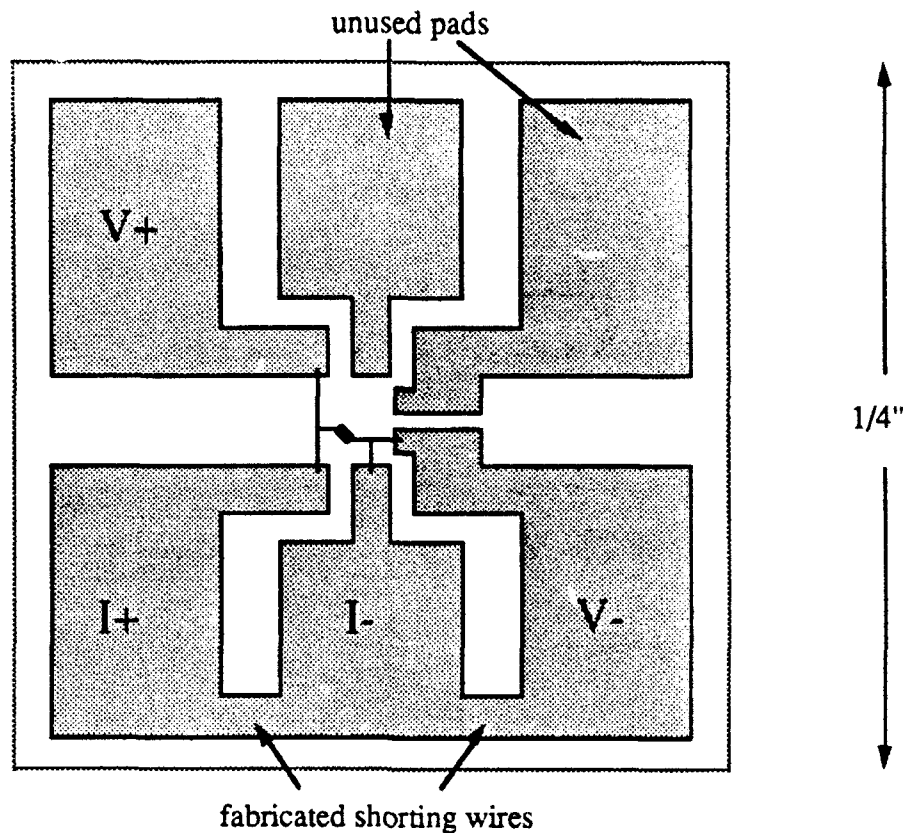


Figure 3-6.

This figure shows the pad layout used for many of the samples, with $V\pm$ and $I\pm$ representing typical configurations for the voltage and current leads. The small inclined rectangle in the center of the pads represents the array. The fabricated shorting wires are "cut" by scratching through them with a diamond-tipped scribe. We do this after the sample is mounted on the dilution refrigerator slug.

detail, we will not discuss them here. For the contact pads we deposit 200 - 500 Å of gold on top of 10 - 20 Å of chrome, the chrome providing the gold good adhesion to the substrate. We use the thinner pads for the aluminum arrays, where the total thickness of the aluminum layers is approximately 500 Å. In Fig. 3-6 we see the layout of the contact pads. Each pad set measures 1/4" on a side, so that 30 to 40 pad sets can be diced from one wafer.

Dust poses a large problem to the patterning of these arrays. The largest source of dust

comes from the wafer itself: scribing and cleaving a wafer into the individual pad sets generates silicon particulates. We have found that no amount of cleaning can then remove these particles. To remedy this problem we coat the wafer with a layer of photoresist before scribing it. The silicon dust then lands on the photoresist layer and is removed as the photoresist is removed when the individual pad sets go through the cleaning process mentioned above. This process increases the yield of dust-free pad sets to almost 100%.

3.2.2 Electron-beam Lithography

Electron-beam (e-beam) lithography works by exposing a layer of material, called resist, with an electron beam. The resist is sensitive to high-energy electrons; when exposed, the molecules which make up the resist break down and become soluble in a developer. By controlling the beam, we can use it, like a sharpened pencil, to write any pattern.

We use a bilayer technique in fabricating the array. The bottom layer consists of PMMA (polymethylmethacrylate) mixed with MAA (methacrylic acid), while the top layer consists of PMMA alone. The PMMA/MAA mixture is more sensitive to electrons, thus helping to provide the wide undercut needed to use the shadow evaporation technique. In Fig. 3-7(a) we see a view of the electron beam exposing the bilayer. The electron beam widens as it reaches the bottom layer due to scattering. In addition, the bottom layer receives a higher dosage of electrons as they also backscatter from the substrate. We make backscattering more prominent by choosing a relatively low accelerating beam voltage, between 12 and 20 keV. The combination of being exposed to a more spread-out beam, being exposed to backscattered electrons, and the higher sensitivity of the PMMA/MAA mixture leads to a large undercut, as seen in Fig. 3-7(b).

In choosing the thickness of the bottom resist layer we adhere to the general rule of thumb that it should be at least three times as thick as the total thickness of the metal deposited. This prevents tearing during liftoff. The top resist layer must be thick enough so that it does not sag in the regions of undercut [the overhang as seen in Fig. 3-7(b)]. The

lower limit of the *sample* thickness is determined by the amount of metal we must deposit to form a continuous path. For aluminum we use layers as thin as 200 Å, which we find to be continuous. With tin, however, we require thicker layers; 1000 Å or more. Also, with the shadow evaporation technique described in the next section, in separate evaporations we deposit overlapping wires. We make the second layer of the evaporation roughly twice as thick as the first layer to be sure that, evaporated at a high angle, it does not have any breaks due to the shadowing of edges of the first layer. Table 3-1 shows all of the relevant information concerning the e-beam resist layers for both the tin and aluminum samples, as well as the thicknesses of metallic layers.

To create ultrasmall junctions, we use a special technique called shadow evaporation. In this method we use two evaporations at different angles to create an overlap: the junction region. For this to work correctly, we need to create a suspended “bridge” of resist. In Fig. 3-8(a) we see how to create a bridge of resist by bringing the end of one line close to another, perpendicular line, or by bringing the ends of two lines close together [Fig. 3-8(b)]. With the resist system designed to give a large undercut, one needs only to bring the lines together to within 1 μm for the tin arrays and 0.15 μm for the aluminum arrays to get a resist bridge (for the aluminum arrays we need a much smaller gap due to the thinner bottom resist layer).

We use a 3 to 1 mixture of isopropanol and MIBK (methylisobutylketone) as a developer. This can be bought commercially as PMMA Rinse (KTI Chemicals; Wallingford, CT). If mixing by hand, one must be alert that MIBK is sold under different names, such as 4-Methyl-2-Pentanone (Aldrich; Milwaukee, WI). For the tin and aluminum arrays we develop for 10 and 5 minutes respectively. After developing, we use pure isopropanol as a stop bath.

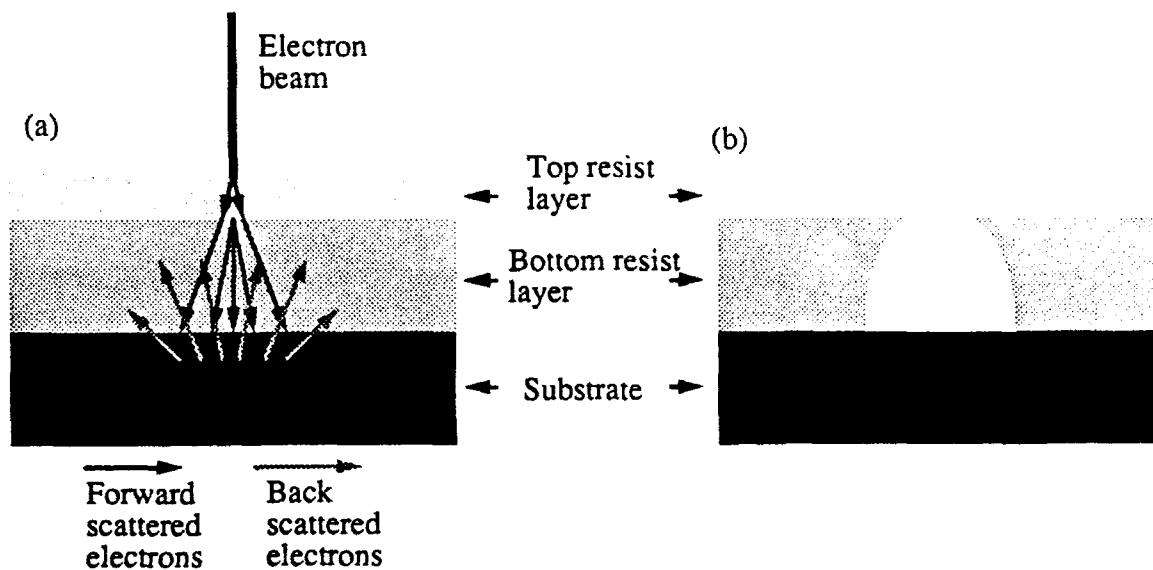


Figure 3-7.

Side view of resist system (a) being exposed by an electron beam and (b) after development.

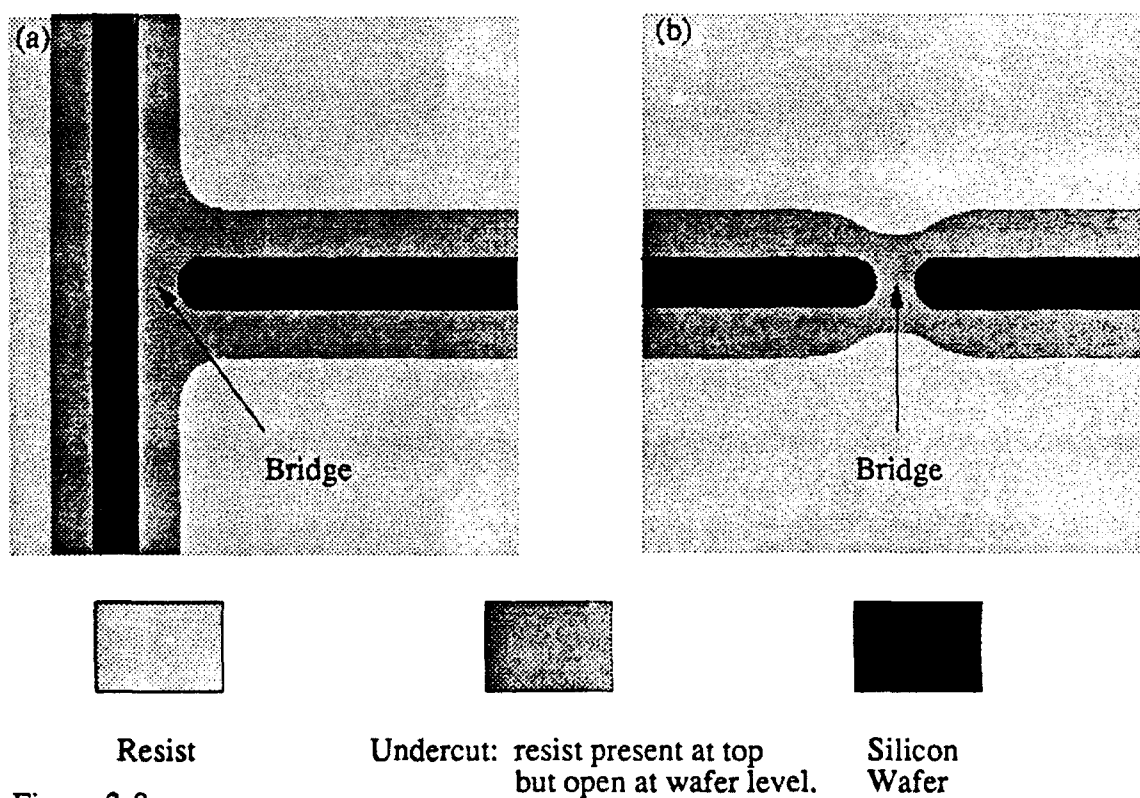


Figure 3-8.

Top view of resist showing method of creating resist bridge with (a) perpendicular lines and (b) parallel lines.

	Resist			Metal	
	Material	Spin rpm " time	Bake temp. " time	Thickness	Thickness ¹ Evap. Angle
Tin Resist: bottom layer Metal: first evap.	PMMA/MAA 0.12 gm/ml in acetic acid	3500 rpm 45 sec.	180 degrees C 1 hour	6400 Å	1250 Å (1100 Å) -25 degrees
Tin Resist: top layer Metal: second evap.	PMMA 4% in Chloro- benzene	8000 rpm 45 sec.	180 degrees C 1 hour	1850 Å	2000 Å (1800 Å) 25 degrees
Aluminum Resist: bottom layer Metal: first evap.	PMMA/MAA 0.06 gm/ml in acetic acid	4500 rpm 45 sec.	180 degrees C 1 hour	2000 Å	200 Å (200 Å) 0 degrees
Aluminum Resist: top layer Metal: second evap.	PMMA 1.5% in Chloro- benzene	8000 rpm 45 sec.	180 degrees C 1 hour	425 Å	600 Å (400 Å) 45 degrees

¹ The first number gives the value deposited as read on the DTM. The number in parentheses gives roughly the value deposited normal to the substrate surface.

Table 3-1.

This table gives various parameters for top and bottom resist layers, and for the metal layers deposited in the first and second evaporations (See Fig. 3-9). Information concerning resist is found on the left side of the dashed line while information on the metal is on the right side.

3.2.3 Evaporation

We use this resist bridge, along with an angle evaporation, to fabricate small junctions. Here, we will discuss only the procedure used in making the junctions formed with perpendicular lines (used in the aluminum arrays). The procedure for the parallel lines (tin arrays) is similar, except as noted.

As seen in Fig. 3-9(a), we perform the first evaporation straight down.¹ We typically use a rate of 10 Å/second for aluminum and deposit 200 Å for the first layer.² We then oxidize the aluminum (this oxide forms the insulating layer of the junction) by letting in a small amount of oxygen gas into the chamber. We typically allow the sample to see 50 mtorr of oxygen gas for 3 to 10 minutes. For the tin arrays we find it necessary to use an oxygen dc plasma for oxidation. The junction normal state resistance R_n increases with the oxidation time. We then change the angle of the sample and perform the second evaporation. We change the angle of the rotating stage on which the sample sits by means of a speedometer cable fed into the chamber through a rotary feedthrough. For the aluminum arrays, we change the angle to 45°. With the second evaporation, we put down a layer of 400 Å at a similar rate.³ As Fig. 3-9(b) shows, this creates just a small area of overlap: the junction region.

After evaporation, we use acetone as the solvent for liftoff. Frequently we need to place the arrays in an ultrasonic bath to get all of the excess metal off. Using ultrasound does not appear to damage the junctions in any way.

For the aluminum arrays we go to forming junctions with perpendicular lines for considerations of junction uniformity. As seen in Fig. 3-5(a), the ends of lines are rounded. As each end, and hence each overlap, is slightly different this leads to different

¹For the tin arrays, we cool the sample stage to 77 K during evaporation. For the aluminum arrays, however, the stage is kept at room temperature.

²For tin we use a rate of roughly 100 Å/sec.

³The nominal thickness is equal to the thickness deposited [as measured by a digital thickness monitor (DTM)] times the cosine of the angle between the normal of the substrate and the line of sight between the sample and the crucible. Therefore, at an angle of 45° we must deposit roughly 600 Å of metal as measured by the DTM to get a nominal thickness of 400 Å.

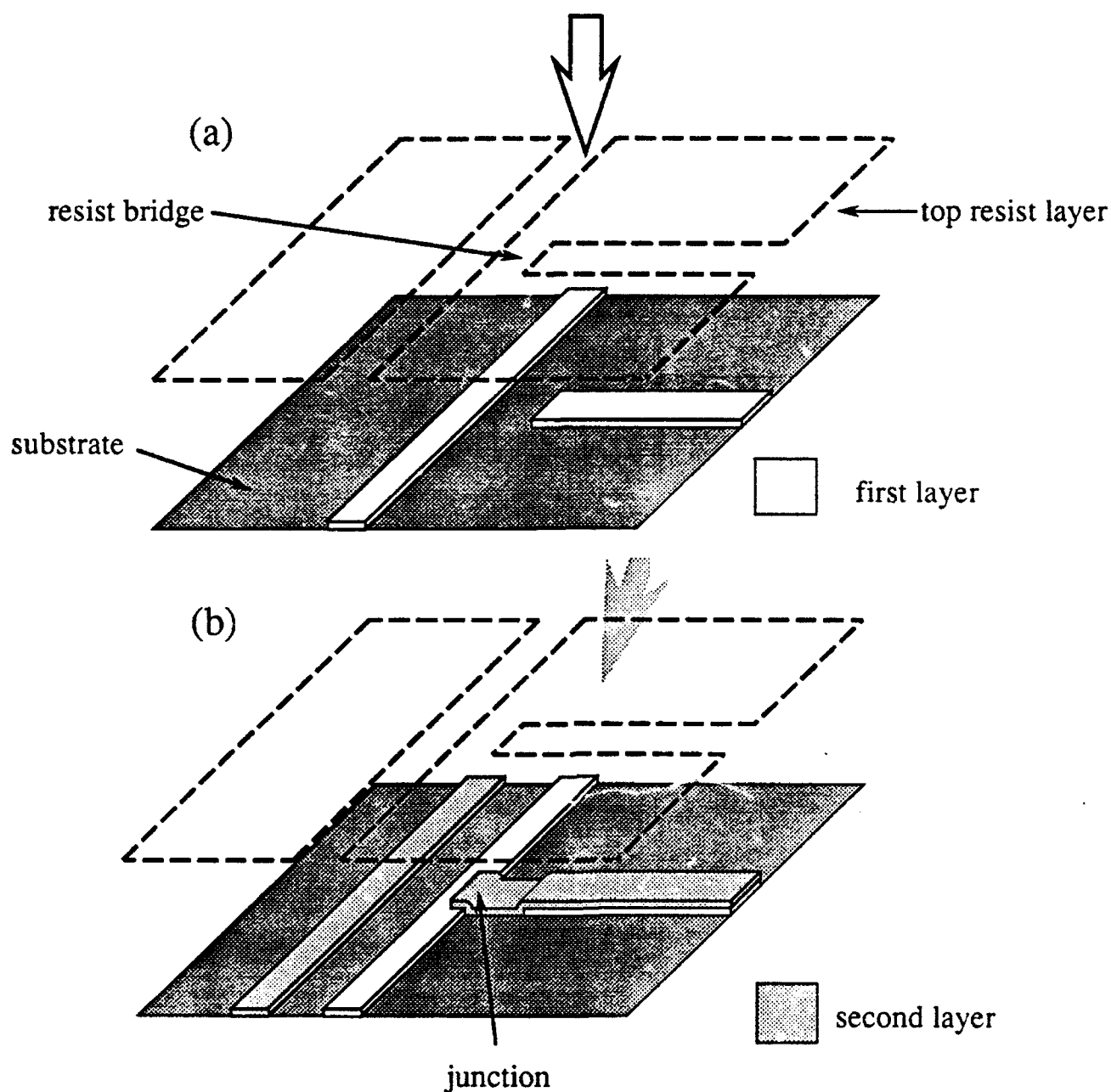


Figure 3-9.

We form a junction with two evaporations. Using the pattern in Figure 3-8(a), in drawing (a) we evaporate straight down then oxidize (oxidation step not shown). We perform a second evaporation (b) at an angle of about 45 degrees, forming an overlap. In a correctly designed circuit, the line to the far left in (b) will not short out any circuit elements.

junction areas within an array. However, the width of the lines is fairly constant away from the ends. To achieve more uniform areas we can lay one line across another to form a cross. However, this leads to larger junctions as the linewidth away from the ends is as much as 50% larger than that right near the end. As a compromise to achieve the maximum junction uniformity without sacrificing too much in junction size, we form the junctions by crossing lines, but not crossing them entirely [shown in Fig. 3-9(b)].

3.3 Measurement

With these arrays we perform transport measurements. In the following two sections we describe first, the circuitry used for the dc characterization of the array and second, the inclusion of microwave irradiation.

3.3.1 DC Set-Up

To connect the array, through the contact pads, to the current and voltage leads we use an indium "sandwich" technique. First, an indium dot (thin slice of indium wire) is placed on a pad. After laying the sample wire on the dot, another dot is added on top and pressed down with the blunt end of a small Allen wrench (or similar tool), forming a sandwich. This technique works well as long as vacuum grease and similar substances which hinder adhesion are kept off of the contact pads.

We then mount the sample so that any applied magnetic field is normal to the array. On the slug used for the dilution refrigerator, we place the sample as seen in Fig. 3-10. We feed the leads through 1 to 5 k Ω resistors. These resistors help in preventing voltage spikes, which occur during the top-loading procedure, from damaging the sample. They may form a low-pass filter with the lead capacitance, thereby reducing the noise which reaches the sample.

For samples #6 and after, we employed microwave filters in the dilution refrigerator to

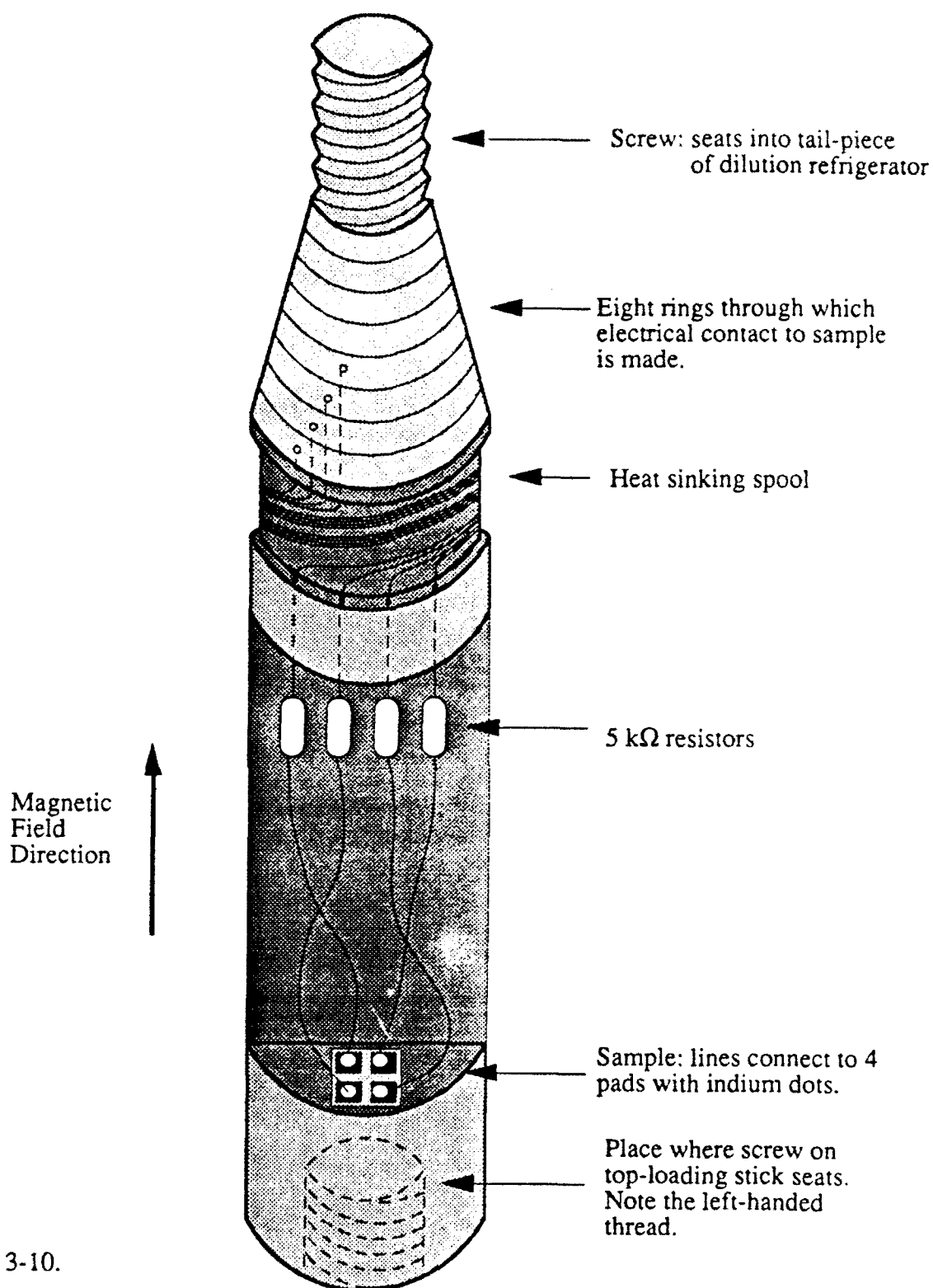


Figure 3-10.

Schematic drawing of the dilution refrigerator slug. The sample sits on the flush end of the sample area so that the magnetic field is perpendicular to the plane of the array. Each ring at the top is electrically connected to a lead (only four are in use here). These rings mate to counterparts in the refrigerator tail when the slug is top-loaded (see Fig. 3-13). When mounted in the refrigerator the slug sits upside-down from the position shown.

prevent microwave noise from getting down the leads and affecting the measurements. First employed by Martinis, *et al.*, (1987) these microwave filters consist of a container filled with fine copper powder mounted onto the mixing chamber. We run the sample leads through this copper powder. The copper particles appear to be insulated from one another by naturally grown oxide layers. This presents a large effective surface area, and the microwave noise is adsorbed through skin-effect damping. In benchtop experiments, we measure these filters to attenuate ac signals by more than 40 dB from 100 MHz to 1 GHz, and more than 50 dB above 1 GHz.

The container we use is a cylinder one inch in diameter and about two inches high. The bottom cap has a screw mounted on it so that the whole assembly can be screwed onto the mixing chamber. Seven of the eight sample leads run through the filter. Lead #7 does not, as after the whole assembly had been mounted, we discovered that it shorted out to the dilution refrigerator body somewhere in the filter. In our experiments, we do not use #7. For each of the other leads, about two feet of wire is coiled up inside the container.

One drawback with our filter design is that at milliKelvin temperatures, if the intergrain thermal contact is poor, the copper grains may be inadequately heat sunk to the mixing chamber. This would limit the filter's effectiveness as it only adsorbs radiation down to its blackbody temperature. Martinis, *et al.* have attempted to solve this problem by mixing the copper grains with a low-temperature epoxy (Stycast 2850; Schall, Burlington, MA), using it as a matrix material. Though this increases the grain heat sinking, it also decreases the number of grains per unit volume, thus decreasing the effective surface area needed for microwave dissipation. To our knowledge, no systematic tests have been performed on these filters or their designs.

On employing a current-biased circuit, we use no other filtering. However, when using a voltage-biased set up we find the curves often to be sharply rounded. Using ERIE filters at the top of the fridge on both the current and voltage leads sharpens up the curves, though never as much as with the current biased circuit. We therefore stick to the current-biased

set-up as much as possible. Figure 3-11(a) shows the current bias set-up employed, including placement of the microwave filters, and Fig. 3-11(b) shows a voltage bias set-up.

Figure 3-12 shows a schematic diagram of a ramping current/voltage source designed by M. Tuominen. The source's basic features are controlled by four pots: the pot marked "f" is used to control the sweep rate; that marked "range" is used to control the maximum output of the source; that marked " R_L " is the limiting resistor ($R_L = 0$ gives a voltage bias while $R_L = 1 \text{ G}\Omega$ gives a current bias, for most applications); and that marked " R_m " is used as the measuring resistor across which the current is determined in current bias mode. When set to "hold", the source sits at a particular current or voltage. However, due to non-ideal op-amps, the current or voltage will drift. Therefore, this circuit is not appropriate for uses which require a fixed current or voltage.

3.3.2 Microwave Set-Up

For the experiments looking for SET oscillations, we wish to irradiate the samples with microwaves up to 20 GHz. Delsing, *et al.* (1989b) performed a similar experiment where they irradiated one dimensional arrays with microwaves. In a large part we duplicate their methods. We run the microwaves from the top of the cryostat to the sample using stainless steel coax. While somewhat lossy (the 0.081" diameter coax is rated at about 3 dB/foot at room temperature), the low thermal conductivity of the stainless steel prevents a large heat leak. We find it necessary to insert a fixed attenuator (Narda; Hauppauge, NY):¹ without it we find significant heating of the sample by either blackbody radiation getting down the coax or simple thermal conduction through the inner conductor, which is not directly heat sunk at any point. The fixed attenuator absorbs a significant fraction of the blackbody radiation, and appears to allow for a good heat-sinking path to the inner conductor. On the helium-3 refrigerator, we use one 20 dB attenuator thermally anchored to the He-4 pot. On

¹We use DC - 18 GHz fixed attenuators with SMA-type connectors. Though only rated to -55° C, we have used them at milli-Kelvin temperatures and have thermally cycled them over ten times without noticeable degradation of their performance.

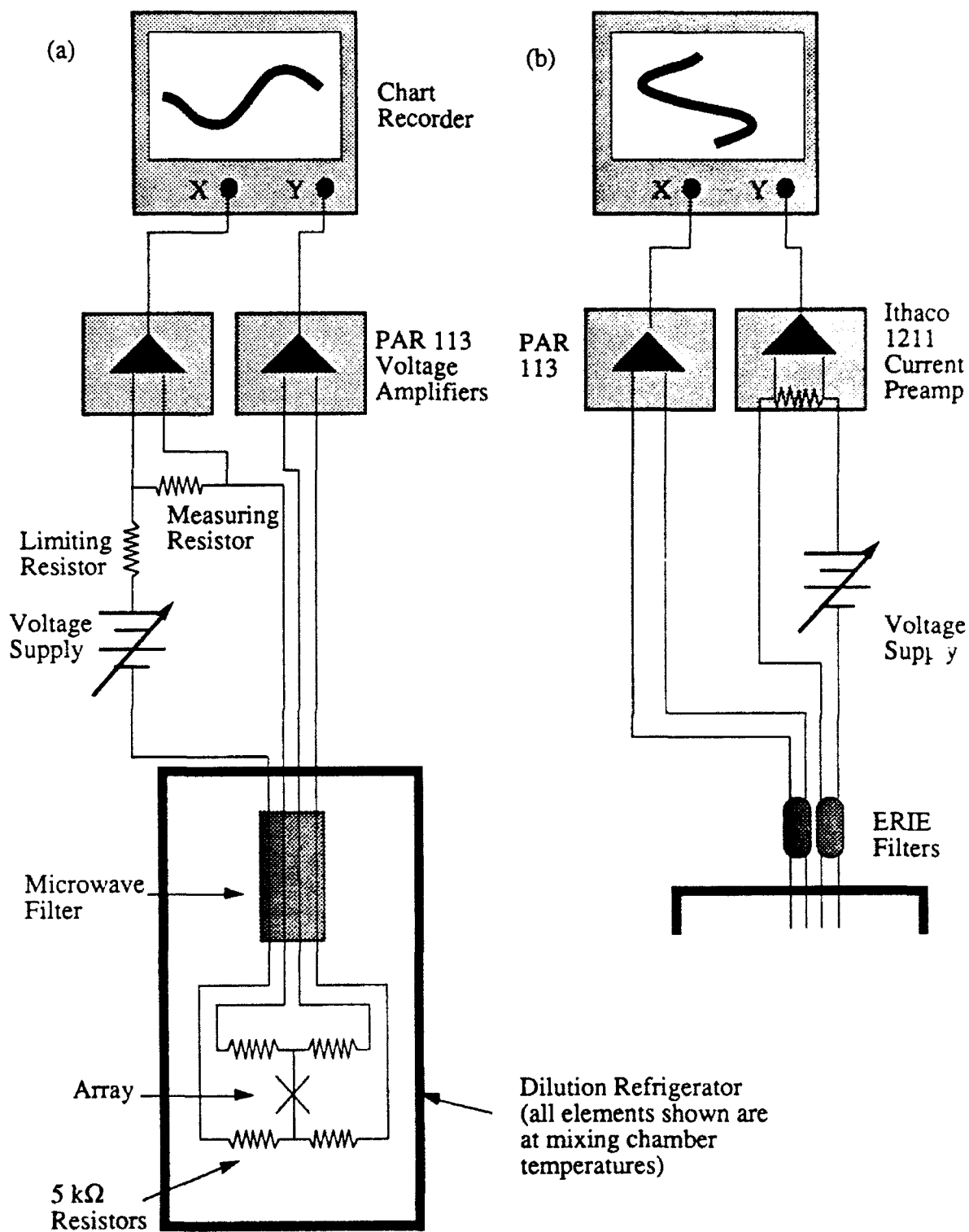


Figure 3-11.

The circuit used for (a) current biased and (b) voltage biased measurements.

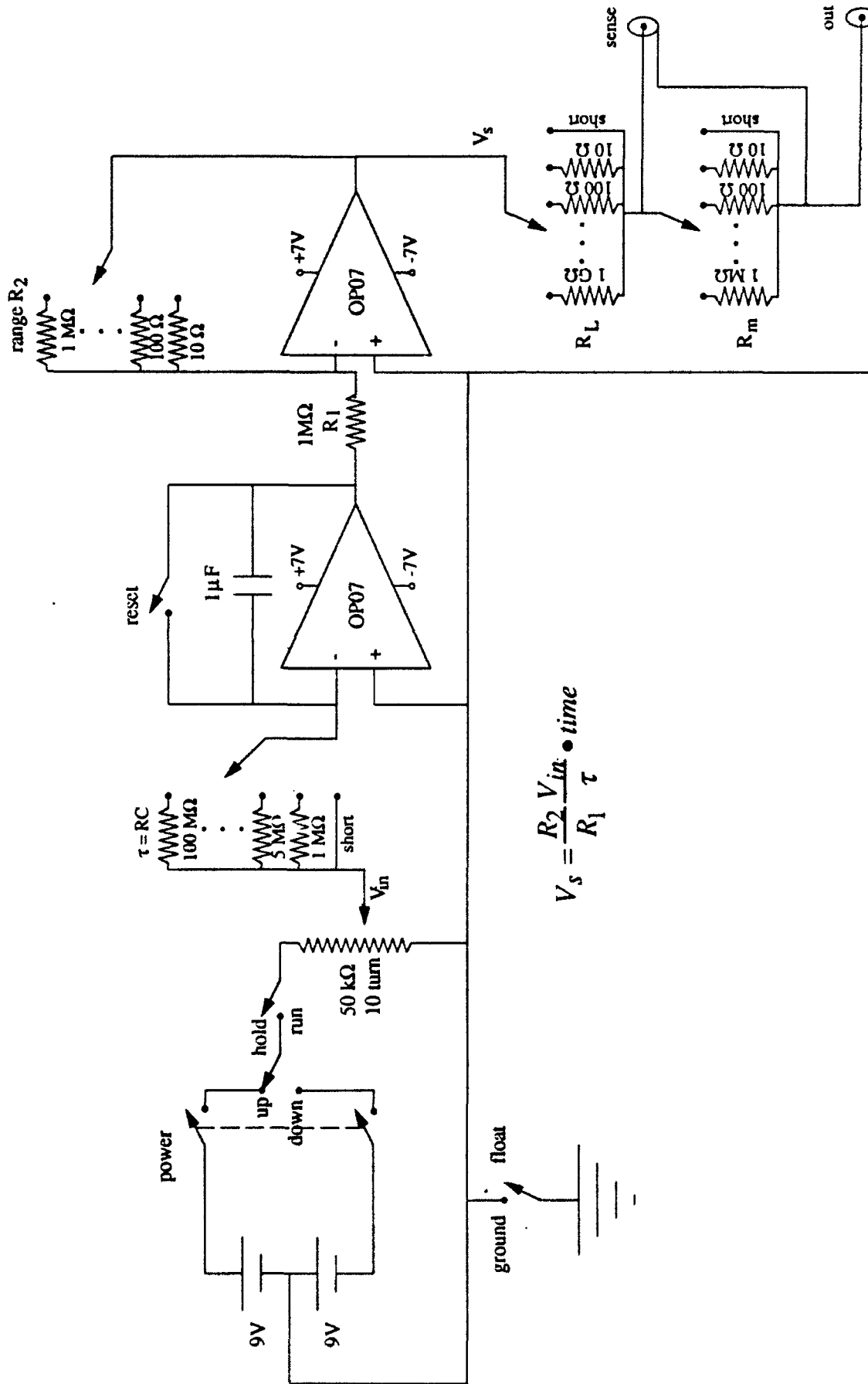


Figure 3-12.

Schematic drawing of ramping current/voltage source designed by M. Tuominen. The equation gives the sweep rate as a function of the circuit parameters. The current can be measured (in current bias mode) by measuring the voltage across the measuring resistor at the "sense" output. For a limiting resistance of 0, the circuit is in voltage bias mode, while for a large limiting resistance, the circuit acts as a current bias for most applications.

the dilution refrigerator, we use two attenuators; a 15 dB attenuator thermally anchored to the He-4 pot and another 10 dB one anchored to the mixing chamber. In addition, we thermally anchor the outer conductor to different stages to assist in heat-sinking.

We couple the microwaves to the sample by attaching them, through blocking capacitors, directly to the leads going across the sample. Delsing, *et al.* tried several different coupling schemes, including radiative coupling using a three turn coil, and report this one to work the best. The blocking capacitors are necessary as without them, the sample leads would short though a resistance of roughly $50\ \Omega$ in the fixed attenuator. We use 100 pF mica capacitors.

Using microwaves in the dilution refrigerator does not allow for top loading; the microwaves would dissipate getting through the wiring on the slug. Therefore, we mount the sample on the outside of the refrigerator tail-piece, as seen in Fig. 3-13. In this position, we can still apply a magnetic field of up to 7 Tesla, while injecting the microwaves in the same fashion as we do in the helium-3 refrigerator. One important feature is that we use the same DC leads as in the other, non-microwave experiments. We top load a slug packed with three inches of sample wire, pull the wire out through a slot in the tail, and connect it to the sample.

3.4 Refrigeration

We perform the majority of measurements in an Oxford Instruments Model 200 dilution refrigerator, with top-loading option. The dilution refrigerator has a base temperature of 13 mK and is equipped with a 7 Tesla magnet. The top-loading option limits the number of sample leads to 8. However, for experiments which do not use this option (for example, the microwave experiment described in the last section), more leads can easily be added (16 are presently available). A semi-rigid coaxial cable for carrying microwave signals also exists, as described in the last section. The refrigerator also has many other features, such

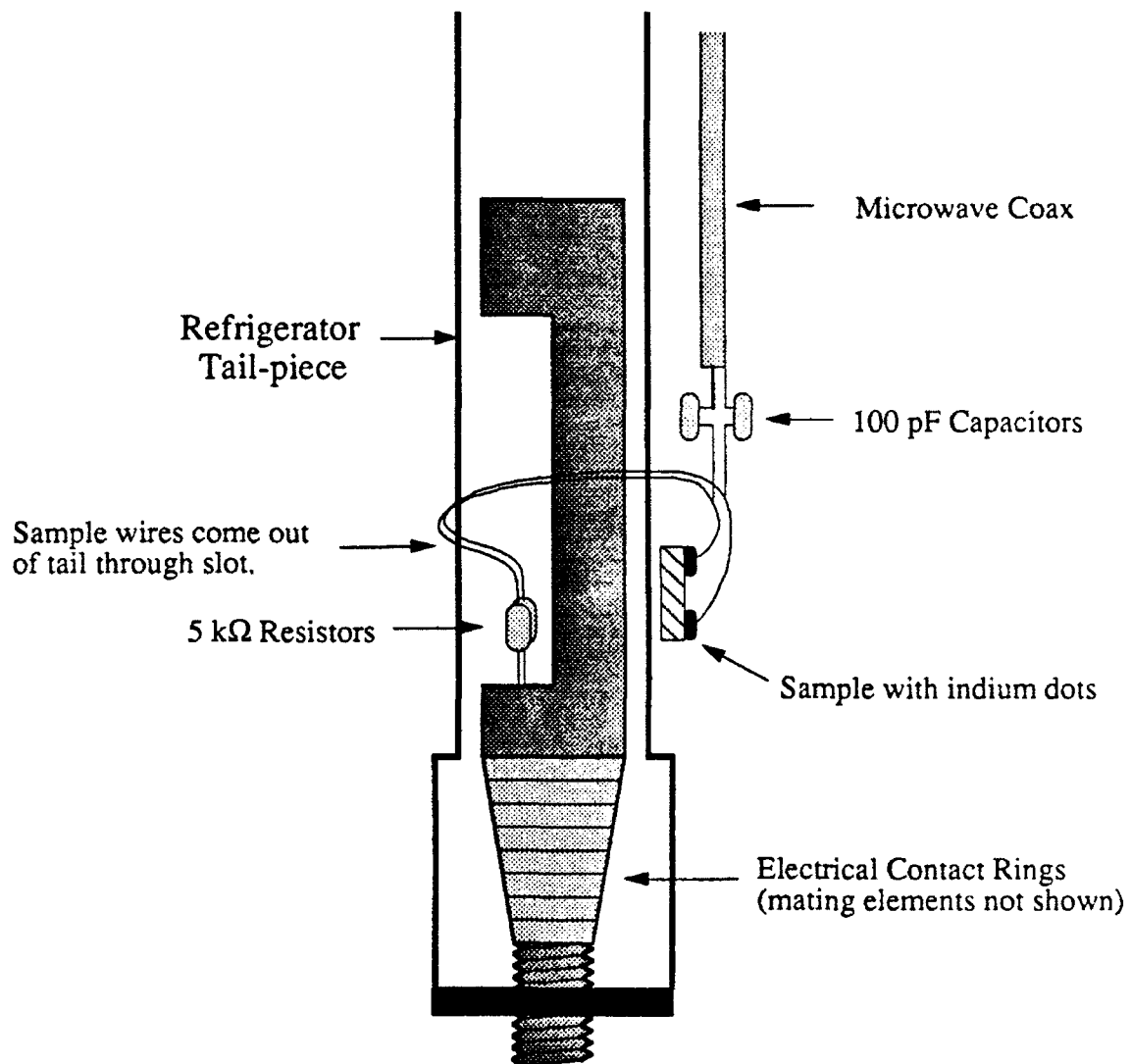


Figure 3-13.

This figure shows the mounting set-up for the microwave experiment in the dilution refrigerator. The sample sits outside the refrigerator tail, but is still connected to the slug leads through wires pulled out through a slot in the tail (we only show two leads here). The microwaves are fed into the sample by attaching its center and outer conductors to opposite sides of the sample. For a more detailed description of the slug, see Fig. 3-10.

as a rotary feed-through and gas feed-throughs, which are all currently unused.

We principally rely on two thermometers, both mounted on the mixing chamber, to determine temperature; a germanium-resistance-thermometer (GRT) and a ruthenium-oxide (RuOx) thick film thermometer. The GRT (Lake Shore Cryotronics, Westerville, OH) works well for temperatures of 300 mK to 6 K and is calibrated by the manufacturer. Though rated for temperatures down to 50 mK, its readings are not as accurate in this temperature range as the readings of the RuOx thermometer. The RuOx thermometer also has the advantage of having a small magneto-resistance, so that for a given temperature its readings do not change much with an applied magnetic field [Li, *et al.* (1986)]. However, the RuOx thermometer has to be calibrated for every cool-down. For this purpose we use five slugs of superconductors with calibrated transition temperatures (purchased from the National Bureau of Standards).¹ With each slug we coil wire around it to form an inductor, the inductance of which we measure by ac lock-in techniques. As the inductance depends on whether the slug is in the superconducting or normal state, we can use the lock-in signal to sit on the transition (specifically, we use the lock-in output as the "error" signal into the temperature controller). The known transition temperature of each slug allows us to calibrate the resistors.

We also use an RMC Cryosystems helium-3 refrigerator and several simple pumped liquid helium systems. The helium-3 refrigerator can reach 300 mK and is designed to fit into a magnet system (Cyromagnetics, Inc.) with a maximum field of 5 Tesla. Cooling comes from pumping on a bath of liquid helium-3 with an activated charcoal pump. Unlike the dilution refrigerator which can operate continuously, periodically the charcoal must be heated, driving off the helium-3 so that it can recondense in the bath. Typically, we have found the need to "regenerate" every 6-8 hours. For thermometry we use a calibrated GRT, similar to the one used in the dilution refrigerator.

We discuss sample self-heating, as it may prevent the sample temperature from reaching

¹The transition temperatures of the five slugs are roughly 15, 23, 101, 161, and 207 mK.

these low milli-Kelvin temperatures. Heat generated by the Josephson junctions may dissipate through two mechanisms: through the on-chip leads and through the substrate.¹ Iansiti (1988), and more extensively, Smith (1989) give calculations for heat dissipation both by conduction through the on-chip leads, and by the substrate. By simple arguments Iansiti showed that for his single junctions at 30 mK, the on-chip leads should be ten times as effective as the substrate for carrying away heat in the form of phonons (as the material is superconducting, electronic heat conduction is greatly reduced). For arrays, however, heat conduction through the on-chip leads is hampered by the presence of multiple junctions: the junction's insulating layer acts as a barrier to phonons as well as to electrons. Heat generated in the center of the array must pass through a minimum of 35 junctions before reaching the on-chip leads. In addition, with our array design we have a much larger area closer to the junctions than did Iansiti, *i.e.* the rectangles seen in Fig. 3-1(a). Therefore, heat-sinking through the substrate should be important, and we consider it here.

We quantify the discussion of self-heating by introducing $\Delta T = T_{\text{sample}} - T_{\text{refrigerator}}$. For a given input power P , we have

$$\Delta T = R_K P \quad (3.1)$$

where R_K is called the Kapitza resistance. The Kapitza resistance is given in Louanasmaa (1974) to be

$$R_K = \frac{\kappa}{AT^3} \quad (3.2)$$

where A is the interface area and κ is a constant and depends on the two materials.

Richardson and Smith (1988) give a typical value for κ from a metallic to a dielectric as 30

¹The substrate is heat sunk by the large contact pads, in turn heat sunk through the leads which coil around the slug (See Fig. 3-10). Following the arguments presented above, the large area of the contact pads presents a strong thermal link.

(K⁴ cm²/W).

For the tin arrays, we estimate the interface area *per junction*¹ to be 6.4 μm². At 50 mK, Eqn. (3.2) gives a Kapitza resistance of 3.8 x 10¹² K/W. To allow an increase in temperature of only ΔT = 2 mK, the maximum power input per junction P_{max} is 530 aW. Table 3-2 gives these values for the aluminum as well as tin arrays. These arguments suggest that we can measure the tin arrays with 2 pW input power (at 50 mK) before sample self-heating begins to affect the sample temperature. For the aluminum arrays, the corresponding power level per junction P_{max} is 0.15 pW.

Table 3-2 Estimated Kapitza resistance and power levels at 50 mK for a maximum temperature increase of 2 mK, for tin and aluminum 50 by 70 arrays.

Material	Area <i>per jj</i>	R_K (K/W)	$P_{max, per jj}$ (W)	$P_{max, array}$ (W)
Tin	6.4 μm	3.8 x 10 ¹²	5.3 x 10 ⁻¹⁶	1.9 x 10 ⁻¹²
Aluminum	0.5 μm	4.8 x 10 ¹³	4.2 x 10 ⁻¹⁷	1.5 x 10 ⁻¹³

We can compare these estimated values with that inferred from measurements. For the tin array sample #14, we measure the low voltage resistance R_0 to have a strong temperature dependence down to 50 mK,² a good indication that sample heating is not a serious limitation in reaching low temperatures. This test is limited, however, to the region where the current-voltage (I-V) curves are continuous, roughly at powers below 100 fW total power. This value of 100 fW falls below the predicted limit of $P_{max, array} = 2$ pW. The measurements of R_0 , whose interpretation would be clouded if the sample's temperature was significantly above that of the mixing chamber, are all made below powers of 100 fW.

For the aluminum arrays, with sample #17 we measure temperature dependent

¹The *per junction* area includes the rectangular islands (see Fig. 3-1). As a 50 by 70 array holds 3500 islands and 7000 junctions, on average each junction dissipates heat through half an island.

²We see this temperature dependence when the sample is in a magnetic field of about 50 G.

conductances down to 50 mK. This test is limited to a total power below 0.4 fW, below the estimated limit of $P_{max, array} = 0.15$ pW. Again, all conductance measurements, whose interpretation would be clouded by sample self-heating, are made below this power level.

In the microwave experiment, we see evidence of heating at the larger power levels used. We can estimate the heating by using the sample itself as a thermometer. Previous measurements record the temperature dependence of the sample's conductance around zero bias--with applied microwaves, we can measure that conductance to infer the temperature. While not completely accurate, as the microwaves may influence the conductance other than through simple heating, it should give a rough idea of the actual sample temperature. We will use this technique in discussing the data presented in Chapter 7.

CHAPTER FOUR

MEASUREMENTS AND DISCUSSION ON SUPERCONDUCTING ARRAYS

This chapter discusses the measurements and results on arrays on the superconducting side of the superconductor-to-insulator transition. Section 4.1 deals with the basic characteristics of the measurements: I-V curves showing depinning, critical and retrapping currents, the low-voltage resistance R_0 , and the magnetic field response. In section 4.2 we discuss the interpretation of some results of the measurements. First, we compare aspects of the measurements (depinning current and temperature dependence of R_0) with the theoretical predictions. We then explain some results on vortex viscosity and critical velocity using a model of vortex damping developed by Nakajima and Sawada (1981), Bobbert (1992), and Geigenmüller, *et al.* (1993).

4.1 Basic Array Characteristics

Before discussing the array parameters, it is important to define the notation used. From our measurements, it appears that the arrays discussed in this chapter are inhomogeneous: there exists a spread in the values of the normal resistance R_n and the capacitance C of the junctions within an array. To clarify the discussion, we introduce the notation that \bar{R}_n refers to the *average* resistance of junctions within a non-uniform array, while R_n represents the resistance of junctions within a *uniform* array (used when discussing an array in theoretical or general terms).¹ We also at times make the

¹This notation also applies to all the parameters discussed: C , E_J , E_c and I_c , but is specific to this chapter only.

approximation that each row acts independently, *i.e.*, each has its own critical current and vortex energy barrier. To denote this, we use the subscript m to refer to the m^{th} row ($1 \leq m \leq M$, where M is the total number of rows). The row number is defined by the order in which the row switches from the zero-voltage state to the gap-voltage state [see Fig. 4-1 and the discussion following]. Hence, the critical current of the first row to switch is I_{c1} , the m^{th} row I_{cm} , and the last row I_{cM} . Finally, parameters denoted with primes, such as ρ_{co}' , are used in special cases where we specifically attempt to correct for the inhomogeneities within an array.

The samples are largely defined by several factors: the array size, the junction normal resistance and the junction capacitance. The size of the arrays is given as M rows by N columns, with the current direction along M (the current must travel through M junctions). We determine \bar{R}_n by measuring $\Delta V/\Delta I$ at temperatures above the superconducting transition temperature T_c , or at voltages far above the superconducting gap, and scale it by the N/M geometric factor. To determine \bar{C} for the tin arrays discussed in this chapter, we measure the junction area using a scanning electron microscope, then convert it to a capacitance using the factor $25 \text{ fF}/\mu\text{m}^2$, as given by Iansiti (1988) and Danchi (1982).^{1,2} Table 4-1 gives the values of \bar{R}_n and \bar{C} for the arrays, as well as \bar{E}_J , \bar{E}_c , the junction plasma frequency $\bar{\omega}_p$, the array size, and the average junction area.

The following three sections discuss the general features of the data. In Sec. 4.1.1 we look at characteristic I-V curves. In Sec. 4.1.2 we show the magnetic field response of the arrays, and in Sec. 4.1.3 we briefly discuss inhomogeneity within the array.

¹This method is not as accurate as determining \bar{C} from the offset voltage--the method used for the aluminum arrays and discussed in Chapter 6. However, for the results discussed here, the capacitance only enters our calculations as the square root of C in the plasma frequency ω_p and the quality factor Q , and any inaccuracies do not significantly affect the interpretation of the data.

²Recent work on aluminum junctions give a value of $45 \text{ fF}/\mu\text{m}^2$ or greater for aluminum. It is surprising that the specific capacitances for tin and aluminum would differ by nearly a factor of two. This suggests that the value of $25 \text{ fF}/\mu\text{m}^2$ for tin may be too small. We will continue to use it, however, as we have no firm basis for any other value.

Table 4-1. Parameters for tin arrays. "D" under array size refers to the diamond pattern discussed in Chapter 3 and Appendix A. The uncertainty in area for sample #5 is twice as large as that for the other samples due to less accurate micrographs of the junctions.

Sample #	Array Size $N \times M$	junction area (μm^2)	\bar{R}_n ($\text{k}\Omega$)	\bar{C} (fF)	$\bar{\omega}_p$ rad/sec	\bar{E}_J/k_B (K)	\bar{E}_c/k_B (K)	\bar{E}_J/\bar{E}_c
1	50 x 70	0.07 ± 0.01	1.2	1.8 ± 0.6	1.1×10^{12}	18	0.5	40
2	50 x 70	0.07 ± 0.01	5.0	1.8 ± 0.6	5.4×10^{11}	4.3	0.5	9
3	10 x 10 D	0.15 ± 0.01	29	3.8 ± 0.6	1.4×10^{11}	0.75	0.2	4
4	50 x 70	0.10 ± 0.01	24	2.5 ± 0.6	2.2×10^{11}	0.90	0.4	2
5	10 x 10 D	0.15 ± 0.02	39	3.8 ± 1.2	1.2×10^{11}	0.56	0.2	3

4.1.1 I V Curves

Figure 4-1 shows an I-V curve for sample #4 (a 50 by 70 array) at a temperature of 90 mK. The curve is hysteretic: increasing the current from zero, no voltage (on this scale) appears across the array until the critical current *of the first step* I_{c1} is reached. The voltage then jumps in many steps to roughly 70 times the gap voltage. These steps result from individual or multiple rows switching from a zero-voltage state to a gap-voltage state, as has been reported by van der Zant, *et al.* (1988). The wide distribution of currents where the steps occur is attributed to junction inhomogeneity.

Upon decreasing the current from this state, the voltage does not drop down immediately, but remains fairly constant until very near zero current. Then, at the retrapping current I_{r1} (on the order of 10 pA), the voltage drops back down to zero. This drop also occurs in discrete jumps, but only the last few are discernible, and then only on an expanded current scale. All of the samples show similar behavior.

Figure 4-2 shows three I-V curves for sample #5 at different temperatures. In (a), at a temperature of 2.6 K, the curve is rounded due to the strong thermal fluctuations which cause continuous phase slips. This figure also shows our definition of the critical current in this temperature region [the same definition as used by Iansiti (1988)]. As this value is

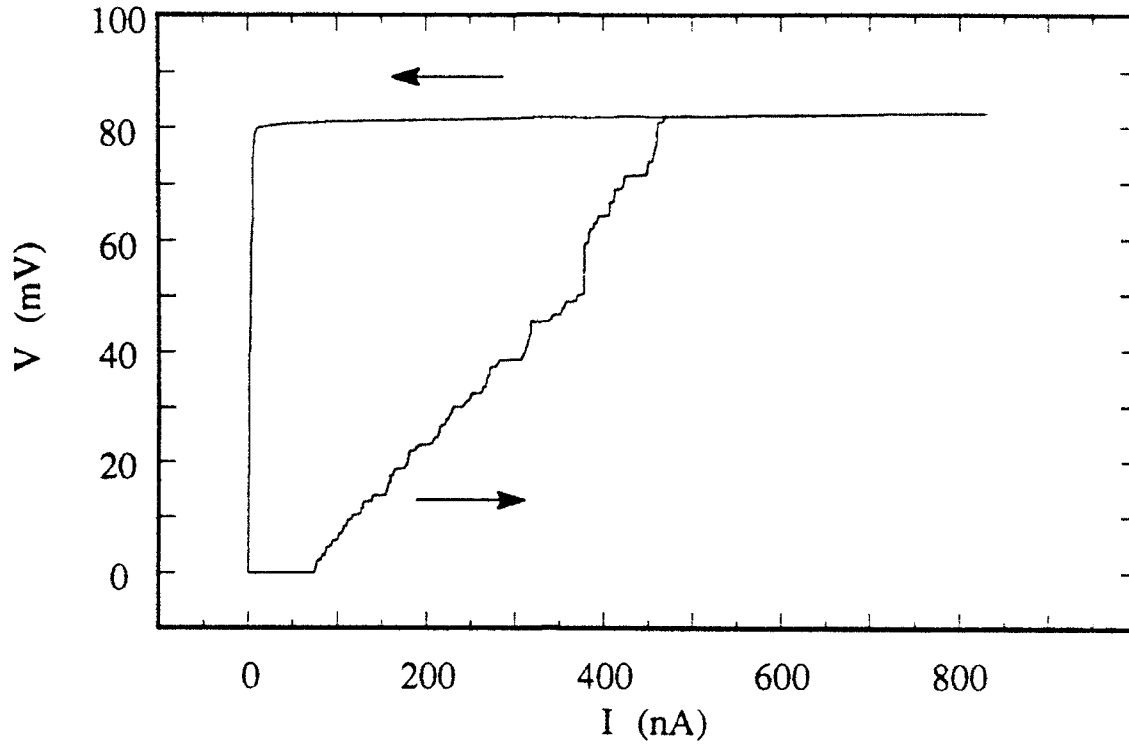


Figure 4-1.

Current-voltage characteristics for sample #4 at 90 mK. The curve is hysteretic, with the arrows indicating the direction of the sweeping current. The frustration for this curve was not recorded, and for different frustrations the I-V curves do not qualitatively change. However, the current values where the switches occur do shift.

most likely an average over all the junctions, we denote it by \bar{I}_c . Figure 4-2(b) shows the I-V curve at a temperature of 1.8 K, the point at which hysteresis first appears (not visible on this scale). The sharp nature of the curve makes the definition of the critical current unambiguous. In curve (c), at a temperature of 1.2 K, the curves are hysteretic, and resemble Fig. 4-1 in form (the point at which the two branches rejoin is not visible on this scale). In this case, we discuss I_{c1} , the critical current of the weakest row. Although it might be more useful to take an average over all of the rows, we were not aware of the importance of this and did not take enough data in order to be able to determine \bar{I}_c accurately over this temperature range.

Figure 4-3 shows \bar{I}_c and I_{c1} (per junction) as a function of temperature for samples #3

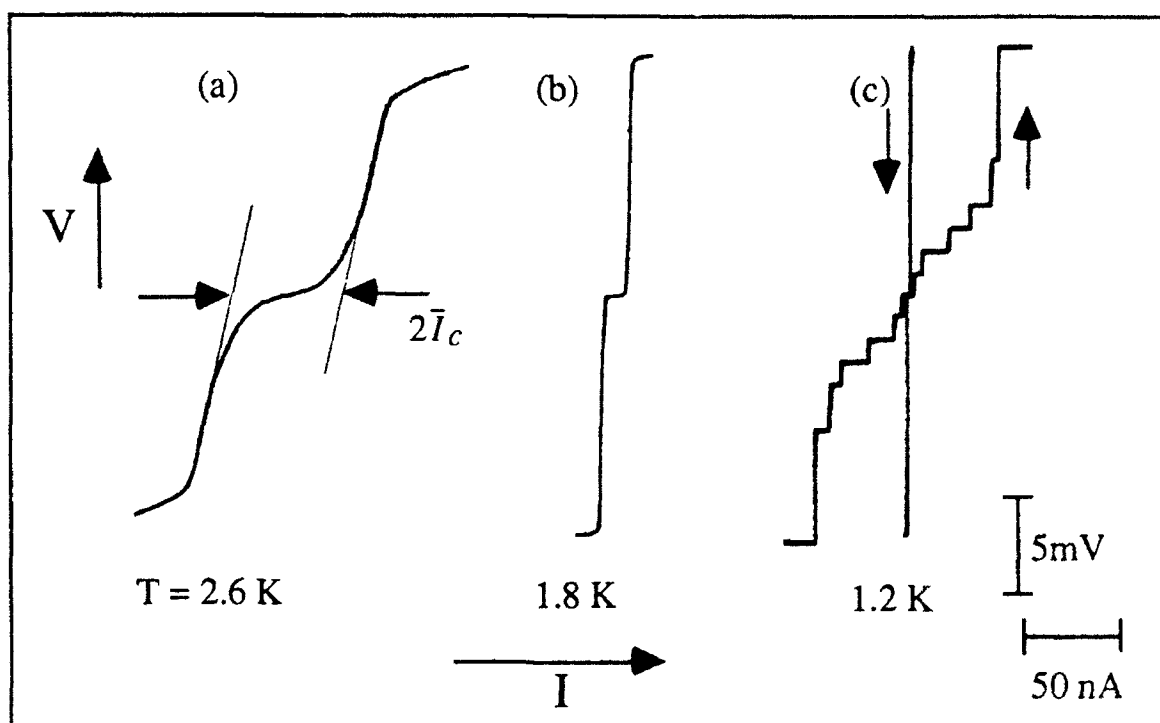


Figure 4-2.

Series of I-V curves at different temperatures for sample #5 (integral value of f). In curve (a), taken at a temperature of 2.6 K, the curve is rounded. We define the "critical" current as seen in the figure. Curve (b) is taken at a temperature of 1.8 K. For temperatures above this, the curves are non-hysteretic, while for temperatures below this, hysteresis occurs. Here, the I-V curve is sharp enough to make a unique determination of I_c . In curve (c), taken at a temperature of 1.2 K, we measure hysteretic curves (the arrows show the direction of the sweeps--the two branches do not rejoin at the scale of this curve). We typically define the critical current in this case as I_{c1} , the current at which the first row switches. The current and voltage scales to the right of (c) apply to all three curves.

and #5, as well as a comparable single junction measured by Iansiti (1988). The average normal resistances of the two arrays are 29 and 39 k Ω respectively, which bracket the resistance of the single junction, 34 k Ω . At temperatures above the point where hysteresis sets in (≈ 1.8 K) the three curves track together, as one might expect if our method of determining critical currents in this temperature range [Fig. 4-2(a)] does indeed give the *average* value. For temperatures below this point, the single junction I_c increases at a faster rate than that of the arrays, and might reflect that I_{c1} measures the critical current of the weakest row, which is, of course, less than \bar{I}_c .

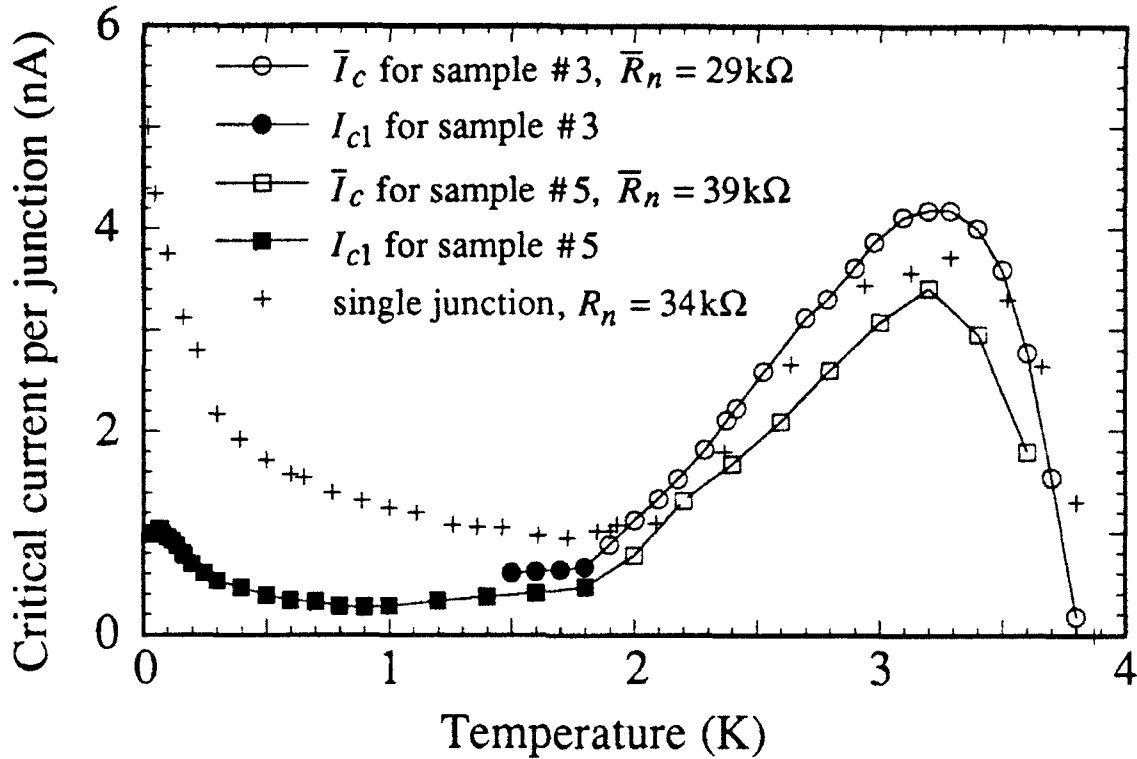


Figure 4-3.

\bar{I}_c and I_{c1} per junction vs. temperature for samples #3 and #5 and a single junction measured by Iansiti (1988). The normal resistance of the single junction falls between that of the two arrays. Due to our method of determining critical currents for the arrays, above the point of hysteresis (≈ 1.8 K) we measure \bar{I}_c while below it we measure I_{c1} . The curves for the arrays are taken at $f \approx 0$.

Iansiti (1988) gives an excellent and lengthy discussion of the shape of the curves in Fig. 4-3, which we attempt only to summarize here for the case of a single junction. In general, thermal fluctuations decrease I_c , as they allow for the system to be prematurely activated out of its metastable well in the washboard potential (see Sec. 2.i.4). Less well known is that thermal fluctuations *increase* I_r : ramping down the current with the system in the running or voltage state, fluctuations prematurely “knock” the system back into a metastable well. As we increase the temperature from zero, I_c largely decreases (as seen in Fig. 4-3) and I_r increases (not shown) until they converge, $I_c = I_r$, the point at which

hysteresis disappears.¹ Iansiti argues that for temperatures above that where hysteresis disappears (≈ 1.8 K), thermal fluctuations are so prominent that the system is prematurely activated out of the metastable state continuously. Thus, the observed "critical current" in this temperature range is in fact determined by the condition for the retrapping current $I_r(T) \propto I_c(T)/\sqrt{\beta_c}$. As Iansiti discusses, $I_r(T)$ at first increases with increasing T because of the exponential increase in damping $1/\sqrt{\beta_c}$. Close to T_c , however, the reverse is true since $1/\sqrt{\beta_c}$ becomes constant while $I_c(T)$ drops toward zero; hence, the rise and fall in Fig. 4-3 for temperatures above $T \approx 1.8$ K.

Using higher voltage sensitivity to study the region before the first step, where all the rows are nominally in the zero-voltage state, we see a small voltage. This voltage is evidence for vortex motion, as the measured voltage for a single vortex is proportional to the average vortex velocity v ,

$$v = \frac{Na}{\Phi_0} V \quad (4.1)$$

where N is the number of columns through which the vortex moves in crossing the array ($N=50$), and a is the lattice spacing. Figure 4-4 shows these features, with the vertical scale of Fig. 4-1 expanded by a factor of 1000. The I-V curves are dependent on the frustration f : the sample develops little voltage for $f \approx 0$, where few vortices are present, but the voltage develops much more rapidly for higher f , where there are more vortices.

For all the values of frustration, no voltage develops until a certain value of current is exceeded, which we identify as the depinning current for the weakest row I_{d1} . In general, the depinning current is a measure of the pinning barrier E_b : the vortices are pinned until forced over the barrier by a sufficiently strong bias current [in the absence of thermal activation, which we believe is negligible at 50 mK (see Sec. 3-4)]. For currents stronger

¹Iansiti (1988) also includes Zener tunneling in discussing the low-temperature behavior of I_c , which we will not go into here.

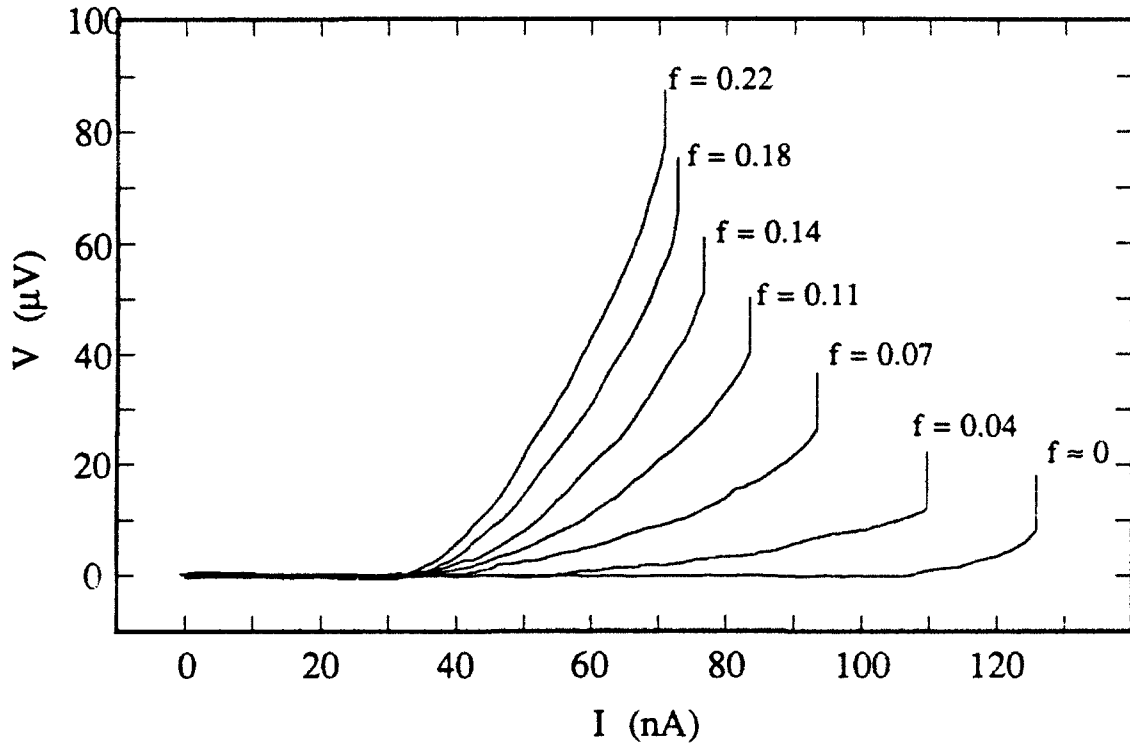


Figure 4-4.

Current-voltage characteristics for sample #4 at 50 mK, before the first step. The vertical scale has been expanded by roughly a factor of 1000 over Fig. 4-1. The different curves are for different values of frustration f , from $f \approx 0$ to $f = 0.22$.

than I_d , the system is in a flux flow regime, with damping largely determining the vortex motion. We will discuss this damping mechanism in Sec. 4.2.3.

For currents less than I_d , a vortex can still move from well to well by thermal activation. Making the direct analogy between single junctions and vortices in an array (shown in Sec. 2.2), we follow the work of Ivanchenko, *et al.* (1968) and Iansiti, *et al.* (1989b) to show that this thermal activation is marked by a linear I-V curve around zero bias. This allows us to define a low-voltage resistance R_o . In Fig. 4-5 we see an I-V curve at 0.7 K which shows the linear slope \bar{R}_o (as with the normal state resistance, what we measure is in some sense the average value for the array).

For single junctions, the presence of *both* a measured voltage for $I < I_c$ and hysteresis is

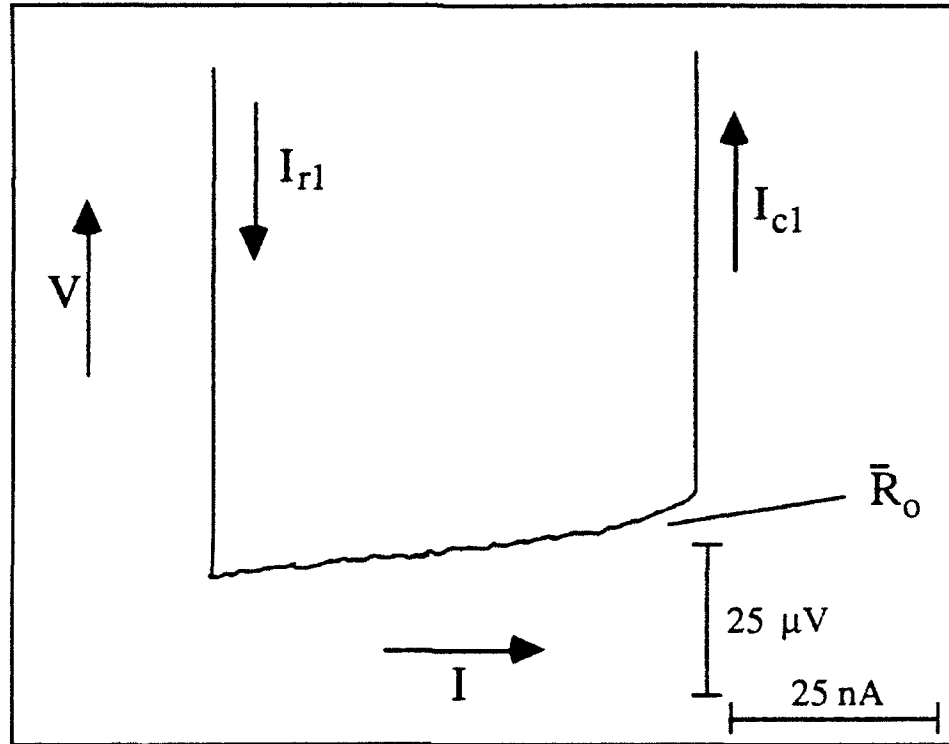


Figure 4-5.

I-V characteristics at an expanded scale for sample #4 at a temperature of $T = 0.7$ K and a frustration of $f \approx 0$. This figure shows the definition of the zero-bias resistance \bar{R}_0 , as well as the critical and retrapping currents of the first row.

not explained by the RCSJ model. Ideally for $I < I_c$, the system remains trapped in a potential well with $V = 0$. At I_c , it escapes and runs free, leading to a measured voltage of the superconducting gap. That Iansiti (1988) measures both a voltage and hysteresis implies that for $I < I_c$ the system escapes its well, but is somehow damped back into the next well (or a subsequent one) of the washboard potential. Johnson, *et al.* (1990) explains this damping mechanism in terms of radiative losses down the leads. For arrays, however, junctions are isolated from the leads by other, high impedance junctions, so these radiative losses are thought to be suppressed. Vortices have a damping mechanism, though, with no analog in single junctions. This mechanism, described in Sec. 4.2.3, provides the same role as radiative losses in explaining why we measure both hysteresis

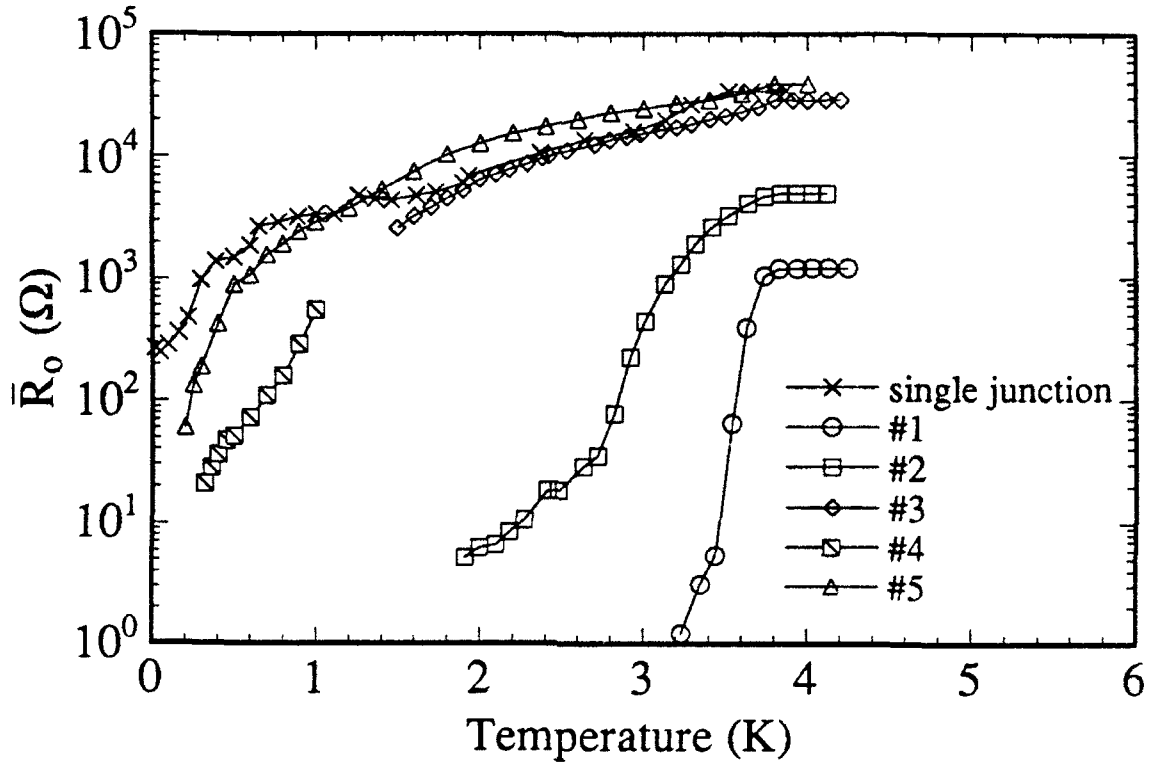


Figure 4-6.

The low-voltage resistance \bar{R}_0 vs. temperature for samples #1 through #5 ($f \approx 0$) and the single junction measured by Iansiti (1988).

and a voltage for $I < I_c$.

Figure 4-6 shows the temperature dependence of \bar{R}_0 for samples #1 through #5 as well as that for the single junction measured by Iansiti (1988). \bar{R}_0 falls off from the normal resistance as we lower the temperature below T_c , as there become fewer thermally-activated phase slips which lead to resistance. For the single junction, R_0 falls in a similar fashion, though not quite as quickly as arrays with comparable junction normal resistances, samples #3 and #5. We will discuss the temperature dependence of \bar{R}_0 in detail in Sec. 4.2.2.

4.1.2 Magnetic Field Response

As we increase the magnetic field perpendicular to the array, the vortex density increases until the independent vortex approximation breaks down. Vortices, repulsed from one

another, will move to form a pattern which minimizes this repulsive energy. At certain values of the frustration, this pattern becomes commensurate with the array lattice: the checkerboard pattern in Fig. 2-5(a) is an example. Commensurate lattices theoretically may form, for an infinite array, for any value of $f = p/q$ where p and q are integers. At the frustration $f = 1$, a vortex occupies every unit cell. Except at the edges, all the currents cancel and we recover the $f = 0$ state. Therefore, features in the I-V curves which are dependent on the frustration will largely be periodic in f with period 1.

Figure 4-7 shows the change in \bar{R}_0 with frustration for sample #4 at four temperatures. In all four curves we clearly see the periodic nature of $\Delta \bar{R}_0$ with the frustration. In (a), at a temperature of 1 K, we only see minima at integer values of f . In (c), at 200 mK, we see minima at integer and half integer values of f , as well as at $f = \pm 1/3$ and $\pm 2/3$.¹ In (d), at 90 mK, we see a complicated structure with many minima. This may be because at these low temperatures, the vortices are sensitive to junction inhomogeneities, which make the "egg-crate" potential more complicated than that described in Chapter 2. In this case, vortices may lock into odd configurations at these low temperatures.

Figure 4-8 shows the magnetic field dependence of I_{c1} . Here we see that I_{c1} is the largest for $f = 0$, with other peaks at $f = \pm 1$, and small peaks at $f = \pm 1/2$. Though taken at 50 mK, the magnetic field dependence of I_{c1} does not show nearly as much sensitivity as does \bar{R}_0 , which as we see in Fig. 4-7(d) at 90 mK has a complicated structure. This may be because the I_{c1} measurements are made at higher currents than the \bar{R}_0 measurements. The larger forces on the vortices due to these higher currents may disrupt all but the most robust vortex lattices.

¹ Minima in \bar{R}_0 occur because in a commensurate state, for voltage to develop, the entire vortex lattice must move. This requires more energy than for a single vortex to move, and hence the lattice is more strongly pinned, leading to a minimum in the voltage for a given bias current and hence the resistance.

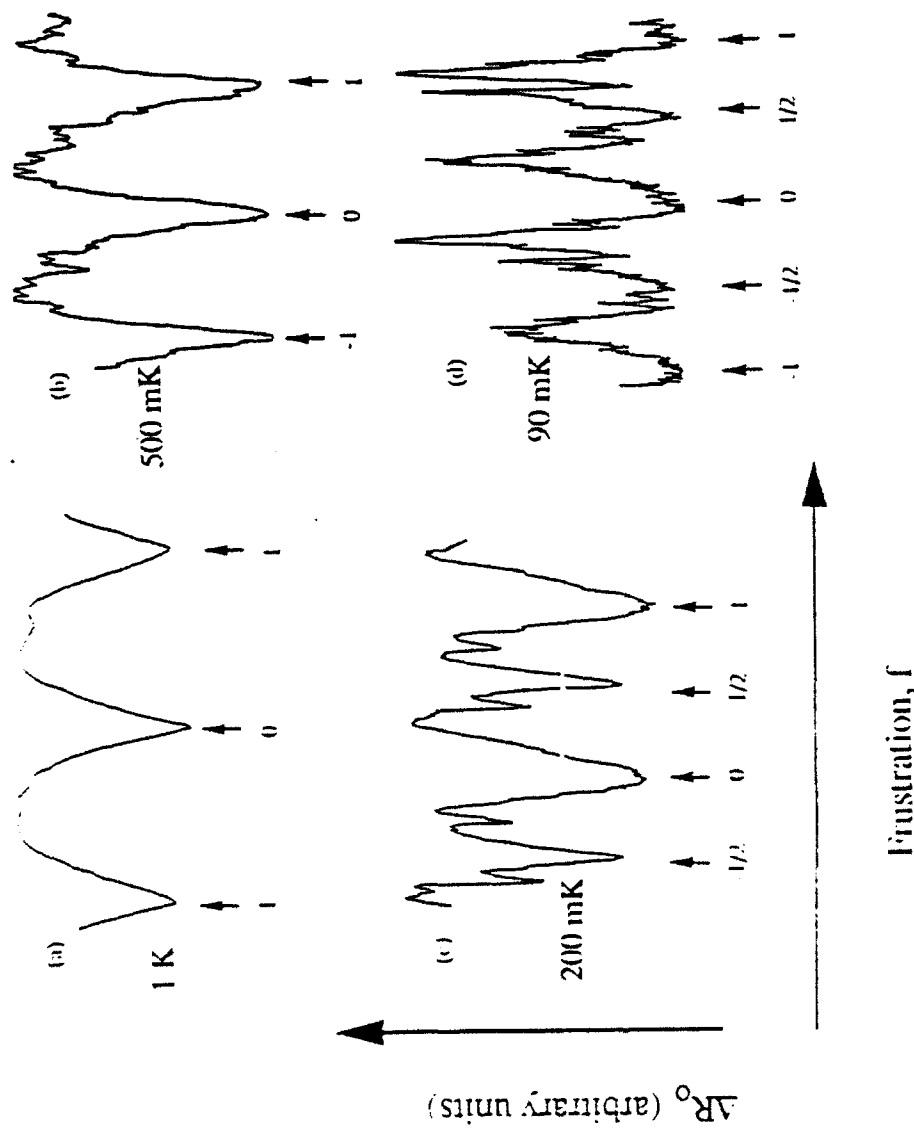


Figure 4.7.

This figure shows changes in \bar{R}_0 (as measured with a lock-in amplifier) vs. frustration for sample #4 at four different temperatures. Arrows mark the integer and half-integer values of f and \bar{R}_0 is a minimum. We do not know the absolute frustration for (b), so for that curve f is given only to within an added integer. We are unsure as to why the curves (c) and (d) have some asymmetry in the array normal direction (see Fig. 3-9). [Because of the overlap technique of fabricating junctions, however, the array does have some asymmetry in the array normal direction (see Fig. 3-9). This asymmetry occurs at length scales of $\sim 1000 \text{ \AA}$, roughly a factor of ten less than the unit cell length scales, and therefore the asymmetry should only become important on magnetic field scales of $f \sim 10 - 100$.]

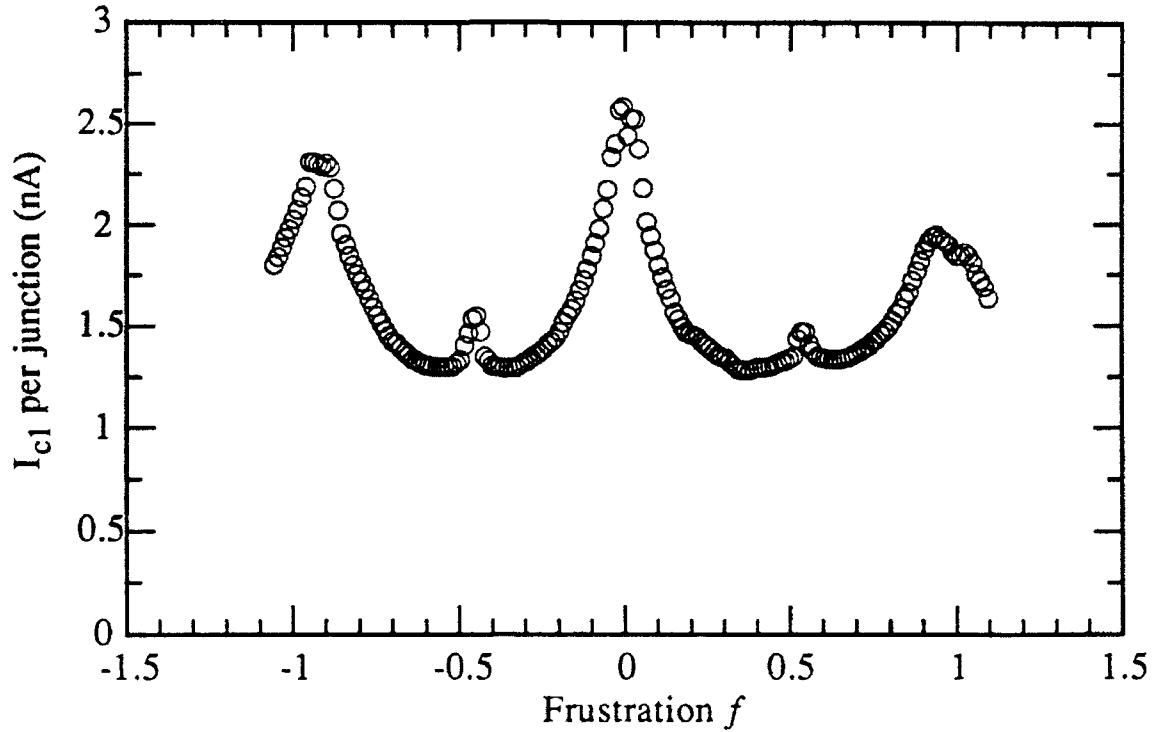


Figure 4-8.

Critical current I_{c1} per junction vs. frustration for sample #4 at 50 mK.

4.1.3 Junction Inhomogeneity

For tunnel junctions, the normal resistance is predicted to be [Knorr and Leslie (1973)]

$$R_n = \frac{\kappa}{A} \exp(t/t_o) \quad (4.2)$$

where A and t are the junction area and insulator thickness, and κ and t_o are constants. For aluminum junctions, Knorr and Leslie (1973) experimentally measure by ellipsometry κ and t_o to be $1.5 \times 10^{-3} \Omega \mu\text{m}^2$ and 1.0 \AA respectively.¹ For tin junctions, Iansiti (1988) gives a rough estimation of $t_o \sim 1 \text{ \AA}$, but does not give a value for κ .

¹Ellipsometry is based on the general principle that linearly polarized light reflected from a surface will become elliptically polarized. The oxide thickness can be determined from the form of the elliptical polarization.

Junction inhomogeneities may come from many sources, of which two significant ones are differences from junction to junction in A and t . Table 4-1 gives the largest uncertainties in A to be about 14%.¹ This does account for some of the inhomogeneity, but the larger source may come from differences in t . For tin junctions, we estimate t to be on the order of 20 Å. A change in t of one angstrom, or 5%, leads to a change in R_n by a factor of 2.7.

We have experimental evidence for this inhomogeneity and its magnitude. Tests on a 1D array of 10 junctions, fabricated in the same way as a 2D array, show a variation of I_{c1} of about 40%, and a standard deviation of 15% about the mean. We also have the distribution of steps for sample #4, seen in Fig. 4-1. We will use this distribution in discussing some results from our measurements on this array as a first attempt at explicitly accounting for the junction inhomogeneities.

4.2 Results of Measurements

We have divided this section into five subsections. In the first, Sec. 4.2.1, we discuss the critical and depinning currents for the array. In Sec. 4.2.2, we look at the pinning barrier to vortex motion as inferred from the \bar{R}_o measurements. Secs. 4.2.3 and 4.2.4 deal with theoretical and experimental results on vortex viscosity, and Sec. 4.2.5 discusses the vortex critical velocity.

4.2.1 Critical and Depinning Currents

As discussed above, at $T = 0$ vortices remain pinned for currents below the depinning current I_d . For $I > I_d$, the $j \times B$ force causes the vortices to move across the array, perpendicular to the current direction. We can compare our measured I_{d1} , the depinning current of the weakest row, to that theoretically predicted.

¹We measure this uncertainty by measuring different junction areas within an array. Therefore, the values quoted represent a spread in areas more than an uncertainty.

In general, Lobb, *et al.* (1983), give I_d as

$$I_d \cong 0.199Ni_{co} / 2 \quad (4.3)$$

where i_{co} is the theoretical *unfluctuated* critical current for a single junction, and N is the number of columns in the array ($N = 50$ for sample #4). We estimate i_{co} by the result, $i_{co}R_n \cong \pi\Delta/2e$ ($\approx 9.1 \times 10^{-4}$ volts for Sn). However, as we only measure the *average* value of the normal resistance, \bar{R}_n , we must replace i_{co} and I_d by their average values, \bar{i}_{co} and \bar{I}_d . For sample #4, Eqn. (4.3) yields $\bar{I}_d \cong 0.199N\bar{i}_{co} / 2 = 190$ nA.

However, the depinning current we measure from Fig. 4-4 will not be \bar{I}_d , but I_{d1} , the depinning current for the weakest row. We can estimate the *theoretical* depinning current of the first row I_{d1}' by multiplying the theoretical \bar{I}_d by the *measured* ratio of I_{c1} to \bar{I}_c [allowed because, from Eqn. (4.3), I_d is proportional to I_c]. From Fig. 4-1, this ratio is 0.24, which gives $I_{d1}' = 46$ nA.

Experimentally, at low values of frustration, the depinning current we measure is somewhat dependent on f , which makes it difficult to compare with that calculated above. As Fig. 4-4 shows, for $f = 0.04$, $I_{d1} \approx 55$ nA, while for f greater than roughly $f \approx 0.14$, I_{d1} approaches a value of $I_{d1} \approx 32$ nA. Within the approximate method we use to take account of inhomogeneities, these values are consistent with the estimated value of $I_{d1}' = 46$ nA.

4.2.2 Thermal Activation Measurements of E_b

Lobb, *et al.* (1983), derived Eqn. (4.3), $I_d \cong 0.199Ni_{co}/2$, from numerical simulations determining the vortex pinning barrier E_b

$$E_b \cong 0.199E_J \quad (4.4)$$

It is possible to determine E_b from thermal activation measurements. For single junctions,

Ivanchenko, *et al.* (1968) predict R_o to have the form

$$R_o \approx \frac{h}{4e^2} \frac{\hbar \omega_p}{k_B T} \exp\left(\frac{-2E_J}{k_B T}\right) \quad (4.5)$$

where $\omega_p = (1/\hbar)\sqrt{8E_J E_c}$ is the junction plasma frequency. Extending the simple arguments of Rzchowski, *et al.* (1990), outlined in Chapter 2, Eqn. (4.5) should be valid for vortices, but with E_J replaced by $0.199 E_J$ in the equations for both R_o and ω_p .¹ This does not take into account vortices jumping multiple wells, which was shown to be important in the prefactor of Eqn. (4.5) by Martinis and Kautz (1989) for single junctions. However, because we are mostly interested in the energy barrier E_b , given approximately by the slope of $\ln(R_o T)$ vs. $1/T$, we will not take multiple jumps into account.

Figure 4-9 shows $\bar{R}_o T$ vs. $1/T$ for sample #4 at $f \approx 0$ and $f = 0.16$. The general trend is for \bar{R}_o to increase as the temperature increases, which reflects the increasing thermal activation of vortices. The values for \bar{R}_o at $f \approx 0$ are much less than those for $f = 0.16$ simply because of the far smaller number of vortices present. We cannot measure \bar{R}_o for the lower temperatures because it falls below our noise level, about 1Ω .

From the slope of these curves, we determine the energy barrier for the $f = 0.16$ case for sample #4. We must be specific, however, in what we mean by the *measured* energy barrier. Because of inhomogeneities, different rows will have different barrier heights. Vortices will most easily move in the row(s) with the weakest barrier(s). Thus, it appears reasonable that the measured energy barrier will be the barrier of the weakest row(s), E_{b1} . The slope of the curve in Fig. 4-9 gives $E_{b1} \approx 1.0 \bar{E}_J (= 0.9 K \cdot k_B)$, higher than that predicted by Lobb, *et al.* (1983), $E_b \equiv 0.199 E_J$. If instead of \bar{E}_J we use an estimate of E_{J1} (found by multiplying \bar{E}_J by the ratio of I_{c1} to \bar{I}_c from Fig. 4-1), we get $E_{b1} \approx 4.2 E_{J1}$, even farther away from $E_b \equiv 0.199 E_J$. This is to be compared with measurements

¹See van der Zant (1991).

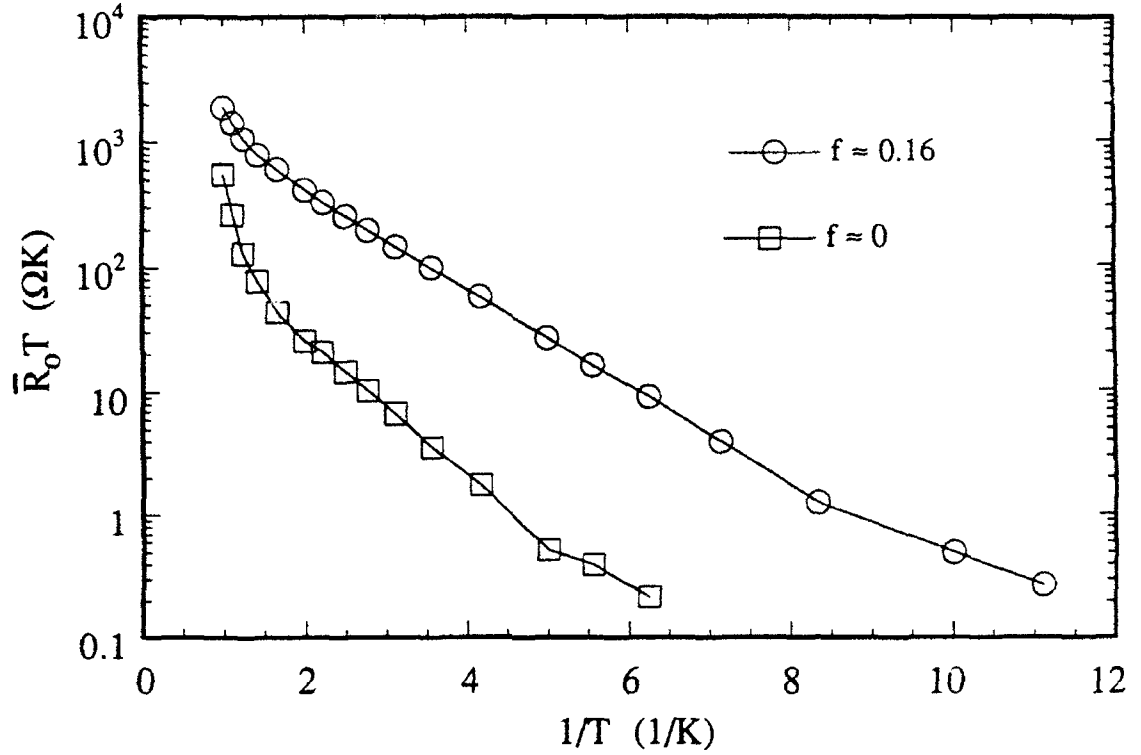


Figure 4-9.

$\bar{R}_0 T$ vs. $1/T$ for sample #4 at frustrations $f \approx 0$ and $f \approx 0.16$. As discussed in the text, the slope of the $f \approx 0.16$ curve should give the vortex pinning barrier.

with Rzechowski, *et al.* (1990) and van der Zant, *et al.* (1991a), which found energy barriers of $0.34 \bar{E}_J$ and $2 \bar{E}_J$ respectively. We do not have any clear explanation for the discrepancy. However, Lobb, *et al.* (1983) do neglect extrinsic pinning by local inhomogeneities and charging effects, both of which may be important.

4.2.3 Vortex Viscosity--Theory

Vortices will be damped by the resistive shunting of the junctions, the same mechanism that damps the oscillations of single junctions. Rzechowski, *et al.* (1990) calculate this damping in terms of the vortex drag coefficient η_0 , defined by the equation $F_{drag} = \eta_0 v$, with F_{drag} the drag force and v the vortex velocity. They calculate the vortex drag

coefficient as,

$$\eta_0 \approx \frac{\Phi_0^2}{a^2} \frac{1}{2R_n} \quad (4.6)$$

where Φ_0 is the flux quantum and a is the lattice spacing.

The vortex drag coefficient is proportional to $1/R_n$, so we expect the damping for these superconducting-insulator-superconducting (SIS) to be much smaller than that of the superconducting-normal-superconducting (SNS) arrays, which can have milli-Ohm resistances.¹ Indeed, as the junctions are underdamped, we would expect the vortex motion to be underdamped as well.² This would mean a hysteretic jump in voltage at the depinning current, as vortices become unpinned and can move freely (much like the hysteretic jump at I_c for a single junction). However, as Fig. 4-4 shows, we do not see this hysteretic jump in voltage, but instead see a signal of overdamped motion: a smooth increase of voltage with current.

Nakajima and Sawada (1981) predict a damping mechanism for vortices in arrays, with no equivalent for single junctions. They found, from numerical simulations, a moving vortex leaves a "wake" of junctions oscillating at their plasma frequencies. The moving vortex transfers energy to these junctions, whose oscillations damp slowly due to the shunting resistances.

Bobbert (1992) performed more detailed numerical simulations of a vortex in an array of underdamped junctions and also found this wake. Figure 4-10 shows some of his results: the vertical axis represents the total energy of a junction and the two lateral axes represent the position of that junction within the array.³ In this figure, we clearly see the vortex, moving towards the marked edge, and its wake.

¹For SIS junctions, R_n in Eqn. (4.6) is thought to be replaced by the quasiparticle resistance, which theoretically goes to infinity as $T \rightarrow 0$. If this holds, we would expect the drag coefficient to go to zero.

²See also Eikmans and van Himbergen (1992).

³The total energy of a junction refers to the sum of its kinetic energy $(1/2 C \Phi_0^2 (d\phi/dt)^2)$, ϕ being the phase difference across the junction) and the potential energy $(-E_J \cos\phi)$.

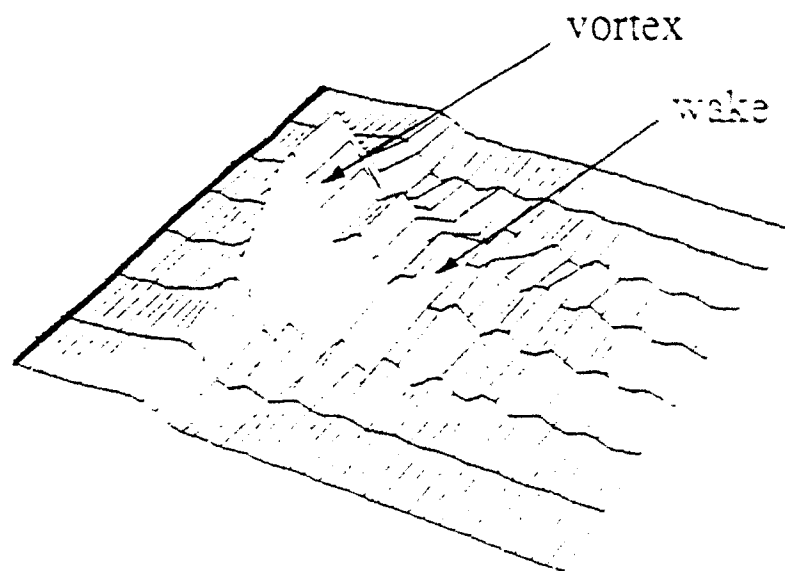


Figure 4-10.

This figure shows a moving vortex and its wake (P. Bobbert). The vertical axis represents junction energy, and the horizontal axes represent position within the array. Here the vortex moves towards the marked edge. We clearly see the wake trailing the vortex.

From his simulations, Bobbert could also calculate I-V curves, shown in Fig. 4-11. Four curves are shown for different values of the quality factor Θ (defined by $\Theta = \omega_p RC$, where R is thought to be, in our case, the quasiparticle resistance). In the flux flow region (for currents above I_d but below I_c , which is marked by the circles), the curves appear to approach an asymptotic form with increasing Θ . This suggests that there still exists vortex damping even in the limit of zero junction damping.

Geigenmüller, *et al.* (1993), expanding on the work of Bobbert,¹ explicitly determined

¹For Fig. 4-10, Bobbert approximated the sine term in the vortex equation of motion (Eqn. 2.25) as a triangular wave. While qualitatively describing the vortex motion, it fails quantitatively. For Fig. 4-11, he used instead a *truncated* triangle wave, which described the dynamics much more accurately, as confirmed by Geigenmüller, *et al.* (1993) who solved the equation with the full sine term.

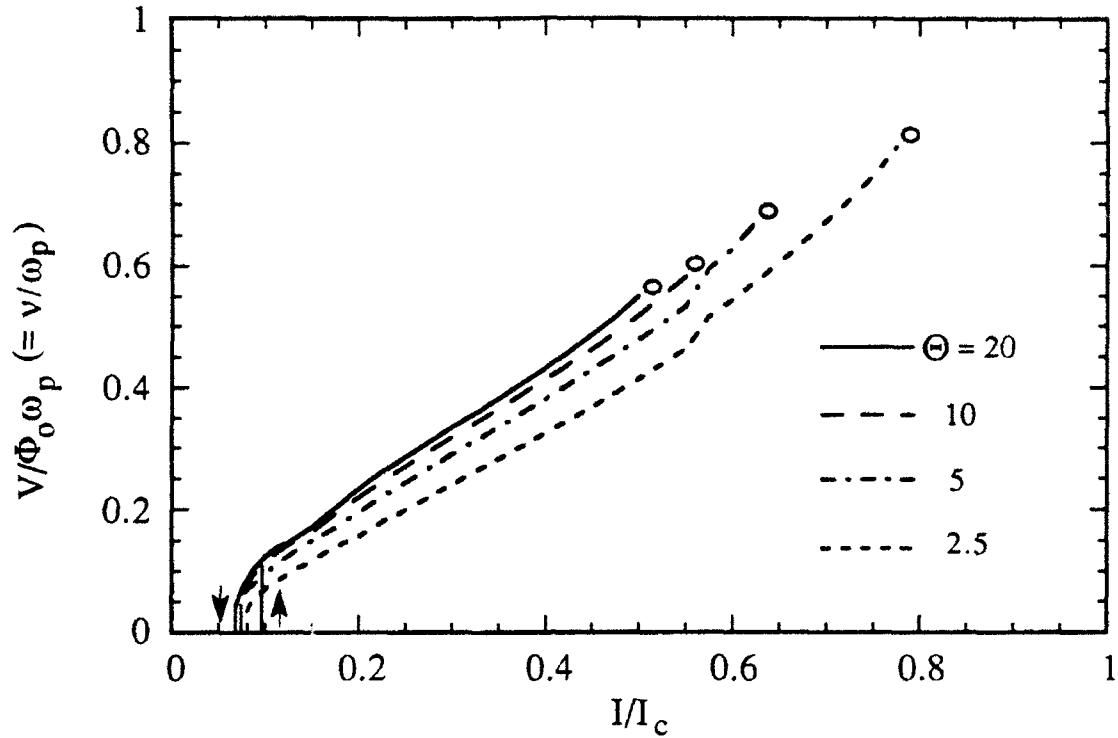


Figure 4-11.

Numerically simulated current-voltage curves for a 100 by 10 array for different values of the quality factor Θ (P. Bobbert). The normalization of the vertical axis equates it to v/ω_p , v the vortex frequency ($= 1/\text{time to traverse one unit cell}$). The arrows represent current direction for the $\Theta = 20$ curve, which shows hysteresis. The circles at the end of the lines mark the position of the critical current.

the drag coefficient for this damping mechanism η_{wake} to be

$$\eta_{wake} = \frac{\Phi_o^2}{a^2} \sqrt{\frac{2i_{co}C}{\pi\Phi_o}} = \frac{\Phi_o^2}{a^2} \sqrt{\frac{C}{\pi^2 L_{J0}}} \quad (4.7)$$

where L_{J0} is the Jospenson inductance of a junction, defined by $L_{J0} = \Phi_o / 2\pi i_{co}$. This result is independent of Θ , as expected from Fig. 4-11.

To give an intuitive feeling of the relative strengths of the two damping mechanisms, Geigenmüller, *et al.* (1993) also write Eqn. (4.7) in terms of η_o and Θ ,

$$\eta_{wake} \approx \frac{\Theta}{\pi} \eta_o; \quad \Theta > 1 \quad (4.8)$$

Here, as $\eta_o \sim 1/R \sim 1/\Theta$, we again recover a Θ -independent drag coefficient.

In the next section, we use the limiting form ($\Theta \gg 1$) of Bobbert's I-V curves in Fig. 4-11 [which gives rise to Eqns. (4.7) and (4.8)] to compare our results to his work and that of Geigenmüller, *et al.* (1993).

4.2.4 Vortex Viscosity--Experiment

In Sec. 4.1.1, Fig. 4-4 showed evidence for overdamped vortex motion.¹ In that figure, f is increased from $f \approx 0$ to $f = 0.22$ in steps of roughly 0.035. We see a regular increase with f in the developed voltage. If the independent vortex approximation held true for all frustrations, the curves in Fig. 4-4 should scale with f . To a large extent they do, except that the depinning current is somewhat dependent on f .

In Fig. 4-12, we take this into account in a simple way by plotting V/f vs. $\sqrt{(I/I_{d1})^2 - 1}$ (for all $f > 0$). This is a reasonable choice as (1) the standard result for a single overdamped junction for $I > I_c$ is $V \propto \sqrt{(I/I_c)^2 - 1}$ [see, for example, Van Duzer and Turner (1981), pg. 171] and (2) the I-V curves from the simulations of Bobbert (1992) in Fig. 4-11 appear to roughly follow this form. In Fig. 4-12, all the curves collapse into a common trend, except the curve at the smallest frustration, where the uncertainties in f and I_{d1} are the largest. For a *uniform* array following this form, we would expect the curves plotted in this fashion to be straight lines. We do not find straight lines in Fig. 4-12, so in modeling the data it appears important to include the array inhomogeneities.

To model the curves in Fig. 4-12, we take explicit account of junction inhomogeneities by treating the rows as separate, with the measured voltage being the sum of voltages from each row V_m . We approximate V_m by the form $V_m \propto \sqrt{(I/I_{dm})^2 - 1}$, where I_{dm} is the

¹See also van der Zant, *et al.* (1991b).

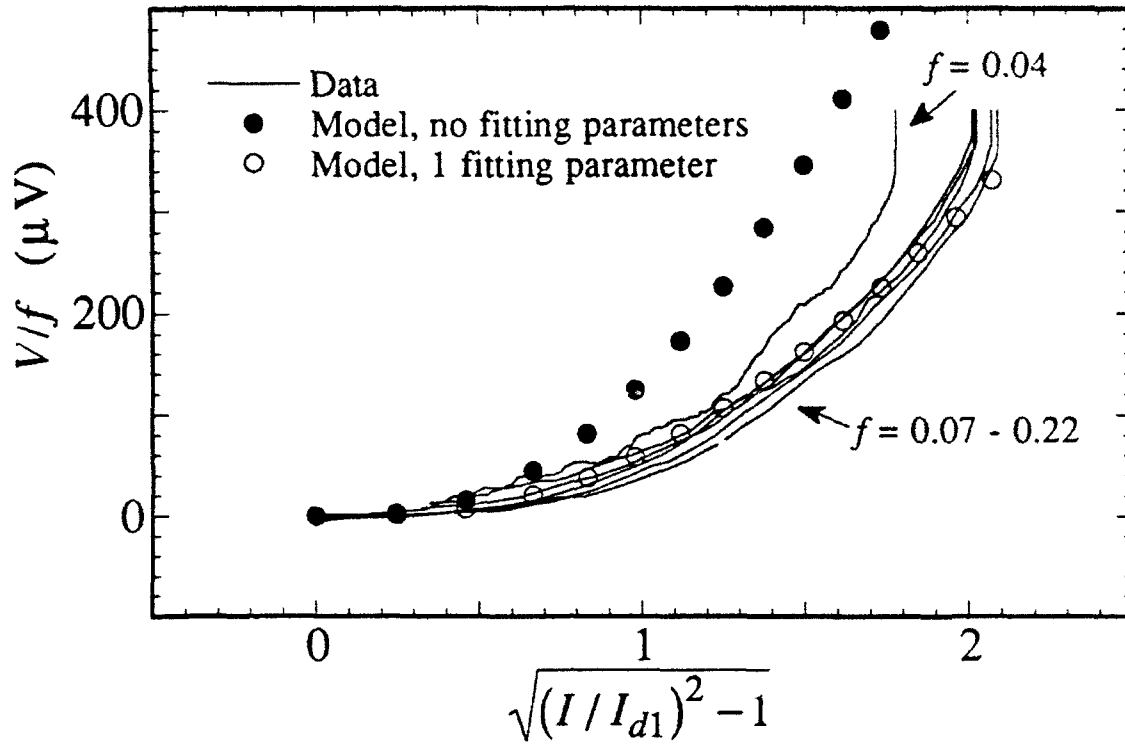


Figure 4-12.

This figure shows the curves of Fig. 4-6 (sample #4 at 50 mK) replotted with different axes, showing a rough collapse into a common trend. Included are two curves which model the data as described in the text: the filled circles give the model with no fitting parameters; with the open circles we scale the voltage values (by a factor of 2.12) in order to determine how well the *forms* of the curves match.

depinning current for the m^{th} row,

$$V = \sum_{m=1}^M V_m; \quad V_m = f\gamma \sqrt{\left(\frac{I}{I_{dm}}\right)^2 - 1} \quad (4.9)$$

with γ a constant.

From Bobbert's work in Fig. 4-11, γ is given by the curves' slopes, which approach unity (when plotted against I/I_c) in the limit of large quality factor Θ . From this we estimate that

$$\gamma \approx \kappa \Phi_0 \omega_p / 2 \quad (4.10)$$

where κ is defined by the relation $I_d = \kappa I_c / 2$ [from Lobb, *et al.* (1983), $\kappa \approx 0.199$].

Taking the distribution of critical currents of the rows from Fig. 4-1, one can compute the sum in Eqn. (4.9). However, as it appears this distribution is approximately uniform, we can analytically determine this sum in a continuum limit

$$V/f \approx \frac{M\gamma}{\alpha} \left[i \ln(i + \sqrt{i^2 - 1}) - \sqrt{i^2 - 1} \right]; \quad i \equiv \frac{I}{I_{d1}} \quad (4.11)$$

where M is the number of rows ($M = 70$) and α describes the normalized width of the distribution (assumed linear) of critical currents, $\alpha = (I_{cM} - I_{c1})/I_{c1}$. The data in Figure 4-1 gives $\alpha \approx 6$.

We plot Eqn. (4.11) as the filled circles in Fig. 4-12 with no free parameters. With the open circles, we scale the voltage values of the model by a factor of 2.12 in order to see that the *forms* of the curves match reasonably well. Though only a crude approximation, we see that this model predicts the data to within a roughly factor of two, and indicates that the upward curvature of the data curves has a simple explanation.

4.2.5 Vortex Critical Velocity

Nakajima and Sawada (1981), and following their work Bobbert (1992), predict a maximum vortex velocity.¹ When the vortex velocity is such that the frequency of phase slips (of the junctions over which the vortex crosses) reaches roughly half of the plasma frequency, they predict a succession of vortex-antivortex pairs to be created in the wake.²

¹Though not applicable here as we discuss this critical velocity and row switching in the independent vortex approximation (*i.e.*, for small frustrations), Octavio, *et al.* (1993) give an excellent discussion of row-switching for the $f = 1/2$ state.

²The critical value of $\approx 1/2 \omega_p$ comes from Nakajima and Sawada. Bobbert and Geigenmüller, *et al.* (1993) show that the fraction of ω_p actually depends on Θ . See, for example, Fig. 4-11.

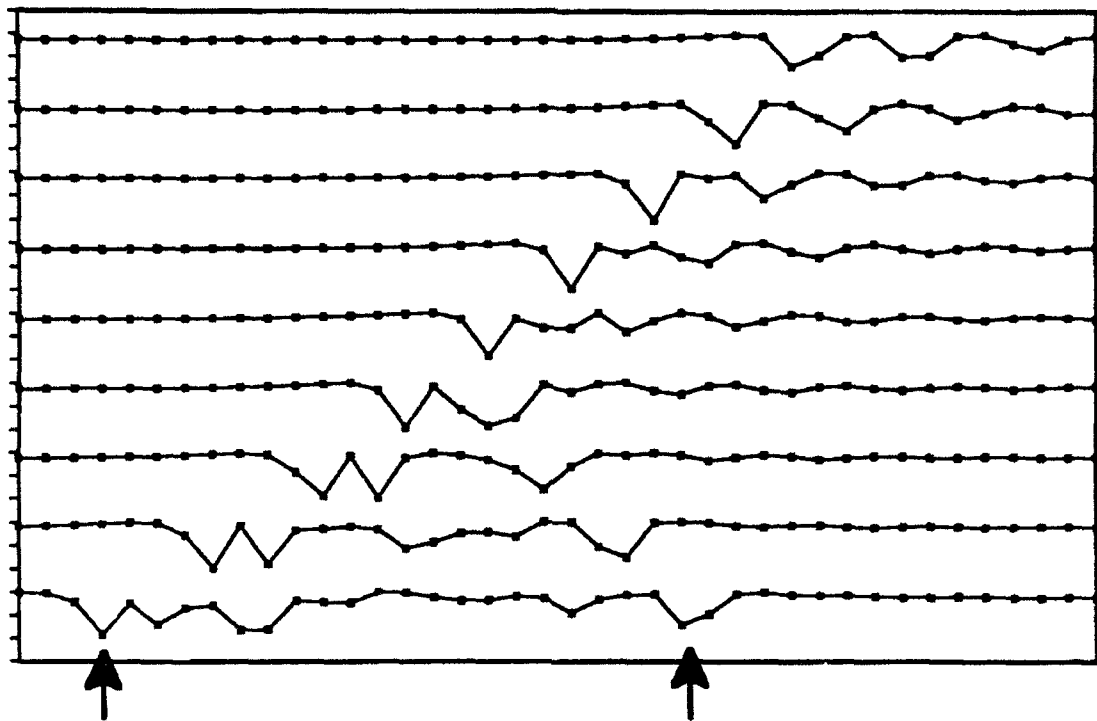


Figure 4-13.

Nine "snapshots" of the supercurrent vs. position along part of the center row of a 100 by 10 array, $\Theta = 5$ (P. Bobbert). The bias current in the numerical simulations has just been stepped up such that the vortex now exceeds its critical velocity. The arrows in the bottom curve show the original vortex, and the created antivortex. Time increases top to bottom, with an interval of $4/\omega_p$, and the division on the vertical axis is i_c .

The vortices in these pairs move in opposite directions, due to opposite $\mathbf{j} \times \mathbf{B}$ forces, and in turn nucleate additional pairs. This breakdown results in a row switching from a zero voltage state to a gap voltage state.

Fig. 4-13 shows this phenomenon. What is seen is the different steps in time for a vortex moving along the center row of the array (the horizontal axis represents the position of a junction in the array along the center row and the vertical axis represents the supercurrent through that junction). We see a vortex moving towards the left, nucleating a vortex-antivortex pair: the vortex of the same sign moves along with the original one and is difficult to see. The vortex of the opposite sign can readily be seen moving in the opposite

direction.

In our measurements we see evidence for this maximum vortex velocity. The data in Fig. 4-12 show this, namely a constant value of V/f where the first row switches. (As the measured voltage per vortex is proportional to vortex velocity, this maximum voltage per vortex suggests a critical vortex velocity).

From this maximum value of $V/f \approx 360 \mu\text{V}$, we can determine a measured critical velocity and compare it with the theoretical predictions. Starting with Eqns. (4.9) and (4.10), we approximate the voltage developed per row as V_m . Writing this voltage in terms of the vortex velocity for the m^{th} row using Eqn. (4.1), we get

$$v_m = \frac{a}{\Phi_o} \frac{V_m}{f} = \frac{a\gamma}{\Phi_o} \sqrt{\left(\frac{I}{I_{dm}}\right)^2 - 1} \quad (4.12)$$

As this equation shows, for a given bias current, the vortex velocity will be largest for the row which has the minimum depinning current, e.g., I_{d1} . In this row, vortices will first exceed the critical velocity and cause the row to switch. Replacing I_{dm} with I_{d1} , this gives $v_1 \approx (a\gamma / \Phi_o) \sqrt{i^2 - 1}$ with $i = I/I_{d1}$. The maximum vortex velocity v_{max} is just given by v_1 evaluated at $I = I_{c1}$, the current at which the first row switches.

To compare with theory, it is easier to discuss the vortex velocity in terms of its angular frequency ω , where $\omega = 2\pi/\text{time it takes for a vortex to travel across one unit cell}$. As $\omega = 2\pi v/a$, this gives $\omega_1 = (2\pi\gamma / \Phi_o) \sqrt{i^2 - 1}$. Using the value of γ from Eqn. (4.10) and the measured value of i where the first row switches ($i \approx 2.27$ from Fig. 4-12), this gives $\omega_{max} \approx 2.8 \times 10^{11} \text{ rad/sec}$. However, as we see in Fig. 4-12, this value of γ overestimates the data by roughly a factor of two. Using a value of γ which gives a better fit to the data, this gives $\omega_{max} \approx 1.5 \times 10^{11} \text{ rad/sec}$. With our simple approximations, this agrees with the estimated value of Nakajima and Sawada of $1/2 \bar{\omega}_p \approx 1.1 \times 10^{11} \text{ rad/sec}$.

This rough agreement should be taken lightly, however, as (1) it is unclear as to

whether it is appropriate to compare ω_{max} , (defined for the weakest row $m = 1$) with the average plasma frequency $\bar{\omega}_p$ and (2) Bobbert and Geigenmüller, *et al.* show that the critical fraction of ω_p (1/2 according to Nakajima and Sawada) depends on Θ .

CHAPTER FIVE

MEASUREMENTS AND DISCUSSION ON TRANSITIONAL ARRAYS

As discussed in the introduction, for a single Josephson junction there exists an uncertainty relation between ϕ and Q , where ϕ is the difference in phases (of the superconducting order parameter) across the junction and Q is the junction's capacitive charge. Restating Eqn. (1.4), the form of this uncertainty relation is

$$\Delta\phi\Delta(Q/2e) \geq 1 \quad (5.1)$$

Iansiti (1988) and references therein give the simplest form of the single junction Hamiltonian H_o as¹

$$H_o(\phi, Q) = E_c \frac{Q^2}{e^2} - E_J \cos \phi \quad (5.2)$$

If the Josephson energy E_J is much greater than the charging energy E_c , then $E_J \cos \phi$ is the dominant energy term in Eqn. (5.2) and the system dynamics are best solved by treating ϕ as a well-defined variable and Q as undefined [we replace Q by V/C where V is related to ϕ by the Josephson relation $V = (\hbar/2e) d\phi/dt$]. This is the case for the classical junctions of the type used in the arrays discussed in chapter 4. On the other hand, if E_J is much *less* than E_c , we again recover a "classical" regime where we treat Q as the well-defined variable (we will discuss this case in the next chapter). However, for $E_J \sim E_c$, to

¹ The full Hamiltonian includes a term describing the influence of the junction "environment" and a term describing the current or voltage source.

Table 5.1 Parameters for samples #6 and #7.

Sample #	Metal	junction area (μm^2)	R_n ($\text{k}\Omega$)	C (fF)	E_J/k_B (K)	E_C/k_B (K)	E_J/E_C
6	Sn	0.10 ± 0.01	201	2.5 ± 0.6	0.11	0.37 ± 0.12	0.30 ± 0.08
7	Al	0.007 ± 0.001	22.9	0.75 ± 0.05	0.40	1.2 ± 0.1	0.32 ± 0.02

describe correctly the system we cannot make the simple approximation that either ϕ or Q is a well-defined classical variable. Stating this in a different fashion, from Eqn. (5.1) both $\Delta\phi$ and ΔQ will be non-negligible, *i.e.*, the variables will experience strong quantum fluctuations. These are the junctions we describe here.

Section 5.1 gives some of the general features of two arrays, #6 and #7, which consist of junctions with $E_J \sim E_C$. In Sec. 5.2, we discuss the results in detail, specifically the temperature dependence of the low-voltage resistance R_0 .

5.1 General Results of Measurements

The parameters of samples #6 and #7 are given in Table 5.1. Sample #6 is a 50 by 70 tin array, similar to samples #1 - #5 discussed in the previous chapter, but with a normal resistance nearly an order of magnitude larger (gained by allowing the junction oxide layer to grow thicker). This relatively large normal resistance depresses E_J below E_C , so that E_J/E_C is roughly 0.30.

Sample #7 is an aluminum array, also 50 by 70 unit cells, but with a smaller junction area: $0.007 \mu\text{m}^2$ compared to $0.10 \mu\text{m}^2$ for #6. The smaller area results in a larger charging energy for #7. However, because its relatively low normal resistance ($\approx 23 \text{ k}\Omega$) leads to a like increase in the Josephson energy, the two arrays have roughly the same value of E_J/E_C .

The general features of the I-V curves for sample #6 closely resemble those of the samples discussed in the previous chapter, as seen in Fig. 5-1(a). We measure row

switching and hysteresis with critical and retrapping currents. A substantial difference between the I-V curves of #6 and those of #1 - #5, however, is that for #6 we measure a non-zero R_o over our entire temperature range. [Figure 5-1(b) shows an expanded view of the low-voltage region at 50 mK.] Indeed, as R_o pins at a finite value for temperatures below ~ 100 mK, it appears that there exists no true "supercurrent" branch with zero resistance, even at $T = 0$.

For sample #7, the current-voltage characteristics show a remarkably different behavior. Figure 5-2(a) shows an I-V curve at a temperature of 15 mK. We measure no hysteresis or switching events, and although one can see evidence of a critical current, the smooth nature of the curve makes a unique value of I_c difficult to determine. Figure 5-2(b) shows the center region of the I-V curve at an expanded scale. At the origin, we measure a voltage gap not previously seen in samples #1 - #6 (we show the gap at $f = 1/2$, as it is more pronounced at this frustration than at $f = 0$). This gap is thought to be similar in nature to the Coulomb blockade measured in like single junctions [Geerligs, *et al.* (1989)].¹ Because of this blockade, for small biases the array tends toward *insulating* behavior.

5.2 Discussion of Results

As the results for the two samples are quite different, we discuss them each in their own section; Sec. 5.2.1 for sample #6 and Sec. 5.2.2 for sample #7. In Sec. 5.2.3, we compare the two samples to each other, and to the relevant predictions of a theory by Fazio and Schön (1991).

5.2.1 Sample #6

As seen in Fig. 5-1(a), the I-V curves for sample #6 appear to be of a similar type to

¹In single junctions, experimentally the gap is not as pronounced, thought to be due to a larger coupling to the external environment [Cleland, *et al.* (1992) and Delsing, *et al.* (1989a)].

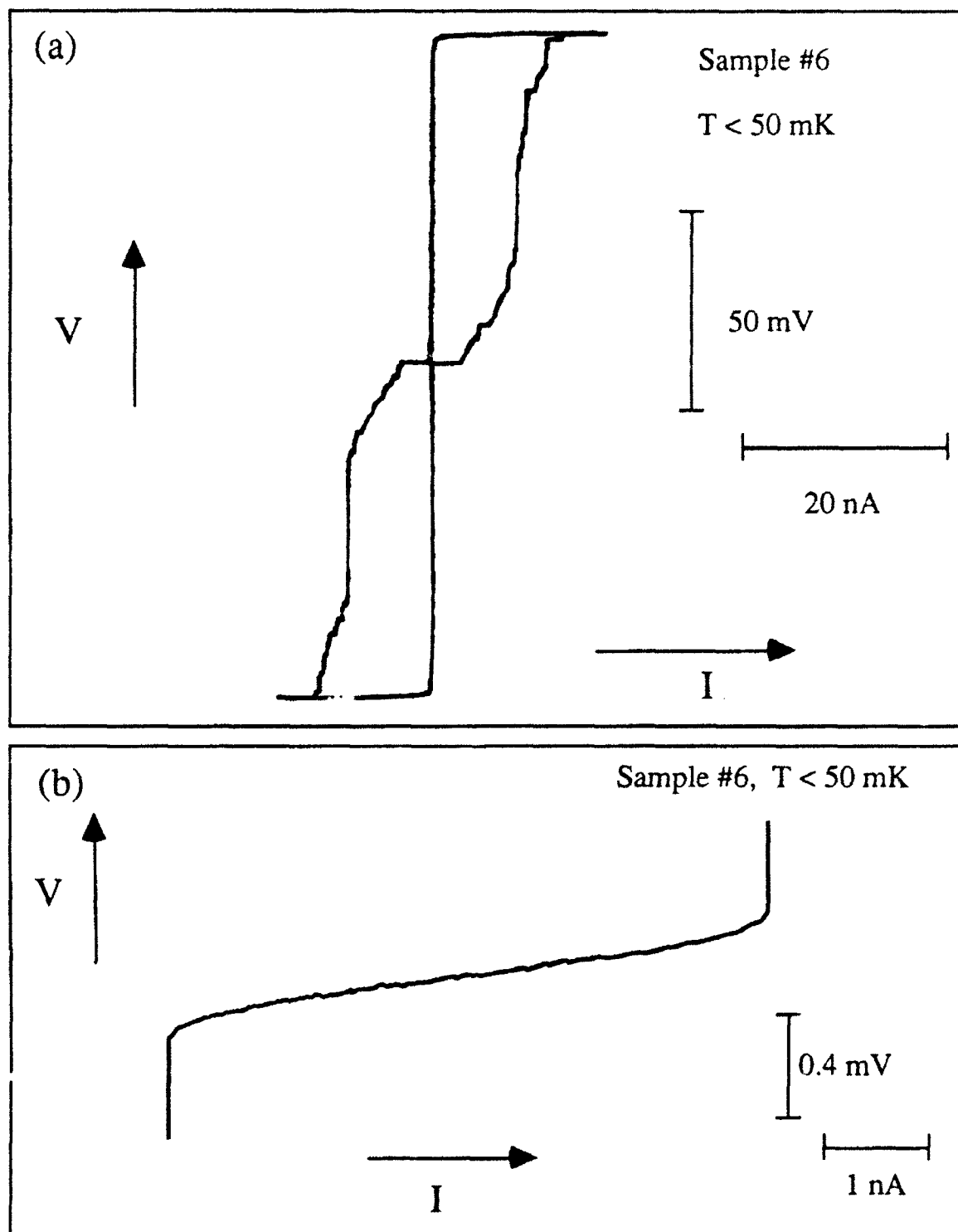


Figure 5-1.

I-V curves for sample #6 at a temperature of $T < 50$ mK. In (a), we see the "supercurrent" branch and the hysteretic switches to the quasiparticle branch, as described in Chapter 4. An expanded view of the "supercurrent" branch is given in (b), which shows a nonzero value of resistance.

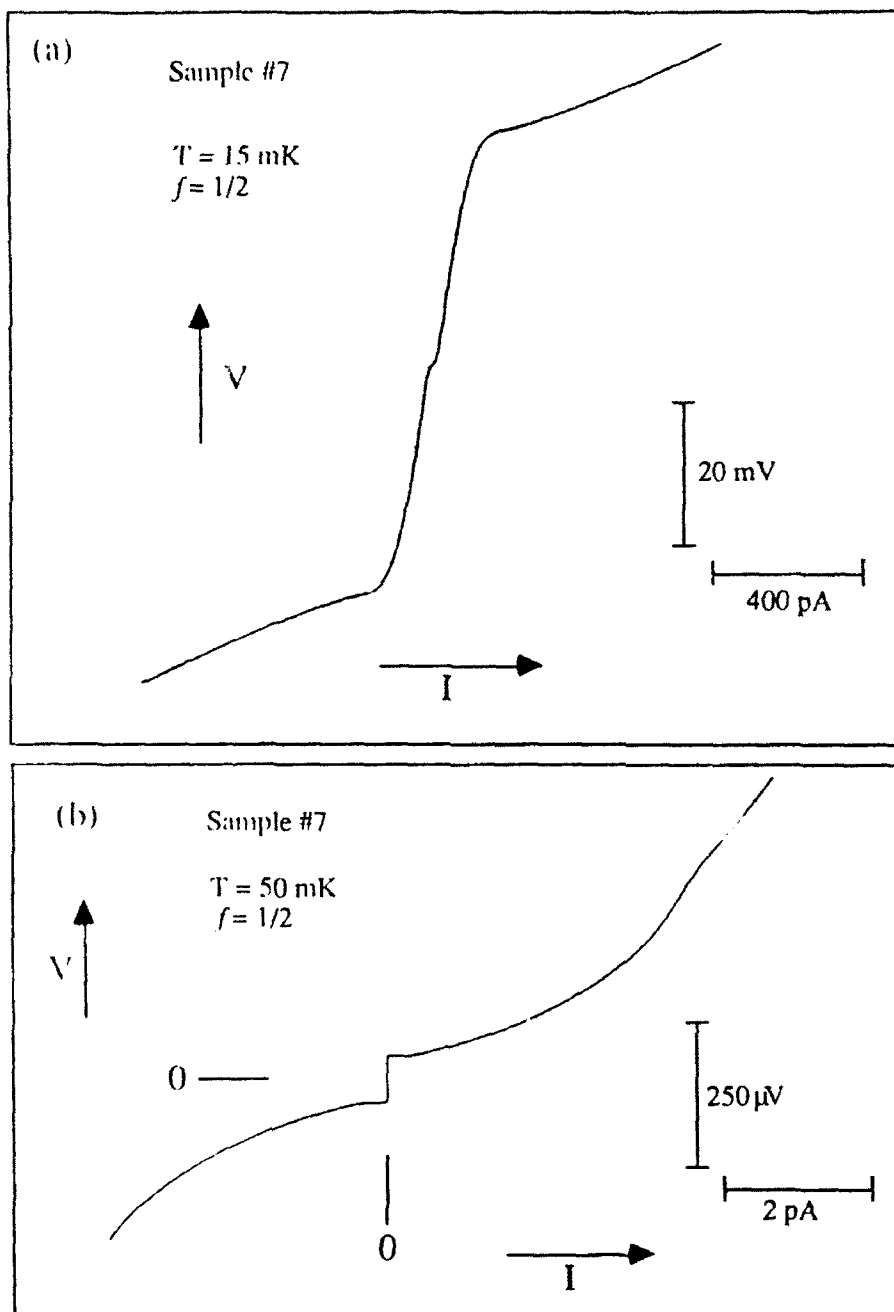


Figure 5-2.

I-V curves for sample #7 at a temperature of $T = 15 \text{ mK}$. In (a) we see the superconducting gap, as well as remnants of a critical current. Curve (b) shows an expanded view of the region about the origin; here we see the Coulomb blockade region. The curves are at frustration $f = 1/2$.

those in the classical regime ($E_J \gg E_c$) discussed in chapter 4. We therefore find it useful to treat this array classically, still describing the dynamics in terms of vortex motion. However, we allow the charging effects to act as a perturbation, *i.e.*, we treat the superconducting phase differences not as well localized, but as each having a spread of values peaked about a mean.¹ We may think of these phase differences then as having quantum fluctuations about this mean value.

As the vortex position is largely defined by the relative phases in the array, quantum fluctuations in these phases translates to quantum fluctuations in the vortex position. There exists, then, a non-zero probability of a vortex moving from well to well in the absence of thermal fluctuations. The vortex will quantum mechanically tunnel *through* the pinning barrier. This description, also called quantum creep, belongs to a general class of phenomena called macroscopic quantum tunneling (MQT), as it involves the tunneling of macroscopic variables, in this case the superconducting phase differences across each junction.

For high enough temperatures, thermal fluctuations in the phase differences will mask these quantum fluctuations and the array will behave classically. In this limit, we expect to find thermally-activated vortex motion, and the low-voltage resistance R_0 should follow the Arrhenius form of Eqn. (4.4). However, for temperatures less than some cross-over value, T_{cr} , the thermal activation rate will fall below that of quantum tunneling. Grabert, *et al.* (1987) predict that for the highly analogous case of phase slips in a single junction, the rate for quantum tunneling is largely temperature *independent* as $T \rightarrow 0$. This suggests that the equivalent vortex tunneling rate and hence R_0 should also become independent of temperature in this limit.

Grabert, *et al.* determined this cross-over temperature, from thermal activation to quantum tunneling, to be $k_B T_{cr} \approx \hbar \omega_p / 2\pi$, with $\hbar \omega_p \approx \sqrt{8E_c E_J}$ in the case of phase slips

¹Iansiti (1988) approximates the nature of this spread as a Gaussian function, with an rms width proportional to the fourth root of E_c/E_J .

in a single junction. Using the analogy between single junction phase slips and vortex motion given in chapter 2 [Eqns. (2.25) and (2.26)],¹ we use the Grabert, *et al.* value to estimate that for vortices, T_{cr} is given by

$$k_B T_{cr} \approx \hbar \omega_o / 2\pi \quad (5.3)$$

where $\hbar \omega_o = \sqrt{8\kappa E_c E_J}$ (κ is defined by the equation $E_b = \kappa E_J$). For sample #6, Eqn. (5.3) gives a cross-over temperature of roughly 40 mK if we use $\kappa \approx 0.199$, the Lobb, *et al.* (1983) value of the pinning barrier [Eqn. (2.22a)]. Using instead $E_b = 1.0 E_J$, the barrier value measured for a similar array, sample #4, we get $T_{cr} \approx 100$ mK.

Figure 5-3 shows R_o as a function T for sample #6. Upon decreasing the temperature from T_c (≈ 4 K), R_o shows a slight increase, the origin of which is unclear. Below a temperature of $T \approx 1.2$ K, R_o falls in a similar fashion to samples #1 - #5. However, as the inset shows, R_o does become temperature independent as $T \rightarrow 0$. The inset also shows one of the two values of T_{cr} discussed above, $T_{cr} \approx 100$ mK. This value appears to match the data closely, as 100 mK sits in the middle of the transition from temperature dependence to temperature independence. The close agreement of the theoretical and experimental cross-over temperatures may be viewed as somewhat fortuitous, however, given that we did not specifically measure E_b in this sample and are instead using sample #4's value.

Nonetheless, it does indicate a reasonable agreement with theory.

This evidence for macroscopic tunneling of vortices is preliminary, as the value of frustration was not determined before an unknown event degraded this sample. However, we do feel that the flattening off of R_o at low temperatures is a real effect and not caused by sample self-heating. As mentioned in Sec. 3.4, upon applying a magnetic field of roughly 50 gauss,² we do see temperature dependence in R_o all the way down to 50 mK; this is a

¹Derived by Rzchowski, *et al.* (1990), and later verified by van der Zant (1991).

²By decreasing E_J and hence the energy barrier with a sufficiently strong magnetic field, we can increase thermal activation of the vortices enough so that it dominates over quantum tunneling for our entire

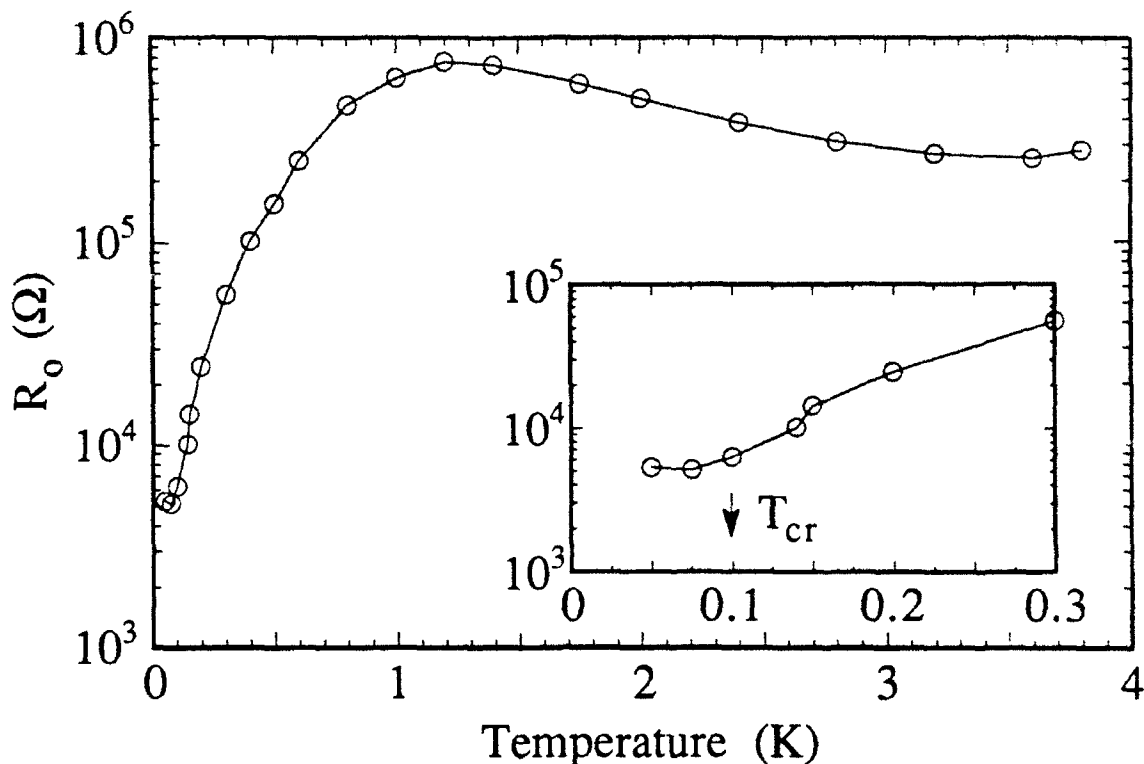


Figure 5-3.

Low-voltage resistance R_0 vs. temperature for sample #6. The inset shows an expanded view of the low-temperature data, where we see a flattening out of R_0 associated with the quantum tunneling of vortices. The T_{cr} marked on the plot refers to the theoretical cross-over temperature where the flattening should occur, as discussed in the text. The value of frustration is not known for this curve.

good indication that sample self-heating is not a serious limitation in reaching these low temperatures.

5.2.2 Sample #7

Figure 5-4 shows a plot of R_0 vs. T for sample #7 (as with all of the samples, we determine R_0 from the slope, around zero bias, of the dc I-V curve). Upon decreasing the temperature from T_c , R_0 initially falls in a similar fashion to sample #6.¹ However, below

temperature range.

¹ As with sample #6, we in fact measure a slight initial *increase* in R_0 upon decreasing the temperature from T_c . The origin of this rise is not clear.

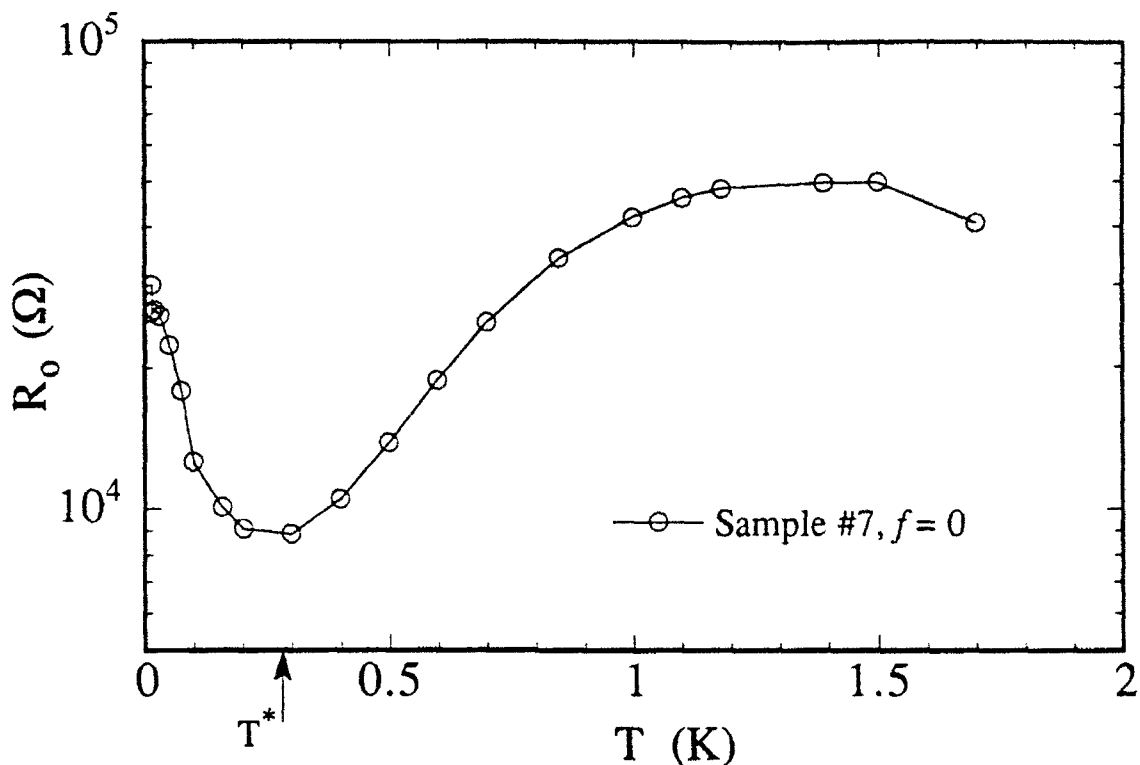


Figure 5-4.

The low-voltage resistance R_0 vs. T for sample #7 at $f = 0$. Here we see reentrant behavior at temperature $T^* \approx 280$ mK. For temperatures below T^* , a Coulomb gap develops, similar to that in Fig. 5-2.

some temperature T^* , the resistance starts rising again. As determined by inspection of the I-V curves, this rise reflects the development of the Coulomb blockade within the “supercurrent” branch.¹

Zaikin (1991) predicts this reentrant behavior at T^* . At $T = 0$ and for normal resistances greater than the quantum resistance R_Q ($R_Q \equiv h / 4e^2 \approx 6.5$ kΩ), he argues that due to the non-negligible charging energy, all of the charges are localized (*i.e.*, bound) on the islands and therefore cannot contribute to the current: the array is insulating. For finite

¹ At temperatures below ≈ 50 mK, R_0 flattens out and becomes temperature independent. This may be due to effects involving quantum fluctuations, similar to those discussed for sample #6. However, in this case sample self-heating at these low temperatures has not been ruled out.

temperatures, but less than T^* , current may flow due to the thermal activation of the charges, and the conductance rises (resistance falls) with increasing temperature. At temperatures above T^* , Zaikin suggests that the charges are sufficiently delocalized (unbound) so that the array may be treated classically in terms of vortex dynamics (hence we see the rise in R_o with increasing temperature, similar to that found for the arrays in Chapter 4).

At T^* , Zaikin argues there exists a competition between the thermal activation of both charges and vortices. He estimates this temperature (in the limit of $R_n \gg R_Q$) as

$$k_B T^* = \frac{16^3}{\sqrt{8}\pi^2} \sqrt{\frac{E_J^3}{E_c}} \exp\left(-8\sqrt{\frac{2E_J}{E_c}}\right) \quad (5.4)$$

Plugging in the values for E_c and E_J for sample #7, this gives $T^* \approx 50$ mK, which underestimates the measured value, ≈ 280 mK, by over a factor of 5. The reason for this discrepancy is not clear, although the normal resistance for sample #7 is not greatly larger than the quantum resistance ($R_n/R_Q \approx 3.6$), and may not satisfy the limits of Eqn. (5.4), i.e. $R_n \gg R_Q$.¹

The Coulomb blockade width we measure is highly dependent on frustration. In Fig. 5-5 we see a series of I-V curves taken about the Coulomb gap for different values of f at 15 mK. Though difficult to see, there does exist a gap in curve (a) at $f = 0$. The gap for each of the other curves ($f \neq 0$) is clearly visible. The size of the gap is periodic in f : the $f = 1$ curve resembles that of the $f = 0$ curve. Figure 5-6 shows this dependence on frustration by plotting R_o vs. T for sample #7 at $f \approx 0$ and $f = 1/2$. We see that at the lowest temperatures, R_o is over 2 orders of magnitude greater for $f = 1/2$ than for $f = 0$.

¹Zaikin's arguments may also apply to sample #6, where we have instead chosen to discuss the data in terms of quantum tunneling of vortices. Using Zaikin's approach, the leveling off of R_o at low temperatures we measure would reflect a crossover to *increasing* R_o as $T \rightarrow 0$. We would not measure this increase if it occurred at temperatures below our experimental limits. From Eqn. (5.4), T^* is roughly 18 mK for sample #6.

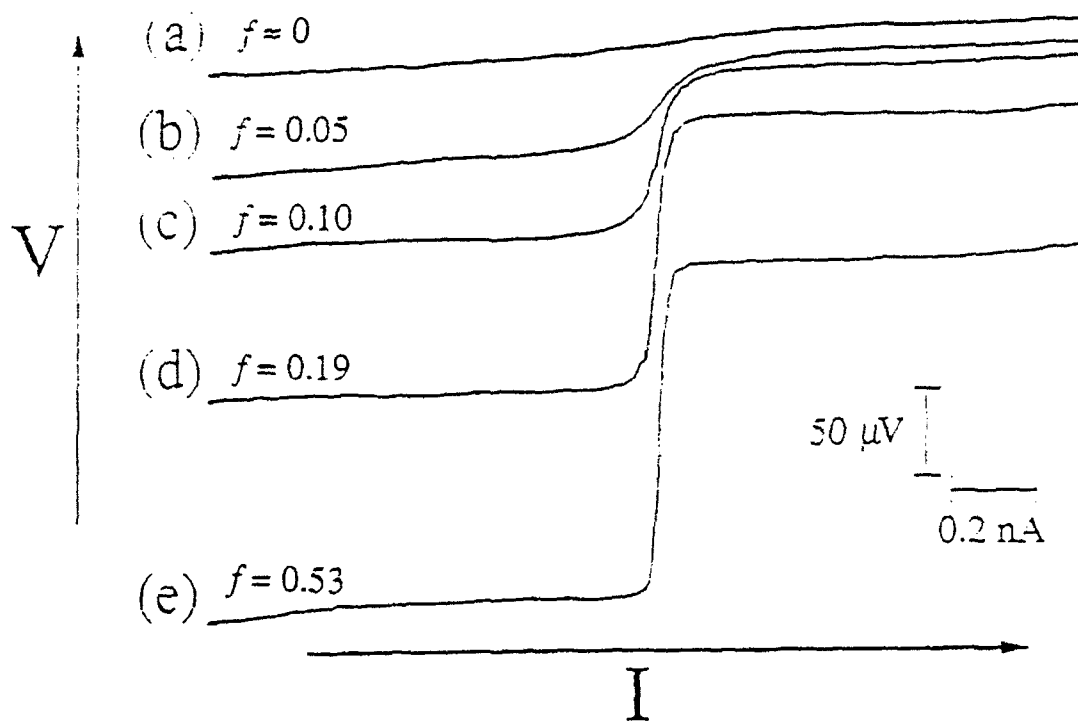


Figure 5-5.

I-V curves showing the development of the Coulomb gap with frustration for sample #7 at 15 mK.

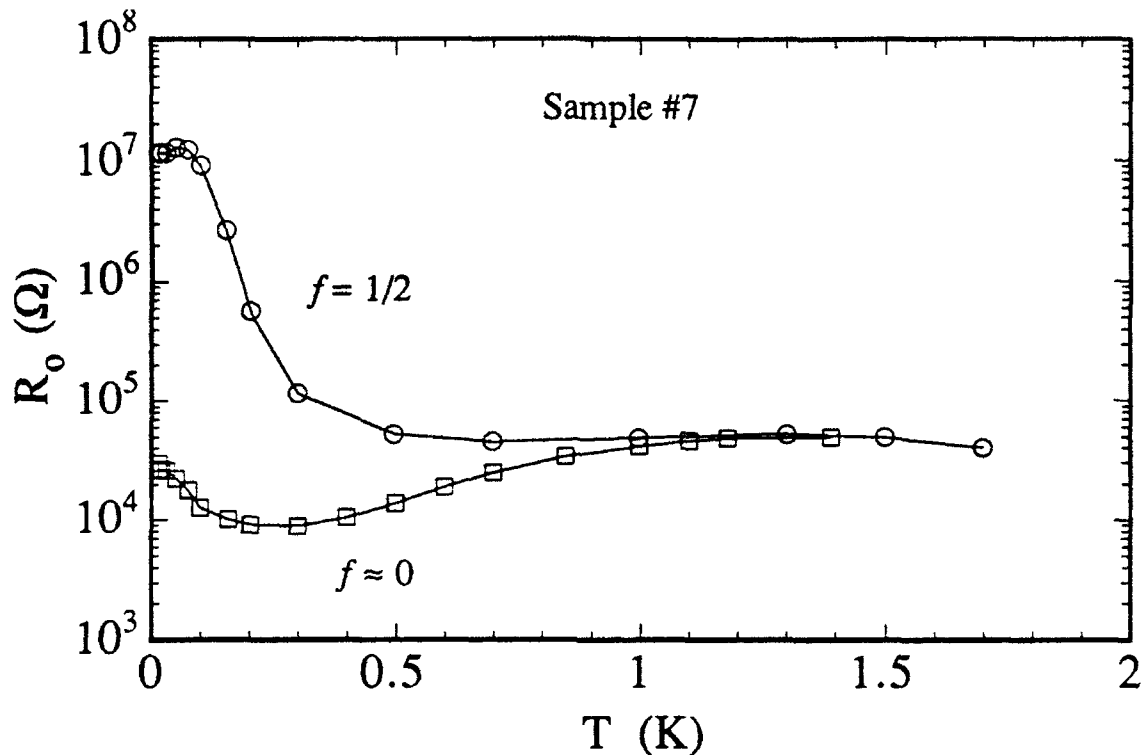


Figure 5-6.

R_0 vs. T for sample #7 at two values of frustration, $f \approx 0$ and $f = 1/2$. At $T = 0$ the resistance for the $f = 1/2$ case is over two orders of magnitude greater than that for $f \approx 0$.

We can explain this dependence on frustration if we allow the superconductor-to-insulator (S-I) transition to depend on magnetic field. Fisher (1990) argues this point theoretically, predicting that, with an applied magnetic field, one can *tune* an array to sit right at the S-I boundary.¹ For fields greater than this critical value at $T = 0$, the array is insulating, and for fields below it, the array is superconducting. We cannot fully apply these ideas to sample #7, though, as we do not measure superconducting behavior for any frustration.² However, at $f \approx 0$ the array is only weakly insulating (*i.e.*, less resistive),

¹ See also Granato and Kosterlitz (1990).

² Strictly speaking, as R_0 flattens off to a finite value at low temperatures, the arrays show only *metallic* behavior at $T = 0$. However, from inspection of the R_0 vs. T curves (see Figs. 5-3 and 5-4), one can determine whether an array *tends* toward superconducting or insulating behavior.

compared to $f \approx 1/2$.¹ This suggests that at zero frustration, the array is *just* on the insulating side of the transition. Increasing f places it more firmly on the insulating side, leading to a more pronounced gap. Recent work by van der Zant, *et al.* (1992a), reports finding this field-tuned transition in a similar array.² As their value of E_J/E_c (≈ 0.9) is larger than that for #7 (≈ 0.32), we might expect their array to show superconducting behavior at low frustrations; it will be more superconducting in general.

5.2.3 Comparison of the Two Samples

Fazio and Schön (1991) report a theoretical phase diagram for the S-I transition.³ Figure 5-7 shows the $T = 0$ plane of this diagram, plotting E_J/E_c vs. α_t , where $\alpha_t \equiv R_Q/R_n$ (they treat the case of quasiparticle dissipation). The diagram consists of two phases, insulating and superconducting. Fazio and Schön give the critical value of E_J/E_c at the boundary as

$$\left(\frac{E_J}{E_c} \right)_{crit.} = a \frac{2}{\pi^2} - \frac{3}{16} \alpha_t^2 \quad (5.5)$$

where a is a constant, slightly greater than or equal to 1. (In Fig. 5-7, we take $a = 1$ for simplicity.) Equation (5.5) holds for $\alpha_t < 0.4$. For α_t greater than this value, the critical value of E_J/E_c falls quickly to zero at $\alpha_t \sim 0.45$. Also in Fig. 5-7 we see the placement of samples #6 and #7.

The position of sample #6 on the phase diagram, in the superconducting phase, appears to match the experimental results. The I-V curves, and the plot of R_o vs. T in Fig. 5-3

¹ We do not measure commensurate effects with these arrays, and the maximum blockade width occurs at $f = 1/2$.

² They measure a 60 by 190 array with aluminum junctions similar to ours.

³ See also van der Zant, *et al.* (1992c).

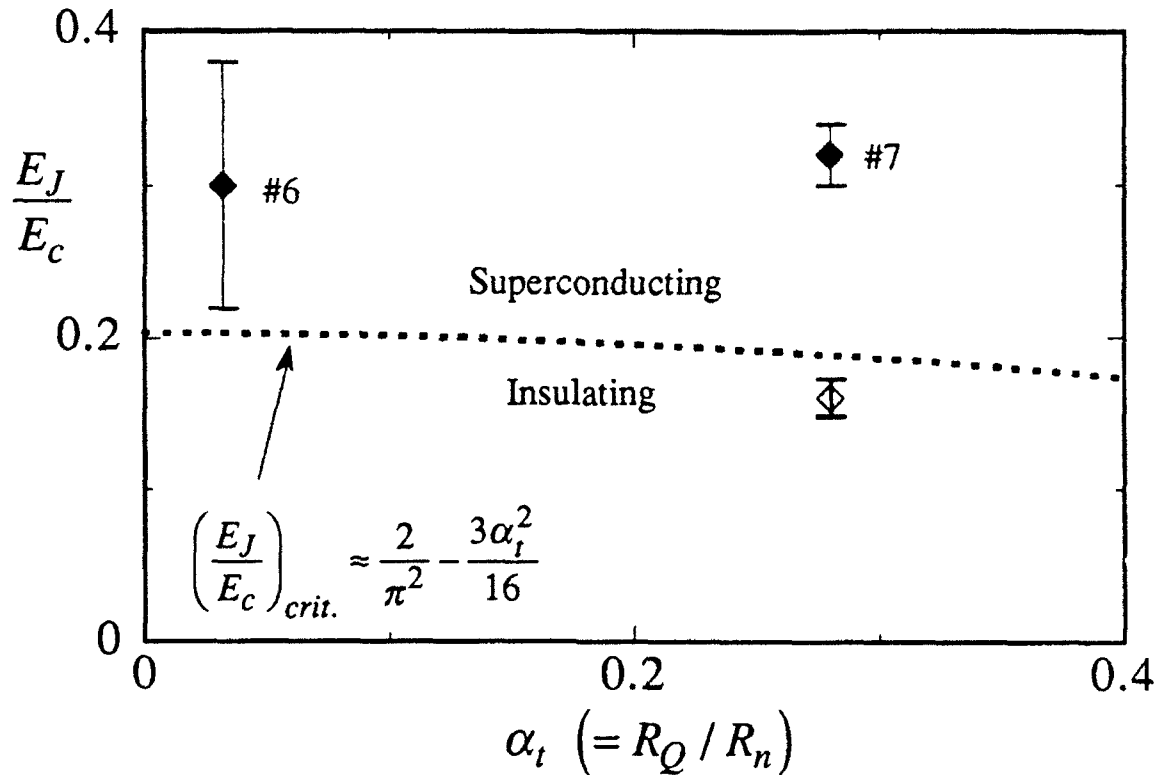


Figure 5-7.

Part of a phase diagram reported by Fazio and Schön. For $T = 0$, arrays above the dashed line [described by the Eqn. (5.5)] are predicted to be superconducting, while those below it are predicted to be insulating. The positions of samples #6 and #7 are marked by filled diamonds (as there exists a factor of 2 uncertainty for the vertical position of sample #7 as described in the text, we indicate the other value by an open diamond). The error bars in the vertical direction reflect uncertainties in the capacitance measurements (the error bars for sample #7 are smaller than that for sample #8 due to the more accurate method of determining capacitance).

indicate that this sample does tend toward superconducting behavior as $T \rightarrow 0$.¹ The position of sample #7, however, does not appear to agree with the experiments. Though #7 also lies on the superconducting side of the transition, Figs. 5-4 and 5-5 show that this sample in fact tends toward insulating behavior in the both the $f = 0$ and $f \neq 0$ cases, respectively.

¹For sample #6, it appears that R_0 approaches a non-zero value as $T \rightarrow 0$, so it can not be considered a "superconducting" array. However, both the general form of the I-V curves and the behavior of R_0 at higher temperatures resemble that of samples #1 - #5. We therefore state this sample *tends toward* superconducting behavior.

There are at least two possible explanations for this discrepancy concerning sample #7. First, our approximation that $a = 1$ in Eqn. (5.5) may be incorrect. A larger value of a would push the S-I boundary out to higher values of E_J/E_c , and possibly encompass #7 on the insulating side of the phase diagram. Taking into account the uncertainties in the values of E_J/E_c for #6 and #7 (denoted by the vertical error bars in Fig. 5-7), for $a \approx 1.6 - 1.7$ the boundary falls such that #6 lies on the superconducting side while #7 lies on the insulating side, in agreement with the measurements.

The second explanation is that for sample #7, the value of E_c we give may be too small by a factor of 2. As discussed in the following chapter, for sample #7 we determine C from the measured offset voltage V_{off} using *local* rules.¹ Using *global* rules we get a value half as large for C , or double E_c . This would give $E_J/E_c \approx 0.16$ for sample #7, correctly placing it on the insulating side of the transition. We denote this point with the open diamond in Fig. 5-7.

Other factors which may be involved are: (1) the two samples are made with different materials, tin and aluminum for #6 and #7, respectively, (2) as the position of the S-I boundary is dependent on frustration, interpreting the data is hampered by not knowing the value of f for sample #6, and (3) the I-V curves for sample #6 (Fig. 5-1) indicate it to have more inhomogeneity than sample #7 (Fig. 5-2).

However, whatever the reason for the discrepancy, it is interesting to note that R_o of the two arrays behaves in a nearly-dual manner. Figure 5-8 shows R_o for both arrays plotted against T/T_c [curve (a) shows the data for all temperatures below T_c while curve (b) shows an expanded view of the low-temperature data]. The two curves nearly mirror each other both in the curvature, and in the relative positions of the peaks and valleys. These curves appear to reflect the dual nature of the conjugate variables ϕ and Q .

¹We determine C differently for sample #6 (discussed in Chapter 4), so the following discussion does not apply to it.

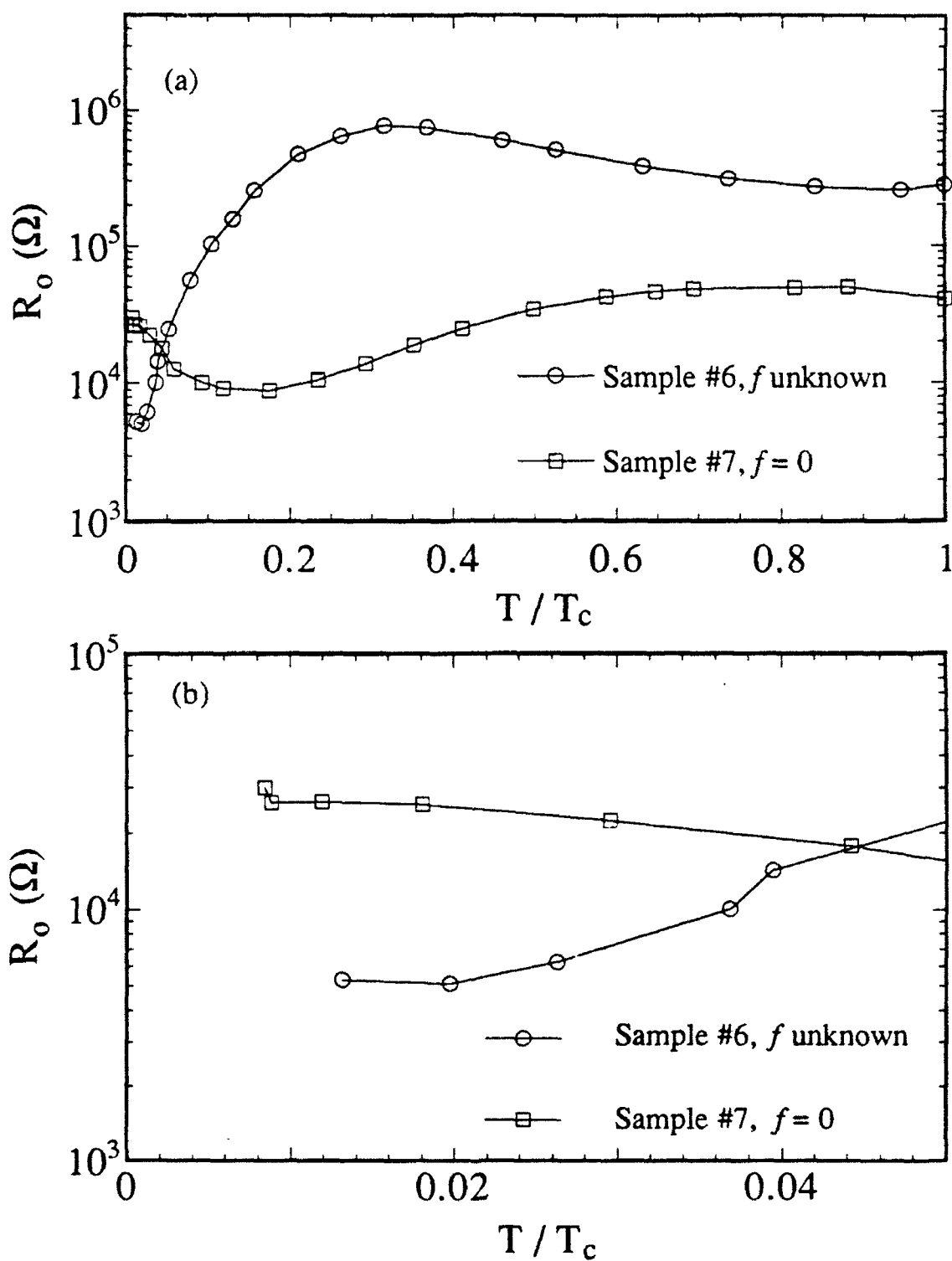


Figure 5-8.

The low-voltage resistance R_o for samples #6 and #7 vs. T/T_c . Curve (a) shows the data for the entire temperature range ($T < T_c$), while curve (b) concentrates on the low-temperature region.

CHAPTER SIX

MEASUREMENTS AND DISCUSSION ON CHARGING ARRAYS

In this chapter we describe arrays where the charging energy E_c dominates the Josephson energy E_J . As discussed in Chapter 1, these arrays show a Coulomb blockade at low temperatures which results in *insulating* behavior around zero bias. We study the blockades of three arrays, with E_c/E_J ranging from roughly 5 to 35, in both the superconducting and normal states.¹

This chapter is divided into three sections. Section 6.1 describes the general aspects of the I-V curves, including the dependence on applied magnetic field. Section 6.2 goes into the determination of the array parameters, most notably the junction capacitance C and the island capacitance-to-ground C_o . In Sec. 6.3 we detail the specific results of the measurements.

6.1 General Results

Before we begin this section on the general results of our data, it is important to review our discussion of the nature of current flow through an array. As described in the introduction, and again in more detail in Chapter 2, an excess charge in an array with large E_c/E_J polarizes neighboring islands. The charge and the resulting polarizations are referred to as a soliton. For current to flow, (1) solitons must be able to pass through the array from one electrode to the other, or (2) soliton-antisoliton pairs must form within the

¹For the charging arrays we find it more transparent to discuss E_c/E_J rather than its inverse, which is used in the previous chapters.

array, then dissociate, with the solitons traveling to one electrode and the antisolitons traveling to the other. The physics of the two processes is essentially the same: in (1), a soliton entering the array from an electrode first forms a pair with its image antisoliton, from which it must then dissociate to be able to move through the array.

At $T = 0$, no thermally activated pairs are present. For current to flow, a strong enough electric field must be applied to create pairs out of the "vacuum" and then pull them apart. This will happen at the edge first as the electric field, given an applied voltage across the array, is strongest there. [This is due to the presence of the island capacitance-to-ground C_o from the following argument. Away from the edge electrodes, the capacitive coupling to ground acts to pull the island voltages to the ground voltage. Therefore, the electric field due to an applied bias voltage is screened to the edges. Tinkham (private communication) calculates that the form of this screening is exponential; $V_i \propto V_{bias} \exp(-x_i \lambda_o)$, where V_i is the voltage of the i^{th} island, V_{bias} is the applied bias voltage, x_i is the distance of the i^{th} island from an edge electrode (in units of the array lattice spacing), and λ_o^{-1} is a characteristic distance, $\lambda_o^{-1} = \sqrt{C/C_o}$ for $C \gg C_o$]. Thus, in considering the threshold voltage V_t , the minimum voltage required for this process to happen and for current to flow, we find it more physical to discuss solitons entering the array from an electrode as in (1). For voltages below V_t , called the Coulomb blockade region, no current flows.

At higher temperatures, activated pairs will be present, both at the edges and within the array. In discussing these thermal activation measurements, we find it helpful to use the general concept of pair formation and dissociation, as in (2), whether it happens at an edge or not.¹

We study three arrays in this chapter, all with Al-AlOx junctions and with dimensions 50 by 70 unit cells. The array parameters are given in Table 6-1. Figure 6-1 shows I-V

¹Currently it is unclear as to whether thermally activated pair formation and/or dissociation primarily happen at the edges or within the array.

Table 6-1. Parameters for samples #8 - #10. As discussed in Sec. 6.2, C and E_c are determined from the offset voltage using local rules. R_n and C are per junction.

Sample #	junction area (μm^2)	R_n ($\text{k}\Omega$)	C (fF)	E_c/k_B (K)	E_J/k_B (K)	E_c/E_J
8	0.004 ± 0.001	24	0.47 ± 0.02	2.0 ± 0.1	0.38	5.3 ± 0.3
9	0.004 ± 0.001	38	0.43 ± 0.02	2.2 ± 0.1	0.24	9.2 ± 0.4
10	0.003 ± 0.001	126	0.38 ± 0.02	2.5 ± 0.1	0.072	35 ± 2

curves for sample #10 in (a) the normal state¹ and (b) the superconducting state. In the normal state, we see the Coulomb blockade region; current does not flow at low voltages as described above. In the superconducting state (b), we see the *superconducting gap*,² which masks the smaller Coulomb blockade region. The Coulomb blockade region is visible only at an expanded scale. We find no evidence of a critical current, which differentiates #10 from #7, a transitional array, where we do see slight evidence of a critical current, despite the sample's insulating behavior around zero bias. (See Fig. 5-1.) Expanding the scale of Figs. 6-1(a) and (b), we can more directly observe the Coulomb blockade regions. Figure 6-2 shows these regions in the superconducting and normal states for sample #10 at a temperature of 15 mK. [In the superconducting state, this blockade feature is contained entirely within the superconducting gap, seen in Fig. 6-1(b). The horizontal scale of Fig. 6-2 is expanded by roughly a factor of 1000 over that of Fig. 6-1(b) in order to see this feature.] Around zero bias and at low temperatures, we measure resistances greater than $10 \text{ G}\Omega$.³ At the threshold voltage V_t , we see a sharp onset of current.

¹The superconductivity has been suppressed to zero with a large magnetic field, typically greater than 2 Tesla.

²The superconducting gap extends from $-2M\Delta/e$ to $2M\Delta/e$ for a full width of magnitude $4M\Delta/e$, where M is the number of junctions through which current must travel, and is equal to 70 for the three arrays.

³Current noise in the measuring resistor (current bias set-up) or the current preamplifier (voltage bias set-up) limits our ability to determine resistances above this value.

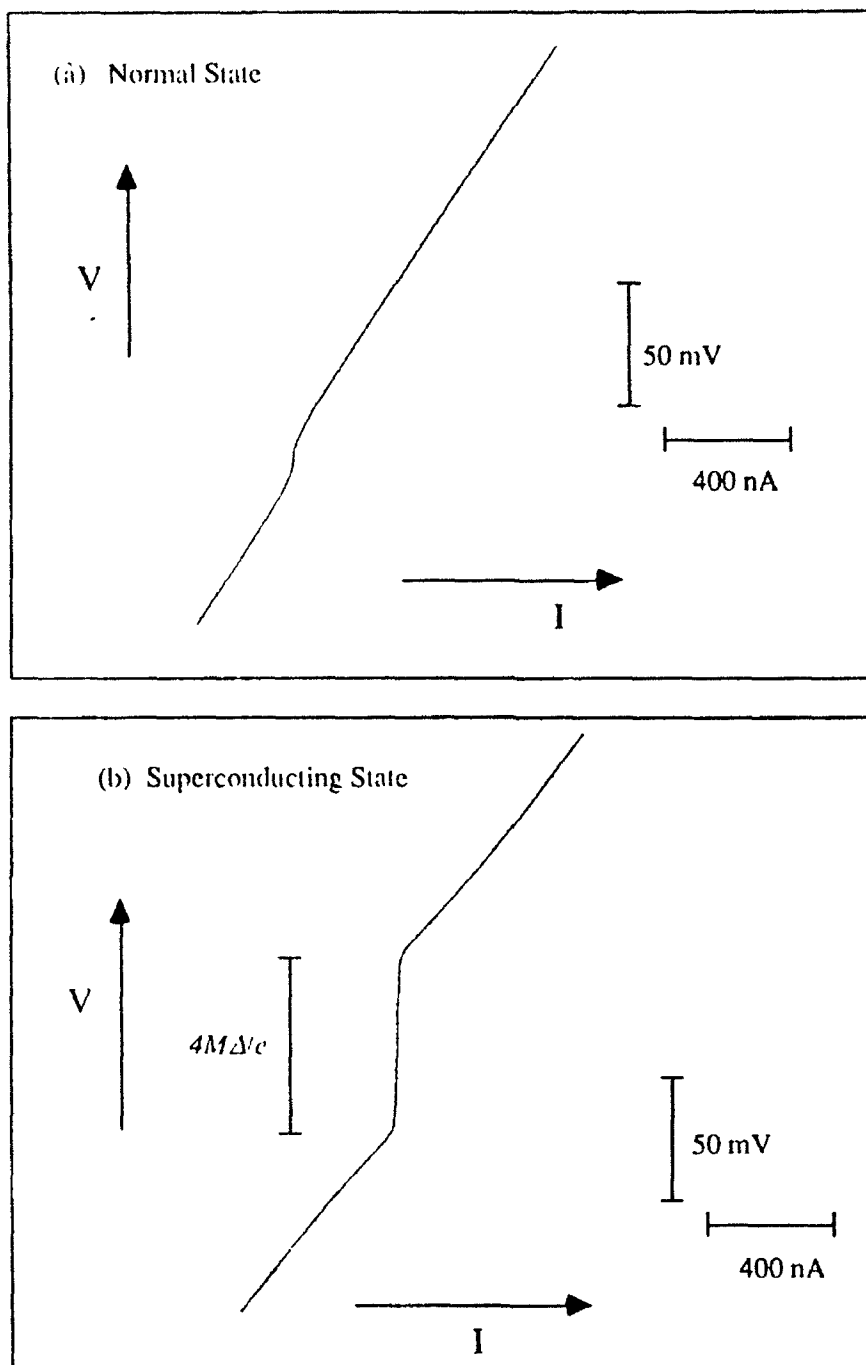


Figure 6-1.

I-V curves for sample #10 at a temperature of 15 mK in (a) the normal state and (b) the superconducting state. In the normal state (a), we see the Coulomb blockade region. In the superconducting state (b), this blockade region is masked by the superconducting gap (of order $4M\Delta/e$).

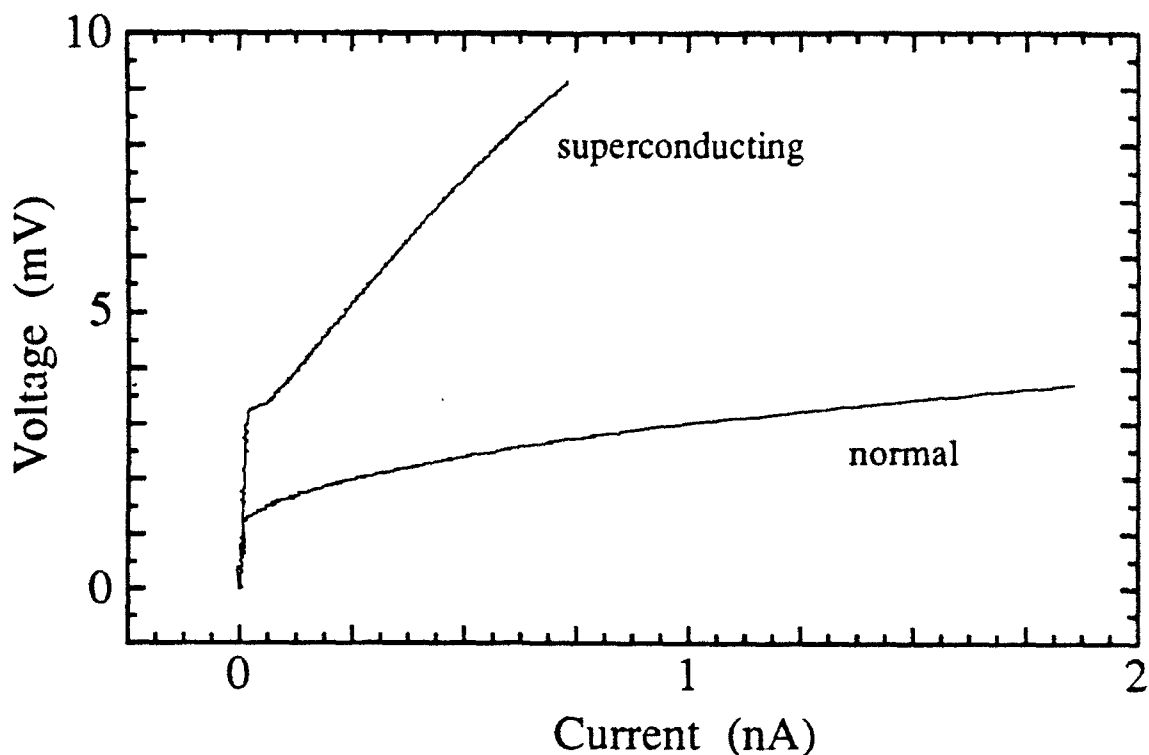


Figure 6-2.

Blow up of the center region of the I-V curves shown in Fig. 6-1 (sample #10 at 15 mK). Here we clearly see the Coulomb blockade in both the superconducting and normal states.

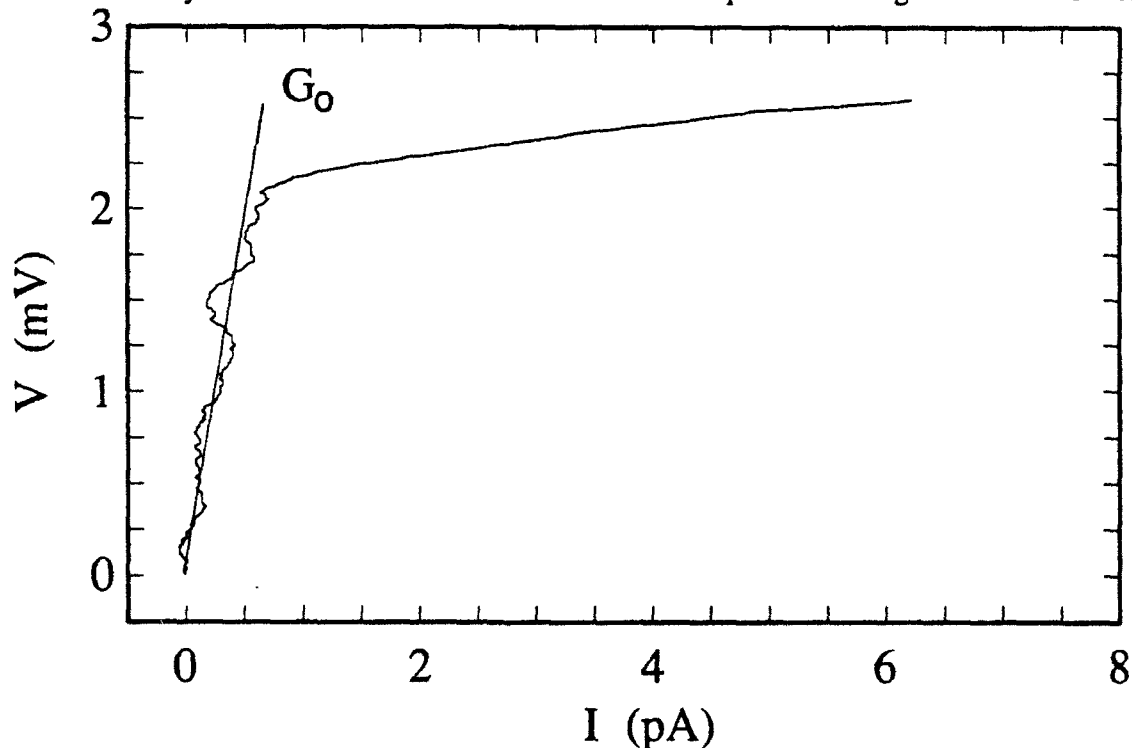


Figure 6-3.

Coulomb blockade for sample #10 in the superconducting state at $T = 300$ mK. Here we see that the current within the blockade region is roughly linear in voltage, allowing us to define a low-voltage conductance G_0 . The fluctuations on the order of 0.5 pA at low currents are non-reproducible, and most likely due to current noise.

Table 6-2. Dependence of V_t on frustration.

Sample #	E_C/E_J	$V_t, f = 0$ (mV)	$V_t, f = 1/2$ (mV)	ΔV_t (mV)	% change in V_t
7	3.1	0.01	1.0	1.0	10000
8	5.3	0.4	0.6	0.2	50
9	9.2	1.7	1.9	0.2	12
10	35	3.2	3.3	0.1	3

At higher temperatures, current may flow for $V < V_t$. Figure 6-3 shows the Coulomb blockade region for sample #10 in the superconducting state at a temperature of $T = 300$ mK. The current within the blockade region appears to be linear in voltage, allowing us to define a low-voltage conductance G_o . This is similar to our definition of R_o ; throughout this thesis we let $G_o = 1/R_o$.

We briefly mention the effect of a magnetic field on these arrays. Though we are not aware of any theory which predicts the effects of magnetic field on an array with large E_C/E_J , these data provide an *indirect* measure of the importance of superconducting coupling, and may serve as an intuitive aid. As we learned with sample #7 in the previous chapter, frustration affects the width of the Coulomb blockade: V_t is at a minimum for $f = 0$ and a maximum for $f = 1/2$.¹ Table 6-2 gives this change in V_t . The most dramatic shift is for #7, a transitional array, where the blockade width at $f = 1/2$ is roughly a factor of 100 larger than the value at $f = 0$. For #10, however, with $E_C/E_J = 35$, the increase is just 3%. For these higher values of E_C/E_J , the superconducting coupling appears only to be a weak effect. Unless explicitly stated otherwise, all of the measurements in this chapter are given for $f = 0$.

¹The data given in Chapter 5 only show that V_t is larger at $f = 1/2$ than at $f = 0$. Other data, not given, show that V_t is *maximum* at $f = 1/2$.

6.2 Determination of Parameters

Three important parameters in these arrays are the junction normal resistance R_n , the junction capacitance C , the island capacitance-to-ground C_o .^{1,2} The determination of R_n is the same as for the previous samples; R_n equals the differential resistance at high temperatures or voltages. However, we use a different method of determining C , which we describe in Sec. 6.2.1. In Sec. 6.2.2 we discuss the method of determining C_o .

6.2.1 Determination of C

At higher voltages, the I-V curves in the normal state, such as that in Fig. 6-1(a), approach a linear asymptote which extrapolates back to a finite offset voltage V_{off} at zero current. For a single junction, the relationship between V_{off} and C is thought to be unambiguous³ [Iansiti (1988)],

$$V_{off} = \frac{e}{2C} \quad \text{single junction} \quad (6.1)$$

However, in 1D and 2D arrays, the relationship between V_{off} and C is thought to depend on the junction's electromagnetic environment. If the system acts under so-called *local* rules (the electron tunneling rate depends *solely* on the change in energy of the junction across which it tunnels), Geigenmüller and Schön (1989) give the relationships as

¹What we measure will be roughly the *average* junction R_n and C , as discussed in Chapter 4. However, here we will not use special notation to denote these average values because (1) our measurements do not show any direct evidence of large inhomogeneities within the arrays, and (2) any indirect evidence for a spread in junction parameters cannot be separated from a new source of inhomogeneity, the random offset charges on each island (which we discuss later in the chapter). At the level of our discussion, it is easiest to treat all the junctions as uniform and associate any inhomogeneity with the offset charges.

²We did not discuss C_o in regards to the arrays in which E_c is less than or on the order of E_J . For the charging arrays, the effects of C_o are much weaker than those of C . In the superconducting arrays, the effects of C are *already small*, so that the effects of C_o are likely to be negligible.

³Single junctions do not serve as the best example for this effect because the blockade is usually washed out by strong electromagnetic coupling to the environment. To measure this offset voltage in a single junction, one must typically connect the junction to the rest of the circuit through highly resistive, on-chip leads. See Cleland, *et al.* (1992).

$$V_{off} = \frac{Me}{2C} \quad \text{1D and 2D arrays, local rules} \quad (6.2)$$

where M is the number of junctions through which current must travel to reach one electrode from the other (= 70 for the three arrays). Under *global* rules (the tunneling rate depends on the change in energy of all the junctions in the array), Bakhvalov, *et al.* (1991), give the relationships as

$$V_{off} \approx \frac{Me}{2C} \quad \text{1D array, global rules} \quad (6.3a)$$

$$V_{off} \approx \frac{Me}{4C} \quad \text{2D array, global rules} \quad (6.3b)$$

The factor of two difference between the 2D results [Eqns. (6.2) and (6.3b)] may be thought of as replacing C in Eqn. (6.2), the local result, by an effective capacitance C_{eff} which takes into account all of the shunting capacitances in two dimensions. Based on arguments of superposition for an infinite square array,¹ $C_{eff} = 2C$ (of which $\sim 5/3 C$ comes from the junction and its nearest neighbors); hence the global result for the 2D array. In the 1D global case, there are no shunting capacitances, so $C_{eff} = C$ and we recover the local result.²

In an attempt to choose between the two possible values of C [from a measured V_{off} using Eqn. (6.2) or Eqn. (6.3b)], we compare it with that determined from the junction area. For sample #10, the measured offset of $V_{off} = 15$ mV gives $C \approx 0.37$ fF using local rules, or ≈ 0.19 fF using global rules. The nominal junction area determined using a scanning electron microscope is $0.004 \pm 0.001 \mu\text{m}^2$. Thus, our data imply a specific capacitance of $93 \text{ fF}/\mu\text{m}^2$

¹The classic problem involves an infinite square array of resistors with identical resistance r . Using superposition of currents, one can show that the resistance between adjacent lattice points is $r/2$. The argument for capacitors is analogous, and leads to a capacitance $2C$.

²Subtle effects involving C_o make the global results only approximate; hence the " \approx " signs. For more information on 1D arrays see Delsing (1992) and Kuzmin, *et al.* (1989).

Table 6-3. Data on arrays measured by Geerligs (1990) (all with Al-AlO_x junctions and with dimensions of 190 by 60 unit cells). Capacitances are determined from offset voltages, using Eqn. (6.2) (local rules).

sample	junction area (μm^2)	R_n (k Ω)	E_c/E_J	specific cap. (fF/ μm^2)
G	0.04	129	5.6	58
H	0.01	15.3	1.6	100
I1	0.01	14.1	1.3	110
J	0.01	9.7	0.82	120
I2	0.02	8.0	0.29	140

using local rules, or 46 fF/ μm^2 using global rules. For comparison, Geerligs, *et al.* (1989) quote 110 fF/ μm^2 , while the Delsing, *et al.* (1992) quote 45 fF/ μm^2 . The latter value is based on two measurements: (1) measurements of Fiske steps on large Nb-Al-AlO_x-Al-Nb junctions by Lichtenberger, *et al.* (1989), which give 45 ± 5 fF/ μm^2 , and (2) measurements of offset voltages and areas on two-junction systems by Tuominen, *et al.* (1992), using global rules,¹ on junctions nominally identical to ours, which also appear to give this value. The Geerligs value is also based on measurements of offset voltages and areas, determining C from Eqn. (6.2), using local rules. They average a large number (> 10) of samples, both single junctions and arrays, with junctions similar to ours. Table 6-3 gives the specific capacitances for the five 2D arrays reported by Geerligs (1990). Here we see that Geerligs measured a wide spread in specific capacitances for arrays, ranging from 58 fF/ μm^2 to 140 fF/ μm^2 . The value for sample G is low in part due to the thicker oxide layer required to have such a large normal resistance despite the larger junction area.² There does appear to be a correlation between the specific capacitance and both E_c/E_J and R_n . The reason for this is

¹ In this system, due to the small number of junctions it is believed that global rules should apply. See Averin and Likharev (1991).

² We can calculate the oxide layer thickness using Eqn. (4.1) [from Knorr and Leslie (1973)]. We get for sample H, $t \approx 11.5$ Å, while for sample G, $t \approx 15$ Å. This increase in thickness from H to G results in a decrease in specific capacitance of $\approx 23\%$, about half the measured decrease (from Table 6-3) of 42%.

unclear at this time.

Choosing global or local rules appears to depend on which value of specific capacitance we choose. A further puzzle arises from comparison with the data of Delsing, *et al.* on arrays similar to ours, in which a V_{off} per junction of 350 μV was observed, compared to our value of 214 μV for sample #10, while the nominal area of their junctions was 0.005 μm^2 compared to our nominal area of 0.004 μm^2 . Thus, regardless of the interpretation rule, their V_{off} implies a substantially smaller capacitance for a junction of equal or larger area. Delsing, *et al.* find good consistency of their data with the *local* rule using the 45 fF/ μm^2 specific capacitance. Our data also support that rule, but only if we presume that our effective junction areas are substantially larger than the nominal values because of edge contributions, or else accept the larger Geerligs value for the specific capacitance, presuming we have more geometry-dependent stray capacitance than in the Delsing work.

This issue remains unresolved, but we proceed on the basis that the appropriate C is determined by the local rules case, $V_{off} = Me/2C$. We choose this for two reasons: (1) to remain consistent with the Delft¹ and Göteborg² groups, who use local rules, and (2) as we measure V_{off} in a high-current regime, the use of local rules is plausible from the following argument. Consider a single tunneling event; under global rules, the electron tunneling rate depends on the change in energy of the whole system. However, if there is a large current passing through the array, this change in energy may rapidly fluctuate because of tunneling transitions of *other* electrons. The single electron then would not “know” how its tunneling would effect the energy of the whole system, and thus global rules would appear inappropriate.

¹Mooij, *et al.* (1990).

²Delsing, *et al.* (1992).

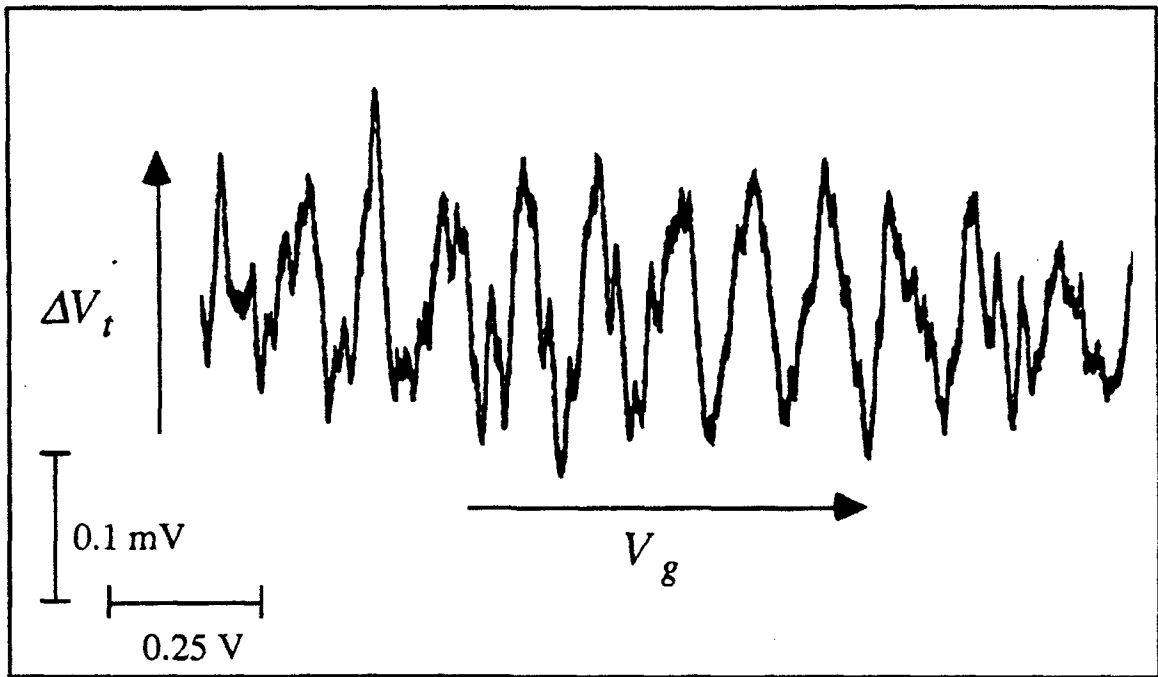


Figure 6-4.

Change in V_t vs. V_g , the voltage between the array and the ground plane, for sample #10 at 15 mK in the normal state. Here we see the periodic oscillations whose period is a measure of the capacitance to ground C_o .

6.2.2 Determination of C_o

Finally, we determine C_o by applying a voltage V_g between the array and the underlying ground plane. Upon sweeping this voltage, Mooij, *et al.* (1990) predict that the threshold voltage V_t should oscillate with a period of e/C_o . For sample #10, we measured these oscillations in the normal state, as seen in Fig. 6-4. V_t oscillates by $\pm 13\%$ (± 0.1 mV) about its mean value, with a period of 0.12 V, corresponding to $C_o = 1.3$ aF. Sample #9 has oscillations of $\pm 18\%$ (± 0.1 mV), also with a period of 0.12 V. For sample #8, we did not measure the oscillation period, but only measured the change in V_t : $\pm 16\%$ (± 0.08 mV). In the superconducting state for sample #10, we also measure a periodic oscillation of V_t with the same period 0.12 V. However, the oscillations are much

smaller, about $\pm 0.1\%$ (± 0.003 mV). We are unsure as to why the magnitude of this effect is so much smaller in the superconducting state than in the normal state.

6.3 Discussion of Results

We break up this discussion into three sections. In Sec. 6.3.1 we compare the measured threshold voltage with that predicted by Bakhvalov, *et al.* (1991). Sections 6.3.2 and 6.3.3 look at the experimental and theoretical aspects of thermal activation in these arrays.

6.3.1 Threshold Voltage V_t

At low temperatures, little or no current flows below some threshold voltage V_t .¹ As discussed at the start of Sec. 6.1, V_t is thought to be a measure of an edge barrier to soliton injection. Bakhvalov, *et al.* (1991) determine an analytical expression for V_t in the normal state

$$V_t \equiv \left(1 - \frac{2}{\pi}\right) \frac{e}{2C} \sqrt{\frac{C}{C_o}} \quad (6.4)$$

This equation can in some sense be thought of as three factors: (1) $e/2C$, the voltage required to move an electron across a single junction, (2) $\sqrt{C/C_o}$, which represents the screening of electric fields within the array, and (3) a numerical prefactor which takes into account the 2D nature of the arrays.

In the superconducting state, we are not aware of any theory in the literature which predicts V_t . A simple idea put forward by M. Tinkham (private communication), is that the system needs an additional applied voltage to break apart Cooper pairs. Following

¹For additional experimental data, see Chen, *et al.* (1992).

Table 6-4. Theoretical and experimental values of the threshold voltage V_t .

Sample #	R_n (k Ω)	C (fF)	E_c/E_J	V_t , normal state (mV)		V_t , s.c. state (mV)	
				theory	exp.	theory	exp.
8	24	0.47	5.3	1.2	0.5 \pm 0.2	6.1	0.4 \pm 0.1
9	38	0.43	9.2	1.2	0.6 \pm 0.1	5.9	1.7 \pm 0.2
10	126	0.38	35	1.3	1.0 \pm 0.1	5.7	3.2 \pm 0.2

the arguments of Bakhvalov, *et al.*, Tinkham estimates this additional voltage to be of the order of $(\Delta/e)\sqrt{C/C_0}$.¹ The expected V_t in the superconducting state is then the sum of this voltage plus the threshold voltage in the normal state.

We give these values of V_t in Table 6-4 for samples #8 - #10, along with the experimental values.² In the normal state, we find the theoretical values to exceed the measured values by as much as a factor of 2.4. In addition, the predicted values are all nearly equal, while the measured ones show more variation.³ In the superconducting state, the predicted values of V_t again exceed the measured ones [Note that here the theoretical values of V_t fall from sample #8 through #10 due to the change in C in the term $(\Delta/e)\sqrt{C/C_0}$]. This qualitative discrepancy in both the superconducting and normal states may arise because the theoretical predictions do not take into account random inhomogeneities, such as offset charges associated with each island (thought to be due to capacitive coupling between charged inhomogeneities in the substrate or insulating barrier). In general, we expect that inhomogeneities would lower V_t , since a locally

¹ This voltage is an order-of-magnitude estimate of that required to pull apart a Cooper pair at the edge of an array. In this simple argument, the separation of a Cooper pair is unrelated to the 2D nature of the array, and so we do not include the $(1-2/\pi)$ prefactor.

² We give the maximum values of the measured V_t , as V_t oscillates upon sweeping the voltage between the array and the ground plane. For sample #8 in the normal state, due to an oversight we did not get as accurate a reading of V_t as we did for the other two samples. This may account for the fact that the V_t in the normal state appears larger than that in the superconducting state.

³ Empirically, in the normal state V_t appears to scale more closely with the junction normal state resistance than with the junction capacitance, but the reason for this correlation is not clear at this time. The effect seems too large to be accounted for by the renormalization of the capacitance by the effect of the conductance onset above a gap, although this mechanism varies in the correct way with R_n .

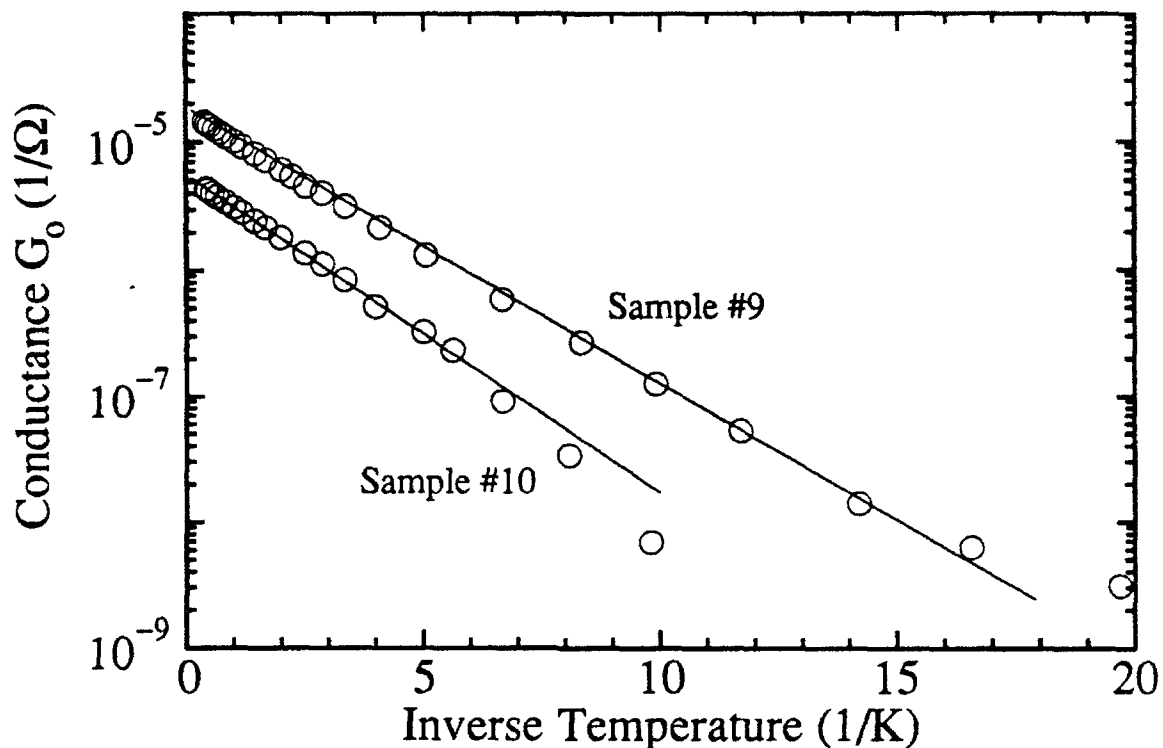


Figure 6-5.

Measured differential conductance within the Coulomb blockade region vs. inverse temperature in the normal state. The solid lines are given by Eqn. (6.5). The lower temperature limit is set by our ability to measure small conductances.

weaker barrier would allow soliton entry at a lower voltage. Also, it may be significant that the agreement in the superconducting case is best when E_C/E_J is largest, since the theoretical estimate ignores E_J completely.

6.3.2 Thermal Activation--Measurements

All the data presented above are for temperatures close to absolute zero, about 15 mK, where the conductance G_0 within the gap is immeasurably small. At temperatures above ~50 mK in the normal state and ~300 mK in the superconducting state, however, we do measure a finite conductance. Making an Arrhenius plot of the logarithm of G_0 in the

normal state vs. the inverse temperature (Fig. 6-5), the data fall on straight lines (sample #8 accidentally cracked before these measurements were made on it); this suggests that the current arises from a thermal-activation process. The straight lines in Fig. 6-5 are given by the simple Arrhenius form

$$G = \left(\frac{N}{M} \right) \frac{1}{R_n} \exp\{-U / k_B T\} \quad (6.5)$$

where we measure the activation energy U (the slope of the straight lines) to be 0.50 K and 0.58 K for samples #9 and #10 respectively. As E_c/k_B for these samples has been inferred from V_{off} measurements to be 2.2 and 2.5 K respectively, we see that the activation barrier for both samples is $U = 0.23 \pm 0.02 E_c$.

These simple results are quite distinct from the temperature dependence

$$G = \left(\frac{N}{M} \right) \frac{K}{R_n} \exp\left\{-2b[(T / T_{KTB}) - 1]^{-1/2}\right\} \quad (6.6)$$

predicted (for $T > T_{KBT}$) for the Kosterlitz-Thouless-Berezinskii (KTB) transition, which is expected theoretically if the attractive interaction between solitons dominates the physics. Despite three adjustable parameters, K , b , and T_{KTB} , Eqn. (6.6) gives a much poorer fit to our data than Eqn. (6.5).

We now compare these data with data taken on arrays by two other groups. Figure 6-6 shows an Arrhenius plot for data from Mooij, *et al.* (1990), Delsing, *et al.* (1992), and our samples #9 and #10. (The vertical axis has been scaled so that the slope of the lines gives the activation energy in units of E_c/k_B .) The curves are parallel, which indicates that all four samples have roughly the same activation energy (scaled to E_c/k_B).¹ Specifically,

¹ The data from the two other groups and sample #9 appear to have a slight upward curvature. We determine the slope by a simple "best fit" by eye, and reflect these curvatures in the quoted uncertainties.

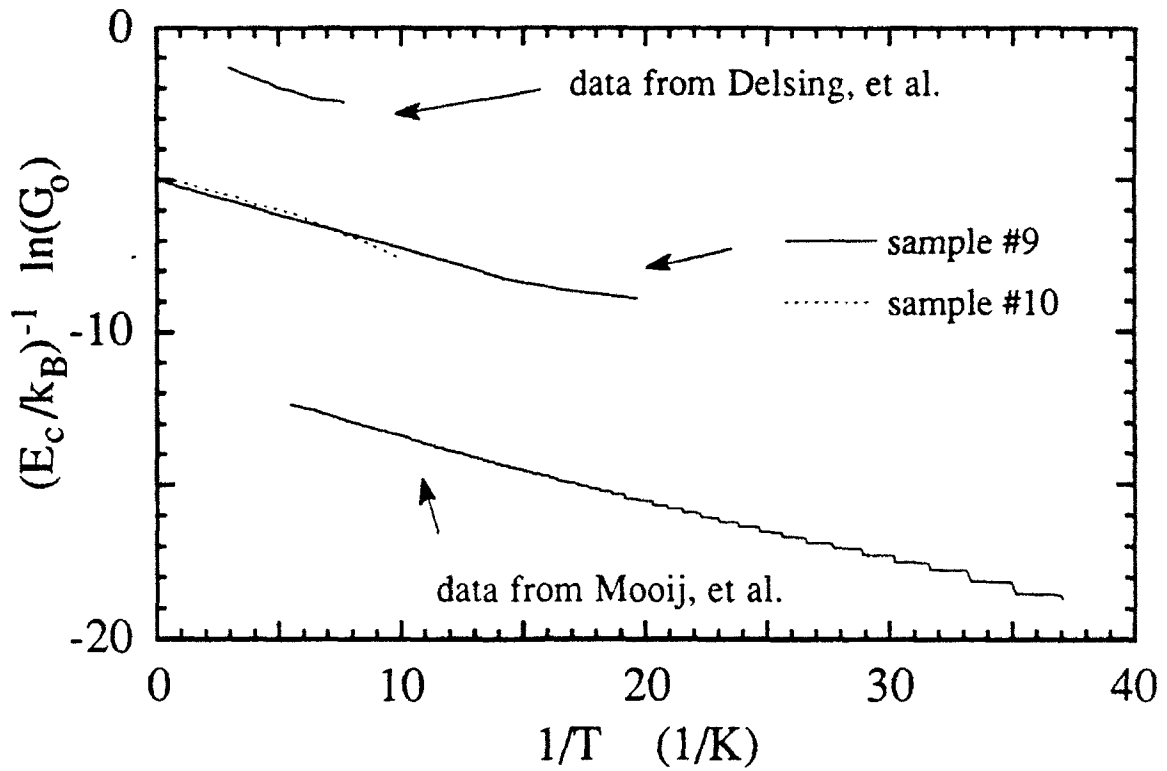


Figure 6-6.

Logarithm of the differential conductance within the Coulomb blockade region vs. inverse temperature (the vertical axis is scaled to E_c/k_B) for arrays from Mooij, *et al.* (1990), Delsing, *et al.* (1991), and our samples #9 and #10, in the normal state.

the data from Mooij, *et al.*, on an array with $E_c/k_B \approx 1\text{K}$, show an activation energy of $U = 0.24 \pm 0.02 E_c$, and the data from Delsing, *et al.*, on an array with $E_c/k_B \approx 4\text{K}$, show $U = 0.27 \pm 0.03 E_c$.

Mooij, *et al.* discussed their array data in terms of a rounded KTB transition, though their experimental data are fitted better by an Arrhenius form. The same is true of the data of Delsing, *et al.*, who stated explicitly that their experimental data did not fit the KTB form, but did not note the Arrhenius fit. This fit and its significance are two of the principal points of this chapter.

In the superconducting state, we again plot the conductance in an Arrhenius fashion

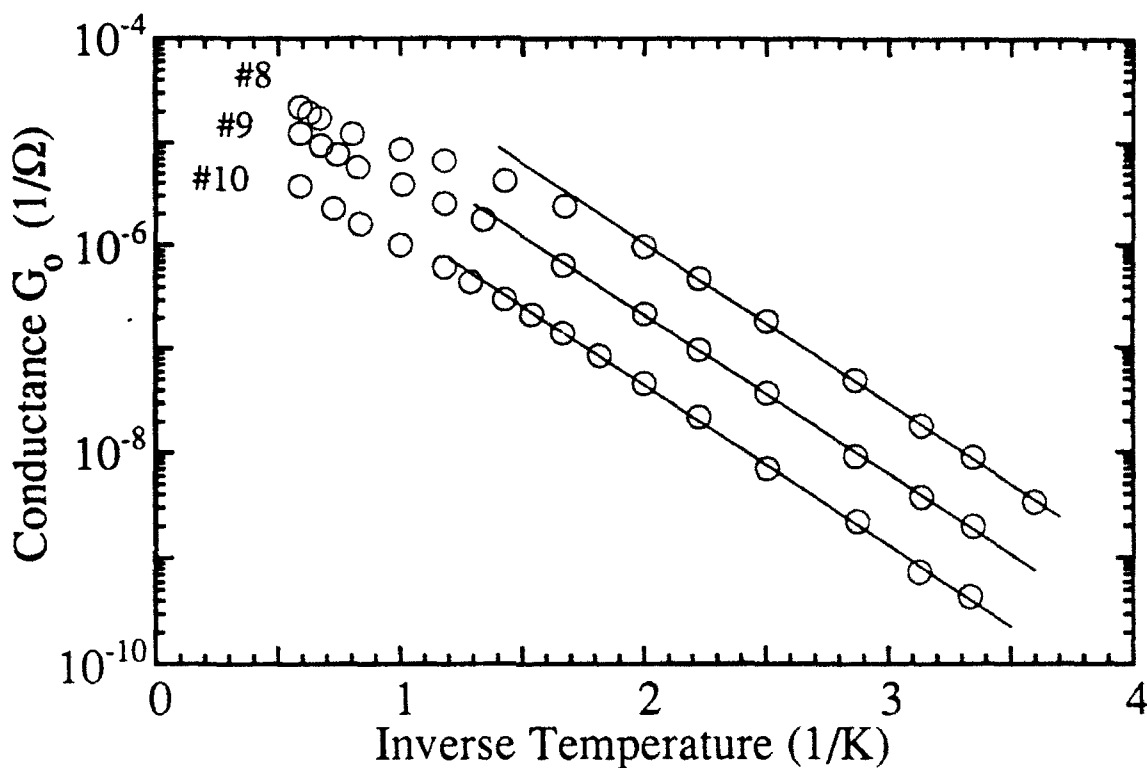


Figure 6-7.

Measured differential conductance within the Coulomb blockade region vs. inverse temperature in the superconducting state. Solid lines are fits to the linear portions of the data.

(Fig. 6-7). Far enough below the superconducting transition temperature of about 1.7 K, the data again fall on straight lines. The solid lines in Fig. 6-7 are proportional to $\exp\{-U'/k_B T\}$, where U' represents the activation energy in the superconducting state.¹ For samples #8, #9, and #10, the slopes are given by $U' = 3.6, 3.5$, and 3.5 K respectively. These values appear to be the sum of two terms; the superconducting energy gap ($\Delta/k_B = 1.76T_c \approx 3.0 \pm 0.1$ K) and the activation barrier for single electrons or quasiparticles, as measured in the normal state (0.50 K and 0.58 K for samples #9 and #10 respectively). This suggests that enough thermal energy must be present to create

¹Unlike the normal-state case [see Eqn. (6.5)], there does not exist a simple prefactor to the exponential term which fits all three curves.

quasiparticles, which then require an extra $0.23 E_c$ of energy, as in the normal state, to separate the charges onto different islands so that current can flow.

6.3.3 Thermal Activation--Theory

At the beginning of Sec. 6.1, we discussed the nature of currents within these arrays: a current flows when soliton-antisoliton pairs form and dissociate, with the solitons moving to one electrode and antisolitons to the other under the influence of a bias voltage.¹ Pair formation and dissociation may occur either within the array or at an edge (where one in the pair is treated as an image charge). The activation energy then is a measure of the barrier pairs must overcome to form and dissociate.

From the following argument we find that the measured activation energy should closely match the energy to form a soliton-antisoliton pair of separation one lattice spacing, the core energy. The work required to move an electron across a junction connecting two otherwise *isolated* islands is just $E_c = e^2/2C$. However, if the islands are part of an array, then one must replace C by an effective capacitance $C_{eff} = 2C$, as discussed previously.² Hence the core energy of a pair is $0.5 E_c$. What is measured as an activation energy, however, will be half of this value as excitations can only be created in *pairs* (similar to a superconductor, where it takes energy 2Δ to create a pair of quasiparticles, yet activation data give a measurement of the activation energy to be Δ).³ The measured activation energy should then be $0.25 E_c$, which closely matches our measured value of $0.23 E_c$.

This interpretation neglects the predicted logarithmic interaction between the soliton and antisoliton (or between the soliton and an edge), as if the interaction were screened,

¹ A pair forms, in an otherwise neutral array, by one electron tunneling across a junction. This leaves an extra electron (soliton) on the island to which the electron tunneled, and a hole (antisoliton) on the island from which the electron tunneled.

² See footnote 1 on page 115.

³ See Tinkham (1975), p. 8.

even at short ranges. D. S. Fisher (private communication) argues that this is due to the presence of fringing fields (see Sec. 2.4.2), so that the interaction is short range and *not* logarithmic. In addition, the existence of the random, offset charges might play a role in this screening, although they would also alter the core energy of a soliton-antisoliton pair depending on the pair's location. Another possibility is if the logarithmic interaction is the correct description, its cutoff length, nominally $\lambda_o^{-1} = \sqrt{C/C_o}$ (≈ 17 lattice spacings for sample #10), may be significantly decreased by the screening effect of other solitons. Since the density of thermal solitons is $\sim \exp(-U/k_B T)$, this screening mechanism is temperature-dependent, and would be expected to be important for all $T \geq 100$ mK, *i.e.*, over most of the experimental range. The above argument which predicts $0.25 E_c$ also neglects the influence of C_o . However, as this capacitance to ground should "weaken" the full charge of the soliton, it may account for our measured value being slightly smaller than that predicted.

Given the simple nature of our model and also the uncertainty of a factor of two in the definition of C (global vs. local rules), the close numerical agreement of this interpretation with the data may be somewhat fortuitous. Nonetheless, it seems very significant that the activation energy (normalized to E_c) measured by us matches within 10% with the values we deduce from the data of the Göteborg and Delft groups taken on arrays having charging energies E_c/k_B ranging from 1K to 4K (using the same method of determining C).

In future work, a more satisfactory explanation may be found by numerically computing the activation barrier in the manner of J. Martinis (private communication). He begins by showing that, using Eqns. (2.33) and (2.34), in a simple fashion one can calculate the *total capacitive energy* E_{array} stored in an array for any given soliton configuration (any number, arrangement, and mixture of solitons and antisolitons).¹ As

¹ As this technique involves the inversion of an $N \times M$ by $N \times M$ matrix, it is somewhat limited in studying large arrays.

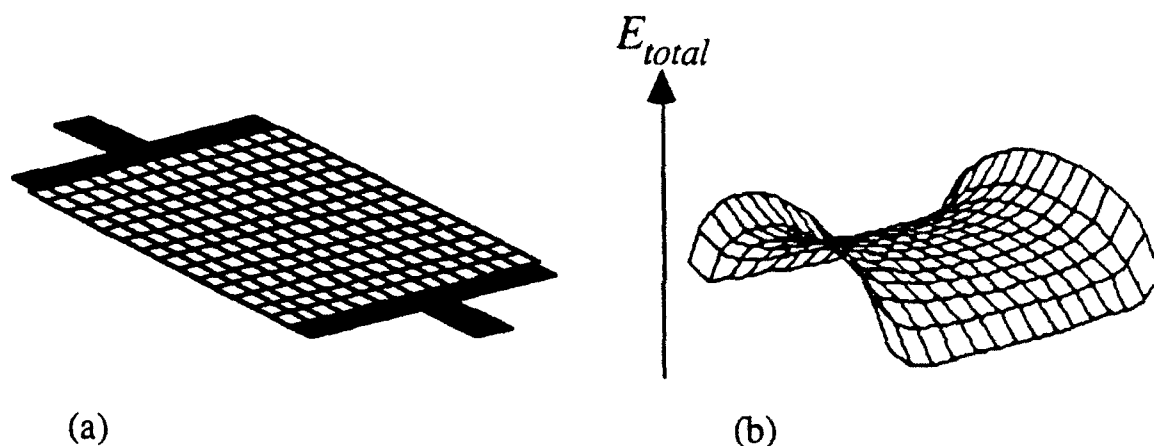


Figure 6-8.

This figure shows (a) a schematic drawing of a 15 by 15 array with the location of the electrodes and (b), for a *single* soliton present, the total capacitive energy E_{total} stored in the array as a function of the soliton's position [J. Martinis (private communication)]. Here we see the saddle-like potential caused by the soliton's attraction to the edge electrodes and repulsion from free edges.

an example of how one might use this to get an activation barrier, he determines E_{array} for a single soliton in an array as a function of the soliton's position. Figure 6-8 shows this for a 15 by 15 array. This saddle-like potential graphically represents the soliton's attraction to edge electrodes and repulsion from free edges, as already discussed. This technique may prove valuable as it is possible to calculate pair energies, as well as include effects such as random offset charges, island capacitances-to-ground, and capacitances between islands which are not nearest neighbors. These calculations may serve as a useful tool in investigating the impact of these effects. Unfortunately, it may be difficult to use these electrostatic energy calculations to include screening effects, which we estimate to be important over most of the experimental temperature range, as they are dynamical in nature.

All of the above discussion focuses on the normal state. In the superconducting state, we measure activation energies of $U'/k_B = 3.6K$, $3.5K$, and $3.5K$ for samples #8, #9, and

#10 respectively. As already discussed, these values of U' appear to be the sum of Δ , the superconducting energy gap, and $0.23 E_c$, the activation barrier for single electrons or quasiparticles, as measured in the normal state (suggesting that enough thermal energy must be present to create quasiparticles, which then require an extra $0.23 E_c$ of energy, as in the normal state, to separate the charges onto different islands so that current can flow). These measurements match a theoretical calculation done by Simánek (1982)¹ which predicts an activation energy in the superconducting state to be the superconducting energy gap *plus* one half the charging energy required for an electron to tunnel across a junction in an otherwise neutral array. Using the simple model described above, this gives $\Delta + 0.25E_c$, almost identical to our measured result.

¹ See Simánek (1982), Eqn. (3.8).

CHAPTER SEVEN

MICROWAVE IRRADIATION OF CHARGING ARRAYS

In this chapter we look at the influence of ac radiation, from 10 MHz to 20 GHz, on the I-V characteristics of the charging arrays. Performing these measurements on sample #9 at milliKelvin temperatures, we find that the radiation reduces the threshold voltage and shifts the I-V curves to lower voltages, with the amount of shift roughly proportional to the amplitude of the ac signal. These results are not explained by three known effects found when applying high frequencies to junctions (measured in 1D arrays or other junction systems); simple averaging, single-electron tunneling (SET) oscillations, and photon-assisted tunneling (PAT). As we do not have an alternative explanation for the behavior of this data at this time, the results in this chapter are left open to interpretation.

In Sec. 7.1, we look at the I-V characteristics of sample #9 with ac radiation applied. Section 7.2 discusses the results of the measurements and how they compare to that expected for the three effects mentioned.

7.1 General Results

Figure 7-1 shows the zero-conductance region of the I-V curves for sample #9 at low temperatures, in the superconducting state, for four different ac power levels at 500 MHz.¹ The power level is defined as the output power of the ac source, a Hewlett-Packard 8341B synthesized sweeper. This power is attenuated 25 dB by fixed

¹For these curves, the mixing chamber thermometer measures temperatures below 50 mK. However, the sample temperature may be greater. See the following discussion and Sec. 3.4.

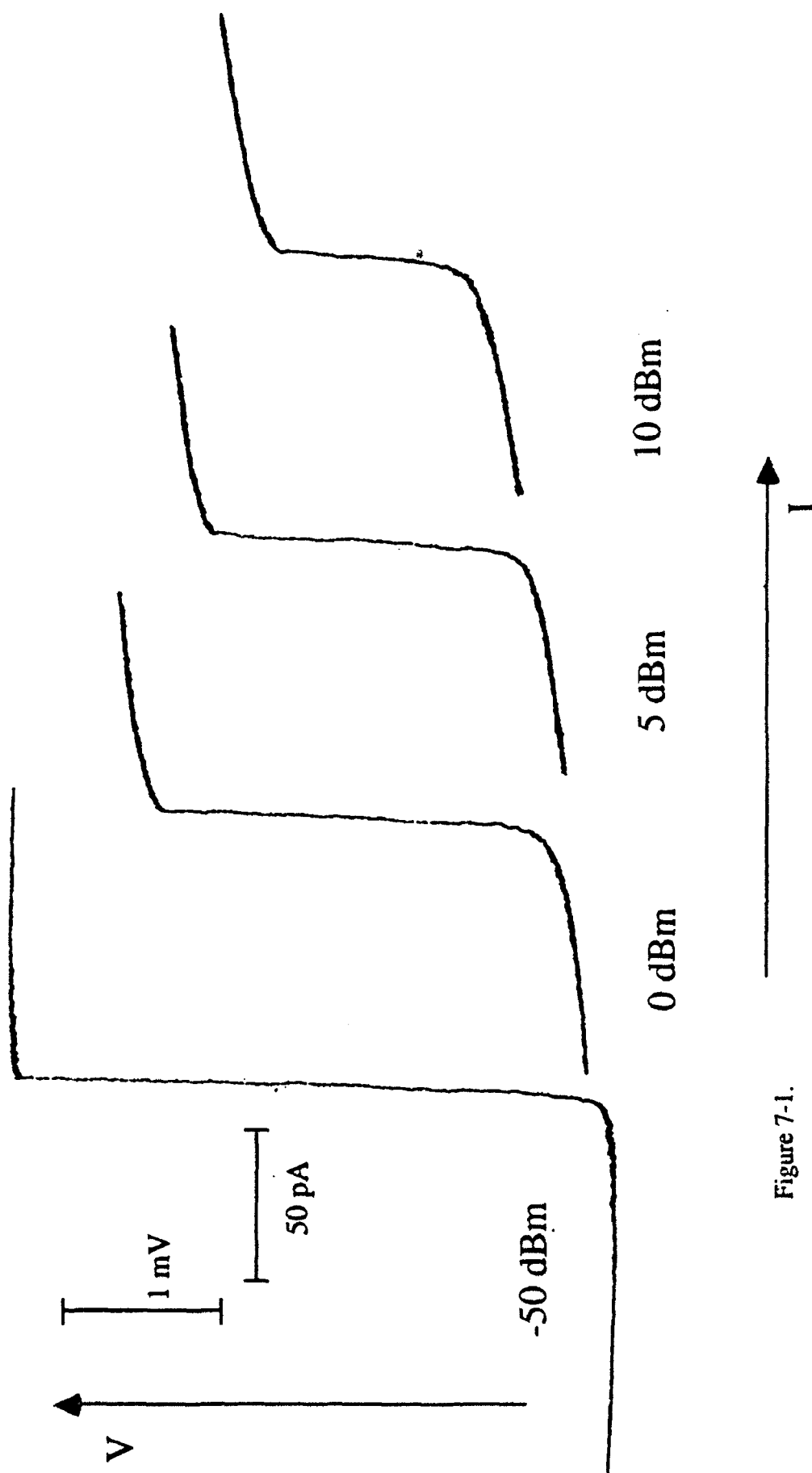


Figure 7-1.

I-V curves for sample #9 at a temperature of $T < 300$ mK (the zero bias point is in the center of the Coulomb blockade region). The four curves are for different powers of microwave radiation at a frequency of 500 MHz. Here we see that the threshold voltage is reduced at the higher microwave powers. (Within each curve, the asymmetry of the sharp corners is caused by sweeping the bias current slightly too fast. For the curves in this figure, the sweep direction is to the right).

attenuators, and an additional amount due to line losses and reflections. As discussed in Appendix B, which treats the subject of line losses, it is extremely difficult to determine the actual microwave power reaching the sample, especially at frequencies above 1 GHz. Except for studying the sample response at $\nu = 662$ MHz (Fig. 7-6), we will not attempt to estimate this power.

With the -50 dBm curve, the power level is small enough to represent zero applied power. From our data, the microwaves at this frequency do not appear to affect the I-V curves until power levels above about -20 dBm. We use very low powers to approximate zero power because to measure the I-V curves with zero power, we must disconnect or turn off the microwave source, which may produce transient voltage spikes large enough to damage the junctions. As we increase the microwave power to 0, 5 and 10 dBm, the threshold voltage V_t is reduced, and we measure a slight conductance for $V < V_t$. This slight conductance may be due to heating effects: the value measured for the 10 dBm curve corresponds to an unirradiated sample temperature of 250 mK. However, this simple heating argument is not entirely satisfactory, as the conductance for the 0 dBm curve corresponds to an unirradiated sample temperature of 240 mK, only slightly less than that at *ten* times the microwave power. Though we do not fully understand the microwave heating of the sample, it appears that the reduction of V_t cannot be explained by simple heating effects; measuring the temperature dependence of V_t , without microwaves, we find it to largely be insensitive to temperature below 500 mK (see the lower inset in Fig. 7-2), or specifically $V_t|_{T=250\text{mK}} \approx V_t|_{T=50\text{mK}}$.

In Fig. 7-2, we see that the microwave irradiation not only reduces V_t ,¹ but also shifts the entire I-V curve, on this scale, to lower voltages. We refer to this voltage shift as ΔV , which is a function of current. The sign of ΔV is such that a shift to lower voltages, as we get by increasing the microwave power, is represented by a positive value of ΔV . These four curves are taken at power levels of -80, -15, -5, and 3 dBm with a microwave

¹Note that the sharp edges in Fig. 7-1 are not visible on this scale.

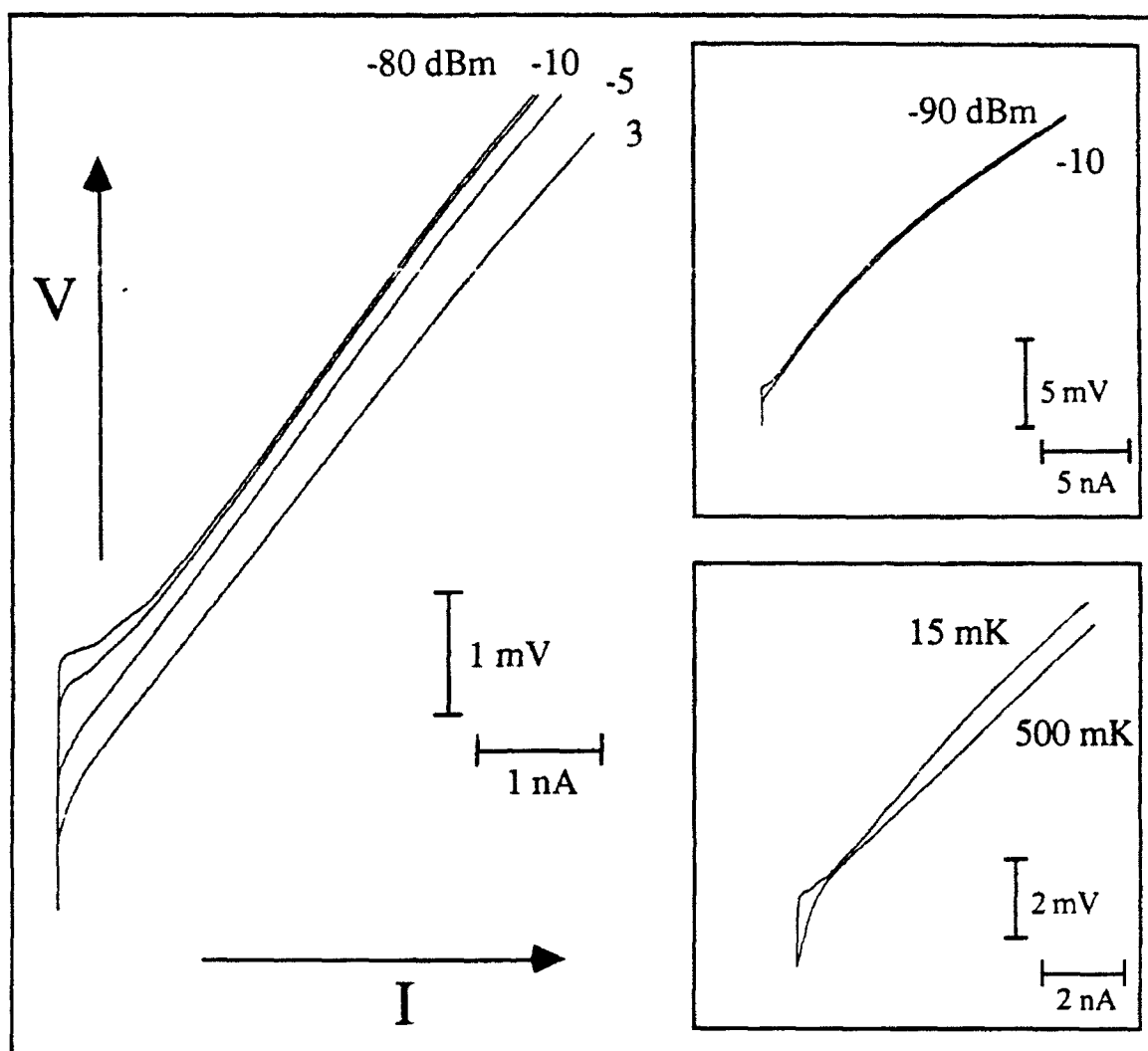


Figure 7-2.

I-V curves in the superconducting state for sample #9 with applied microwaves ($\nu = 6.200$ GHz for the main figure and 2.963 GHz for the upper inset) for different power levels. The curves in the upper inset are plotted at a larger scale. For the main curves and the upper inset, the mixing chamber sample is $T < 50$ mK. In the lower inset, we see two I-V curves, with *no applied microwaves*, at different temperatures. The shift ΔV with microwave power does not appear to have the same signature as simple heating, which tends to wash out the blockade region, but does not systematically shift the linear part of the I-V curve above the threshold voltage.

frequency of 6.200 GHz at $T < 50$ mK (for the rest of this chapter, all temperatures refer to the mixing chamber temperature of the dilution refrigerator).¹ We take the -80 dBm curve to approximate zero applied power, as described above. The curves in the upper inset, at an even more expanded scale, are taken at a frequency of 2.963 GHz, at 2 power levels, -90 and -10 dBm. The lower inset shows I-V curves without any applied microwaves, taken at temperatures of 15 and 500 mK. We include these two curves to show the effects of a simple temperature increase which smears out the blockade region without appearing to reduce the threshold voltage (which at higher temperatures we define as the "knee" in the I-V curve).

Figure 7-3 shows results in the *normal* state: four I-V curves with power levels of -50, -10, -5, and 0 dBm, taken at a frequency of 662 MHz and at $T < 50$ mK. Again, we take the curve at -50 dBm to approximate zero applied power. Unlike the superconducting state, at the higher microwave powers the sharp onset of current, used to define V_t , becomes washed out. Therefore, V_t does not have a unique definition in this case. However, as with the superconducting state, the I-V curves show an increasing shift in voltage ΔV as the microwave power is increased.

This shift ΔV , seen in both the normal and superconducting states, does not persist to all currents, however. For large enough currents, the I-V curves at the higher microwave powers asymptotically approach the zero-power curve. In the normal state at a temperature of $T < 50$ mK, we have to apply currents on the order of milliamps to see this. However, at higher temperatures the I-V curves reach the asymptotic form at much lower current levels. Figure 7-4 shows three I-V curves in the superconducting state at a temperature of $T \approx 300$ mK, at power levels of -50, -30, and -20 dBm and a frequency of 1 GHz. Here we again see the reduction of the threshold voltage V_t at zero current. However, the two higher power curves quickly approach the -50 dBm curve.

We display the frequency dependence of the voltage shift in Fig. 7-5. (For this figure

¹For Fig. 7-4 only, temperatures refer to the ³He pot temperature of the helium-3 refrigerator.

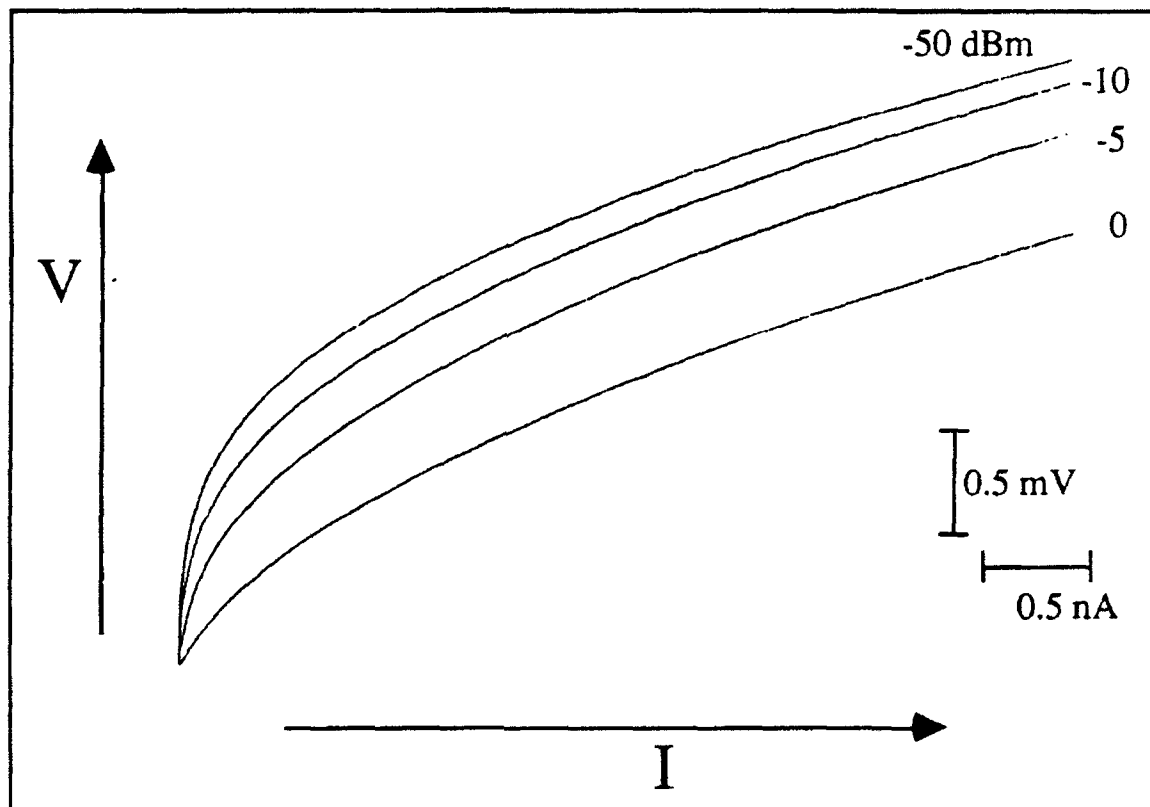


Figure 7-3.

I-V curves for sample #9 in the *normal* state with applied microwaves ($\nu = 662$ MHz) for four different power levels. The mixing chamber temperature is $T < 50$ mK.

only, we measure the shift in *current* for a fixed voltage as described below. For the bias voltage we use, ΔI should be roughly proportional to ΔV .) To obtain this plot, we bias the array with a fixed voltage $V_{bias} > V_t$, fix the microwave source output power level, sweep the frequency, and measure the current. An increased current represents an increased ΔV . Curves (a) - (c) in Fig. 7-5 show the current response in the superconducting state at $T < 50$ mK, for different frequency ranges, from 10 MHz to 20 GHz. Curve (d) shows the response in the normal state at $T < 50$ mK, from 10 MHz to 10 GHz.

The response of the current appears to be in the form of peaks. Three prominent peaks in both the normal and superconducting states occur at frequencies of 662 MHz, 2.963

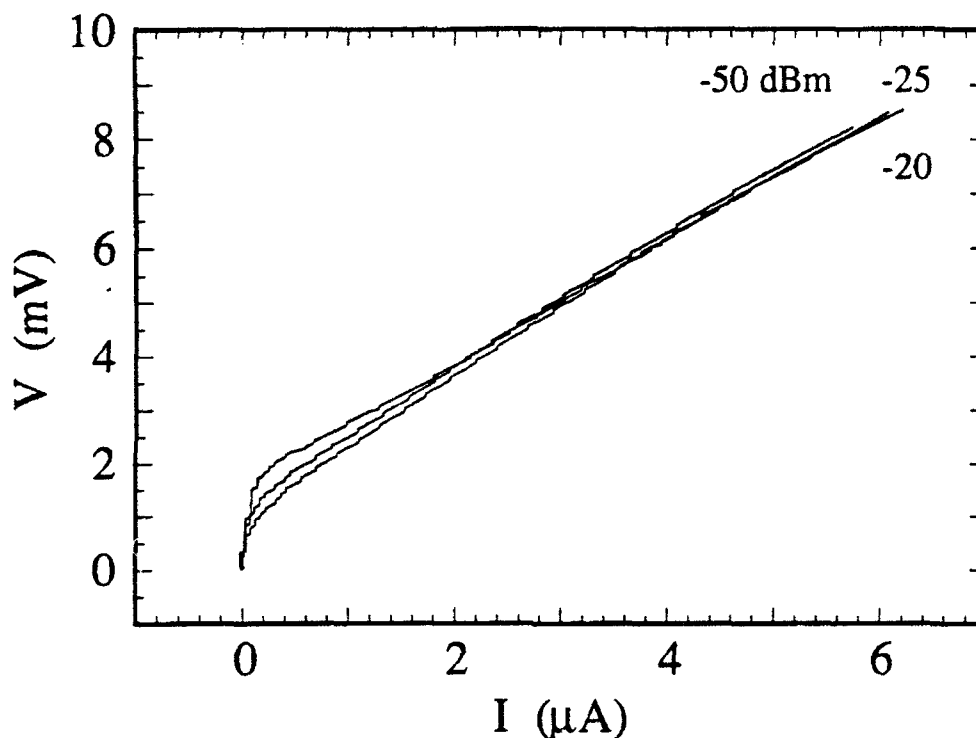


Figure 7-4.

I-V curves for sample #9 in the superconducting state for applied microwaves (1 GHz) at three different power levels. Measured in the helium-3 refrigerator, the ^3He pot temperature is $T = 300$ mK. The step-like nature of the curves at a fine scale is an artifact of the method of digitizing the data.

GHz, and 6.200 GHz, which is why these frequencies were used in Figs. 7-2 and 7-3. As we are not aware of any theory which predicts such a non-monotonic, intrinsic dependence on frequency, a more suitable interpretation may be that the peaks are due to resonances in the microwave injection set-up. Peaks may represent frequencies where the transmission of microwaves to the sample is high, while dips or regions of low ΔI may represent frequencies at which the microwaves are largely reflected and do not reach the sample. Because of this possible interpretation of the traces in Fig. 7-5, it is difficult to make any determination of the array's response to microwaves as a function of frequency.

To look into the nature of the shift in voltage ΔV , we can study it as a function of the

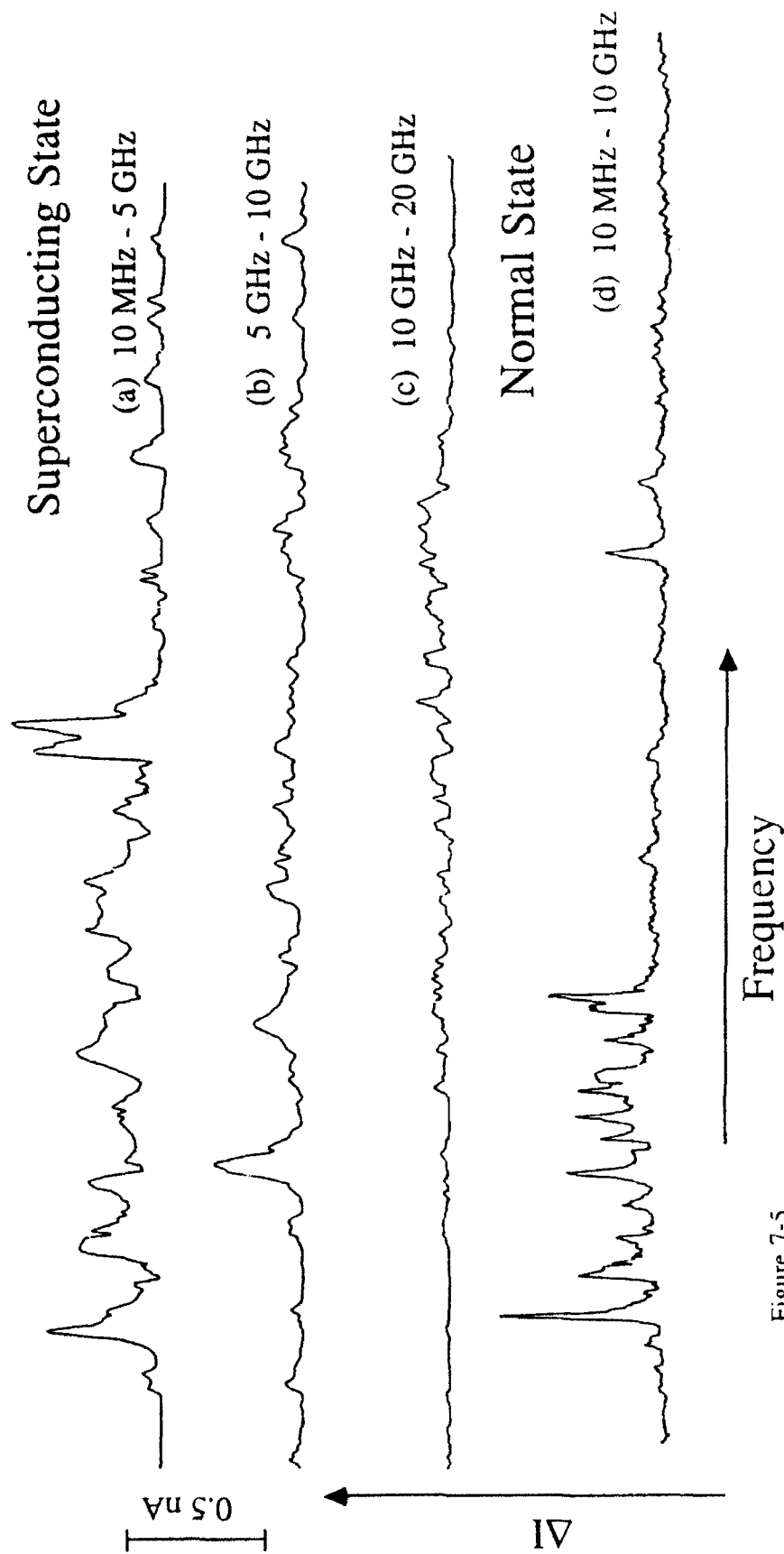


Figure 7-5.

Change in measured current vs. microwave frequency (linear scale) at a fixed voltage bias and a fixed microwave output power level. Curves (a) - (c) are for different frequency ranges in the superconducting state. The data in curve (d) is taken in the normal state.

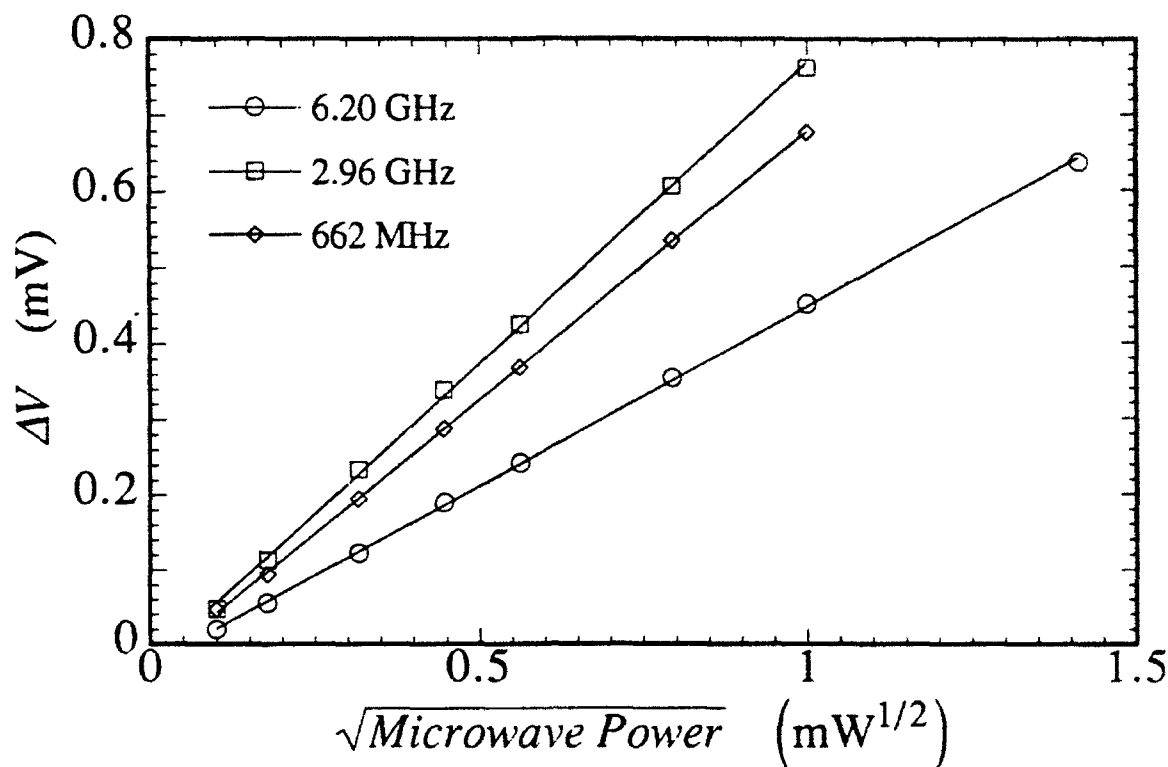


Figure 7-6.

For sample #9 in the superconducting state, we see the shift in voltage measured at a constant current, $I^*(1.5V_I)$, as a function of the square root of the microwave power level (at the source) for three different frequencies. The mixing chamber temperature is $T < 50$ mK. The straight lines are "least-square" fits to the data.

microwave power. First, though we need to quantify this shift as it is a function of current. Let $I^*(V)$ represent the current as a function of voltage with *no applied microwaves*. We then define ΔV at this current, $\Delta V|_{I^*(V)}$. Figure 7-6 shows $\Delta V|_{I^*(1.5V_I)}$ vs. the square root of the power at three different frequencies, 662 MHz, 2.963 GHz, and 6.200 GHz, for sample #9 in the superconducting state. The data fall on straight lines, which suggests that the shift in voltage is proportional to the *amplitude* of the ac signal. The relative slopes of the curves most likely have to do with the relative fraction of the nominal microwave power which reaches the sample. Of the three curves, the slope is largest for 2.963 GHz, which from Figs. 7-5(a) and (b) we see is the highest peak of the

three (in the superconducting state). The curve for 6.200 GHz has the lowest slope, and correspondingly the smallest peak.

As we do not know the actual microwave power reaching the sample, in Fig. 7-6 we define the power as the output power of the microwave source. It is difficult to even estimate the power reaching the sample, with the difficulty increasing with increasing frequency. However, as discussed in Appendix B, for the 662 MHz data we *have* attempted to make an order of magnitude estimation (the line loss data presented in Appendix B does not show any resonant peaks at $\nu = 662$ MHz, as does the data in Fig. 7-5, which increases the uncertainties in this value): the signal is attenuated 25 dB from the fixed attenuators and ~ 10 dB from line losses and reflections for a total of ~ 35 dB attenuation. Assuming the coax to have a line impedance of $50\ \Omega$, 1 mW of output power corresponds to an rms voltage at the sample of ~ 4 mV, larger than the measured ΔV at this frequency and output power, ~ 0.7 mV.

The linearity of the data seen in Fig. 7-6 depends on the current level, $I^*(V)$. For currents taken at voltages just above V_t we do not get a linear relation. At higher currents we also lose linearity, though only slightly. Figure 7-7 shows ΔV vs. microwave power for two different current levels, $I^*(1.5 V_t)$ and $I^*(2.25 V_t)$. The curve for $2.25 V_t$ does not appear to be as linear as that for $1.5 V_t$, rounding off somewhat at the lower power levels.

Finally, we look at ΔV in the normal state. Figure 7-8 shows $\Delta V|_{I^*(2.5V_t)}$ in the normal state and $\Delta V|_{I^*(1.5V_t)}$ in the superconducting state at a frequency of 662 MHz.¹ Though we only have three data points in the normal state, they roughly fall on a straight line.² However, the straight line drawn through these three points does not extrapolate back to the origin, as one might expect if the dependence on \sqrt{P} has a physical

¹ We choose I^* at $2.5 V_t$ in the normal state because we wish to study ΔV in a region in which it is largely independent of current. Experimentally, in the superconducting state this region begins at voltages just below to $1.5 V_t$, while in the normal state we must go to somewhat higher voltages.

² At the time of the measurements, the importance of this data was not clear to us, and so we did not take more curves at different microwave powers.

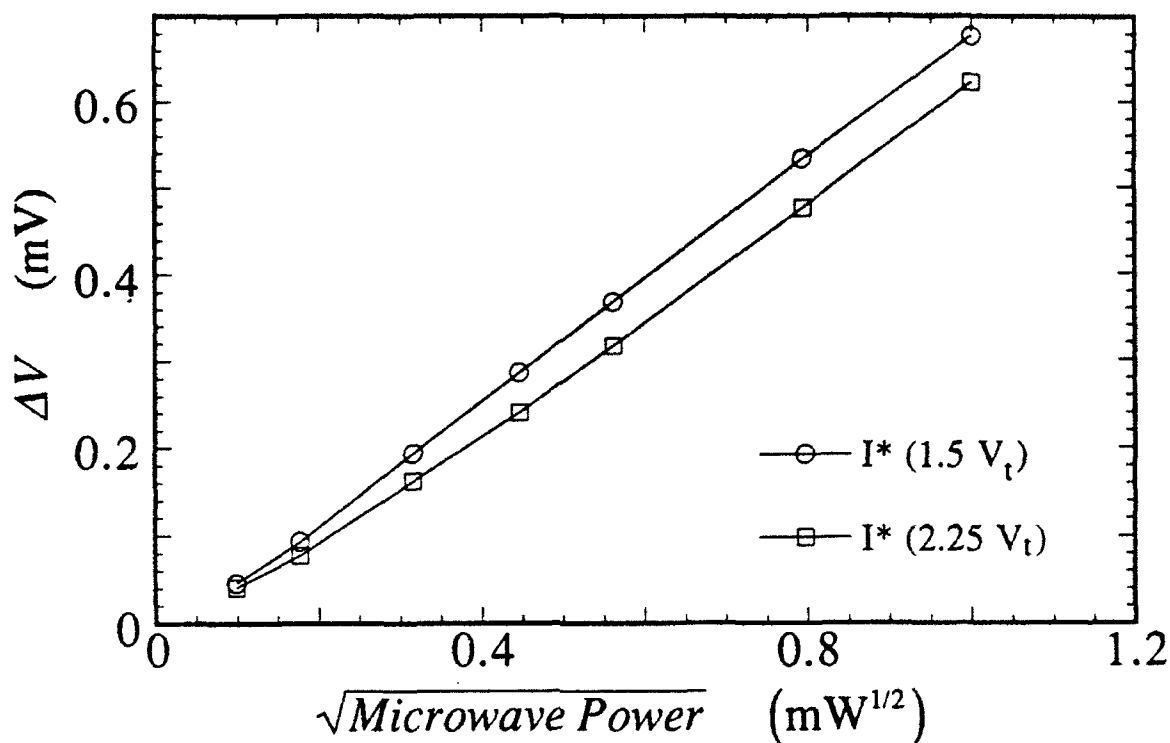


Figure 7-7.

Shift in voltage measured at two currents, $I^*(1.5 V_t)$ and $I^*(2.25 V_t)$, as a function of the square root of the microwave power level (at the source) for sample #9 in the superconducting state. The microwave frequency is 662 MHz, and the mixing chamber temperature is $T < 50$ mK. The straight lines simply connect the data points.

significance. The curve may begin to flatten out at the lower power levels, similar to that seen in the lower curve of Fig. 7-7.

7.2 Discussion of Results

We find the dependence of the I-V characteristics on applied microwaves to be a shift in voltage ΔV , with the amount of shift proportional to the *amplitude* of the ac signal. This behavior cannot be explained by three possible mechanisms we might expect to apply to this system; (a) simple averaging, (b) single-electron-tunneling (SET)

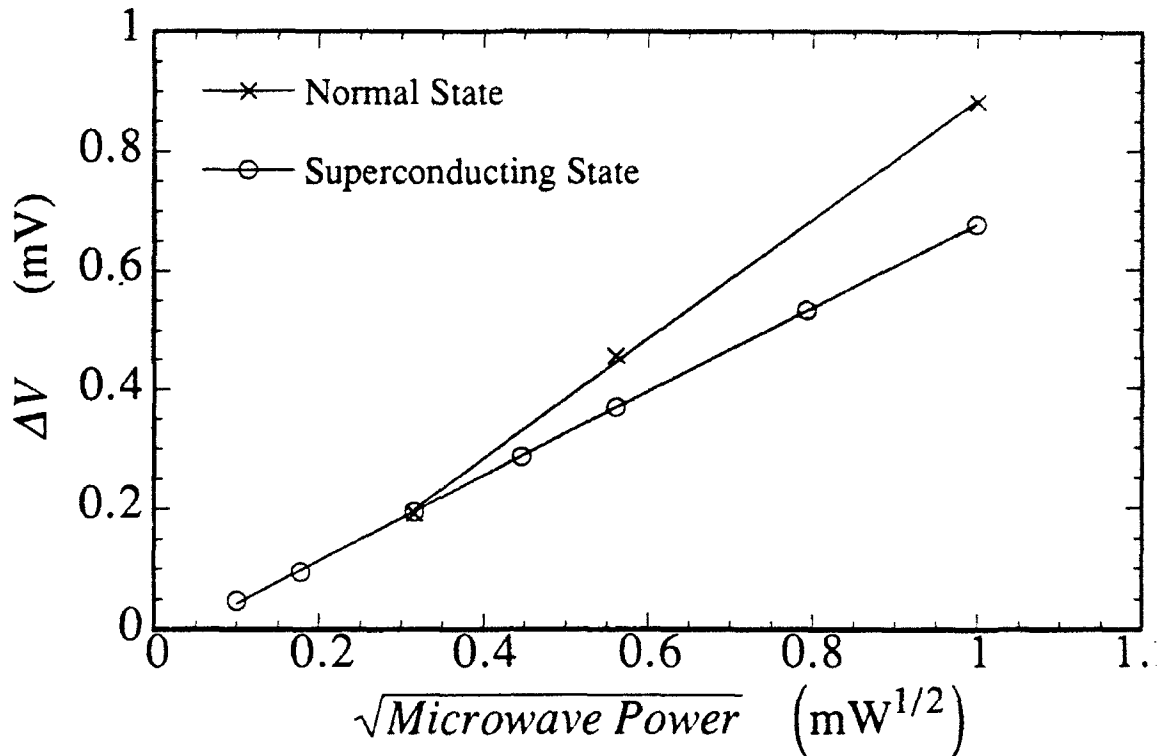


Figure 7-8.

For sample #9, shift in voltage at a specific current, $I^*(1.5V_I)$ in the superconducting state and $I^*(2.5V_I)$ in the normal state, vs. microwave power (at the source) at a frequency of $\nu = 662$ MHz. The mixing chamber temperature is $T < 50$ mK. The straight lines are "least square" fits to the data.

oscillations,¹ and (c) photon-assisted tunneling (PAT).² As we do not have an alternative explanation at this time, we will describe these effects as motivation for future discussion.

(a) Averaging. Averaging is the most straightforward of the three effects. With it, we treat of the array as being voltage biased,³ with an instantaneous voltage

$$V(V_{dc}, V_{ac}, \omega; t) = V_{dc} + V_{ac} \sin \omega t \quad (7.1)$$

¹See Averin and Likharev (1986), Delsing, et al. (1989b), Geigenmüller and Schön (1989) and Bakhvalov, et al. (1991).

²See Dayem and Martin (1962), Tien and Gordon (1963), and Danchi (1982).

³With the microwave injection set-up we use, the inner and outer conductors of the microwave coax are connected to the source *in parallel*. Therefore, with the ac and dc channels combined, we do not have either a strict current or voltage bias source. We performed these measurements with the dc portion of the circuit both nominally current and voltage biased, and found no difference in the I-V curves.

and assume that the instantaneous current, $I(V_{dc}, V_{ac}, \omega, t)$, is the same function of $V(t)$ as in the dc case. If the apparatus used to measure the current averages over a time longer than $2\pi/\omega$, however, it will measure an *average* current, $\bar{I}(V_{dc}, V_{ac}, \omega)$, where

$$\bar{I}(V_{dc}, V_{ac}, \omega) = \frac{\omega}{2\pi} \int_0^{2\pi/\omega} I(V_{dc}, V_{ac}, \omega; t) dt \quad (7.2)$$

In discussing our data, it is only necessary to concentrate on the limiting case where the dc current is linear in the dc voltage. In this case, the integral in Eqn. (7.2) of the sine term in Eqn. (7.1) gives zero. The current will be independent of V_{ac} and ω , i.e., $\bar{I}(V_{dc}) = I(V_{dc})$.

Our data do not show this form, however. From the above argument we would expect the I-V curves in Fig. 7-2 at different microwave powers (different but sufficiently small values of V_{ac}) *in the linear regions* to lie on top of one another.¹ However, we see instead a uniform shifting of the curves in both the linear and non-linear regions. Thus this type of averaging does not seem to explain our data.

(b) SET Oscillations. SET oscillations refers to periodic tunneling of electrons. Though different junction systems exhibit these oscillations, we initially concentrate on 1D arrays, where they have been observed by Delsing, *et al.* (1989b), with junctions similar to those in sample #9. Delsing, *et al.* measure this effect by voltage biasing their arrays with both dc and ac components (the frequencies range from 0.7 to 5 GHz). In their I-V curves, they measure slight plateaus in the current at values of

$$I = nev \quad (7.3)$$

¹ Although we do not know the actual microwave power reaching the sample, experimentally the width of the blockade region provides an upper bound to V_{ac} . If we measure a zero or low current region for voltages below V_I , then V_{ac} must be less than V_I . Otherwise, we would measure smearing of the blockade region; if V_{ac} exceeds V_I , then at an arbitrarily small dc bias, the currents generated do not average to zero.

where ν is the frequency of the ac signal and n is an integer. Different values of n correspond to the different plateaus. Experimentally, n is determined by the bias voltage, and Delsing, *et al.* see plateaus up to $n = 4$. On the n^{th} plateau, during every rf cycle ne electrons move into the array from one end and ne electrons move out of the array from the other end.

As a first approximation, a 2D array can be considered many 1D arrays in parallel. For sample #9, the number of "parallel 1D arrays" is $N = 50$. In this case, the currents from each 1D array, or column, add together to give

$$I = Nne\nu \quad (7.4)$$

However, there exist numerical and theoretical arguments as to why SET oscillations may be unobservable in 2D arrays. Geigenmüller and Schön (1989) performed numerical simulations in which they calculated the strength of SET oscillations as a function of array size. They studied 3 arrays, identical except for their sizes: 1×21 (a 1D array), 3×21 , and 7×21 . They found strong SET oscillations in the 1×21 array, but found the oscillations to weaken with increasing width. Bakhvalov, *et al.* (1991) performed similar simulations and reached the same results. They argue that in 2D arrays, the oscillations are weakened or unobservable because of differences in the current carrying channels, or columns. Columns close to the edge do not carry current as well as those in the middle of the array due to the strong soliton repulsion from the edges. Thus, different columns contribute unequally to the net current, and the SET oscillations become washed out.

In our measurements we do not reveal any current plateaus in the normal state at frequencies from 10 MHz to 20 GHz. In the superconducting state, Fig. 7-2 shows what does appear to be slight plateaus at low microwave power levels. However, the current values where these appear are independent of frequency, in contradiction with Eqn. (7.4), so they appear to be unrelated to SET oscillations.

(c) Photon-Assisted Tunneling. In discussing photon-assisted tunneling (PAT), we start by describing the case of a voltage-biased single Josephson junction. If we bias the junction just *below* $2\Delta/e$, Δ being the superconducting energy gap, theoretically no current flows at $T = 0$; Cooper pairs do not give a dc tunnel current for $V \neq 0$, and the bias does not supply enough energy to break them and create quasiparticles, which can tunnel and contribute to a current. However, if the junction is exposed to photons of angular frequency ω , dc current may flow if the energy supplied by the photon, $\hbar\omega$, added to that supplied by the bias, eV_{bias} , is enough to break a pair, i.e., $eV_{bias} + \hbar\omega \geq 2\Delta$.

Experimentally, this phenomena shows up in the I-V curves as steps in the current at voltages of

$$V_{bias} = (2\Delta - m\hbar\omega) / e \quad (7.5)$$

where m is an integer which describes the number of photons involved in breaking apart a Cooper pair: for $m = 2$, for example, a Cooper pair adsorbs two photons and an energy $2\hbar\omega$. In the experiment on PAT by Danchi (1982), steps were visible for $m = 0, 1$, and 2 .

We are not aware of any theory put forward to predict PAT in arrays of charging-effect-dominated junctions. However, we might envision a similar situation to that described above. For $V < V_t$, not enough energy is supplied by the voltage bias to create and pull apart soliton-antisoliton pairs. At low temperatures, where thermal energy does not significantly contribute, no current flows. Following a similar argument to that presented above, an absorbed photon would add enough energy to break apart the pair if the photon energy satisfied the inequality $eV_{bias} + \hbar\omega \geq eV_t$. We might then expect to measure current steps at voltage levels of

$$V_{bias} = V_t - m\hbar\omega / e \quad (7.6)$$

Experimentally, we look for these steps by applying microwaves with frequency 9.77 GHz and studying the region of the I-V curves just below V_I . At this frequency, $\hbar\omega/e = 6$ μ V, and is within the limits of our resolution. We do not measure any current steps other than that at V_I . In addition, although we do see a reduction of V_I with increasing microwave power in the superconducting state, the magnitude of this reduction is on the order of millivolts, much too large to be described by Eqn. (7.6), unless one takes m to be on the order of 100. While we cannot rule out processes involving large numbers of photons, it appears that the *simple* description of PAT, presented here and which gives rise to steps in the I-V curves, does not describe our data.

CHAPTER EIGHT

CONCLUSION AND SUGGESTIONS FOR FUTURE RESEARCH

In this thesis we have presented experimental results of measurements on ten 2D arrays of mesoscopic Josephson junctions. The junctions which form these arrays are typically characterized by two energies, the Josephson energy E_J and the charging energy E_C . The I-V characteristics for an array in which one energy dominates are nearly opposite to that for arrays in which the other dominates: for $E_J \gg E_C$, the array shows superconducting behavior while for $E_C \gg E_J$, we measure insulating behavior instead. The symmetry between the two cases extends seemingly deeper. The excitations for the two cases, vortices and solitons, share many either identical or opposite properties. Table 8-1 gives a list of many of the dualities present for the two cases. These dualities are important in understanding the superconductor-to-insulator (S-I) transition. Although we did not study the S-I transition directly, we attempted to learn more about it by studying its details.

It is important to point out that this duality is broken in at least two ways: (1) with vortices in the superconducting arrays, the array unit cells act as a lattice of pinning sites with a pinning barrier of $\approx 0.199 E_J$; for solitons in charging arrays, far enough away from the array edges, no such pinning barriers exist; and (2) Fazio and Schön (1991) predict that spin-wave excitations, coherent oscillations of the island spin variables which propagate in a wave-like fashion in the superconducting arrays, do not have a counterpart in the charging arrays.

Some of our specific results are the following. In the superconducting case, we studied vortices and vortex motion in two new limits: (1) in arrays of junctions whose

Table 8-1. Comparison of properties of superconducting and charging arrays.

	Superconducting arrays	Charging arrays
well-defined variable	ϕ	Q
characteristic energy	$E_J \propto 1/R_n$	$E_c \propto 1/C$
zero-bias conduction	superconducting	insulating
zero-bias phenomenon	supercurrent branch	Coulomb blockade
excitation	vortex	soliton
excitation interaction potential	$U = \mu_{core} + 2\pi E_J \ln r$	$U = \mu_{core} + (E_c / \pi) \ln r$ <i>predicted</i>
excitation interaction with free edges edge electrodes	attract repel	repel attract
energy barrier to move from site to site (far away from edges)	$= 0.199 E_c$	0
excitation induced by	magnetic field	electric field <i>predicted</i>
existence of KTB transition	yes	<i>predicted</i>
existence of excitation commensurate lattices	yes	<i>predicted</i>
existence of spin wave excitations	yes	no
ac response of junctions	Shapiro steps	SET oscillations
ac response of arrays	"giant" Shapiro steps	"giant" SET oscillations <i>predicted</i>
applications of circuits made with junctions	voltage standard; SQUID magnetometer	current standard; SET transistor electrometer

oscillations are underdamped and (2) in arrays where the island phases ϕ_i have quantum fluctuations. With (1), the similarities between the single junction and vortex equations of motion led us to believe that the vortices might show underdamped motion as well. However, our measurements showed the vortex motion to be *overdamped* which led to the experimental discovery of a new damping mechanism for vortices, not present in single junctions. A moving vortex transfers energy to the junctions over which it travels in the form of "wake". Thus, even if the individual junctions have essentially zero damping, vortex motion will still be overdamped. With (2), we have preliminary experimental evidence of the macroscopic-quantum-tunneling (MQT) of vortices through the pinning barriers, a result of the quantum fluctuations in ϕ_i .

With the charging arrays ($E_c \gg E_J$), we studied soliton motion by looking at two properties; the threshold voltage V_t in the zero-temperature limit, and the conduction within the blockade region for nonzero temperatures. Our experimental values of the threshold voltage V_t , in both the normal and superconducting states, match reasonably well with a theoretical prediction by Bakhvalov, *et al.* (1991) [modified for the superconducting case by M. Tinkham (private communication)]. Random offset charges may account for the differences which do exist. For nonzero temperatures, our data show that instead of the predicted Kosterlitz-Thouless-Berezinskii (KTB) soliton-antisoliton unbinding transition, the pair formation and unbinding is better described by a simple thermal activation process with an activation barrier of $0.23 E_c$ in the normal state and $0.23 E_c + \Delta$ in the superconducting state. The values measured in the normal state match that measured by Mooij, *et al.* (1990), who find a barrier of $0.24 E_c$, and Delsing, *et al.* (1991), who measure $0.27 E_c$. These results are also consistent with the predicted values of $0.25 E_c$ in the normal state [Tighe, *et al.* (1993)] and $0.25 E_c + \Delta$ in the superconducting state [Simánek (1982)], though only if we neglect the soliton-antisoliton logarithmic interaction (possibly the result of screening by other pairs).

In regards to future work, the majority of unanswered questions lie in the regions of the transitional and charging arrays. The superconducting arrays are reasonably well-understood, with the possible exceptions of ballistic motion of vortices [van der Zant, *et al.* (1992b)] and the Aharonov-Casher (AC) effect, the magnetic analog of the Aharonov-Bohm effect (with the AC effect, it is theoretically predicted that one can measure the interference between two channels of vortices passing on opposite sides of an electric field).¹ There is still much insight to be gained from transitional arrays, however, as a systematic study of them is lacking. Of interest are the quantum mechanical effects, which are greatest in this region due to large quantum fluctuations in both ϕ and Q .

With the charging arrays many questions still remain open, as evidenced by the “*predicted*” notations in Table 8-1. For example, while we have shown that our data does not fit the KTB transition, we cannot rule out the possibility that the KTB model may apply to other charging arrays, with different values of parameters such as C_ϕ/C and array size. Also yet to be determined is whether solitons can be induced into the array with an applied electric field (similar to how vortices are induced with an applied magnetic field). If so, then it may be possible to form lattices of solitons commensurate with the array lattice. The existence of soliton lattices would open up the possibility of measuring “giant” SET oscillations: every rf cycle the entire lattice would shift by one unit cell.

In addition, with regards to soliton motion it is not entirely satisfactory that we must neglect the logarithmic interaction in order to get a theoretical activation barrier of $0.25 E_C$. A numerical study of this system, as outlined in Chapter 6, might be useful in addressing this point, as it can include such effects as random offset charges and stray capacitances.

¹ See Aharonov and Bohm (1959), and Aharonov and Casher (1984).

REFERENCES

- Aharonov, Y., and D. Bohm, Phys. Rev. B **3**, 485 (1959).
- Aharonov, Y., and A. Casher, Phys. Rev. Lett. **53**, 319 (1984).
- Ambegaokar, V., and A. Baratoff, Phys. Rev. Lett. **10**, 486 (1963).
- Averin, D. V., and K. K. Likharev, in *Mesoscopic Phenomena in Solids*, edited by B. L. Altshuler, P. A. Lee, and R. A. Webb (North-Holland, Amsterdam, 1991).
- Bakhvalov, N. S., G. S. Kazacha, K. K. Likharev, and S. I. Serdyukova, Physica (Amsterdam) **173B**, 319 (1991).
- Bean, C. P., and J. D. Livingston, Phys. Rev. Lett. **12**, 14 (1964).
- Benz, S. P., Ph. D. Thesis, Harvard University (1990).
- Benz, S. P., M. S. Rzchowski, M. Tinkham, and C. J. Lobb, Phys. Rev. Lett. **64**, 693 (1990).
- Berezinskii, V. L., Zh. Eksp. Teor. Fiz. **59**, 907 (1970) [Sov. Phys. JETP **32**, 493 (1971)].
- Bobbert, P. A., Phys. Rev. B **45**, 7540 (1992).
- Caldeira, A. O., and A. J. Leggett, Ann. Phys. (N.Y.) **149**, 374 (1983).
- Caldeira, A. O., and A. J. Leggett, Phys. Rev. Lett. **46**, 211 (1981).
- Chen, C. D., P. Delsing, D. B. Haviland, and T. Claeson, Physica Scripta T **42**, 182 (1992).
- Cleland, A. N., J. M. Schmidt, and John Clarke, Phys. Rev. B **45**, 2950 (1992).
- Danchi, W. C., Ph. D. Thesis, Harvard University (1982).
- Dayem, A. H., and R. J. Martin, Phys. Rev. Lett. **8**, 246 (1962).
- Delsing, P., K. K. Likharev, L. S. Kuzmin, and T. Claeson, Phys. Rev. Lett. **63**, 1180 (1989a).
- Delsing, P., K. K. Likharev, L. S. Kuzmin, and T. Claeson, Phys. Rev. Lett. **63**, 1861 (1989b).

- Delsing, P., Chiidong Chen, D. B. Haviland, and T. Claeson in *Single Electron Tunneling and Mesoscopic Devices*, Eds. H. Koch and H. Lubbig, Springer, Berlin (1992).
- Delsing, P. in *Single Charge Tunneling: Coulomb Blockade Phenomena in Nanostructures*, Eds. H. Grabert and M. Devoret, Plenum, New York (1992).
- Dolan, G. J., Appl. Phys. Lett. **31**, 337 (1977).
- Dolan, G. J., R. E. Miller, R. A. Linke, T. G. Phillips, and D. P. Woody, IEEE Trans. Magn. **MAG-17**, 684 (1981).
- Eikmans, H., and J. E. van Himbergen, Phys. Rev. B **45**, 10597 (1992).
- Fazio, R., and G. Schön, Phys. Rev. B **43**, 5307 (1991).
- Fisher, M. P. A., Phys. Rev. Lett. **65**, 923 (1990).
- Fisher, Matthew P. A., G. Grinstein, and S. M. Girvin, Phys. Rev. Lett. **64**, 587 (1990).
- Fulton, T. A., and G. J. Dolan, Phys. Rev. Lett. **59**, 109 (1987).
- Geerligs, L. J., Ph. D. Thesis, Delft University of Technology (1990).
- Geerligs, L. J., M. Peters, L. E. M. de Groot, A. Verbruggen, and J. E. Mooij, Phys. Rev. Lett. **63**, 326 (1989).
- Geigenmüller, U., and G. Schön, Europhys. Lett. **10**, 765 (1989).
- Geigenmüller, U., C. J. Lobb, and C. B. Whan, Phys. Rev. B **47**, 348 (1992).
- Grabert, H., P. Olschowski, and U. Weiss, Phys. Rev. B **36**, 1931 (1987).
- Granato, E., and J. M. Kosterlitz, Phys. Rev. Lett. **65**, 1267 (1990).
- Hanna, A. E., Ph. D. Thesis, Harvard University (1992).
- Haviland, D. B., Y. Liu, and A. M. Goldman, Phys. Rev. Lett. **62**, 2180 (1989).
- Hu, E. L., L. D. Jackel, and R. E. Howard, IEEE Trans. on Electron Dev., **ED-28**, 1382 (1981).
- Iansiti, M., Ph. D. Thesis, Harvard University (1988).
- Iansiti, M., M. Tinkham, A. T. Johnson, Walter F. Smith, and C. J. Lobb, Phys. Rev. B **39**, 6465 (1989a).

- Iansiti, M., A. T. Johnson, C. J. Lobb, and M. Tinkham, Phys. Rev. B **40**, 11370 (1989b).
- Ivanchenko, Y. M., and L. A. Zil'berman, Zh. Eksp. Teor. Fiz. **55**, 2395 (1968) [Sov. Phys. JETP **28**, 1272 (1969)].
- Johnson, A. T., Ph. D. Thesis, Harvard University (1990).
- Johnson, A. T., C. J. Lobb, and M. Tinkham, Phys. Rev. Lett. **65**, 1263 (1990); Phys. Rev. Lett. **65**, 2613(E) (1990).
- Knorr, K., and J. D. Leslie, Solid State Communications **12**, 615 (1973).
- Kosterlitz, J. M., and D. J. Thouless, J. Phys. C **6**, 1181 (1973).
- Kuzmin, L. S., P. Delsing, T. Claeson, and K. K. Likharev, Phys. Rev. Lett. **62**, 2539 (1989).
- LaFarge, P., H. Pothier, E. R. Williams, D. Esteve, C. Urbina, and M. H. Devoret, Z. für Physik B **85**, 327 (1991).
- Li, Q., C. H. Watson, R. G. Goodrich, D. G. Haase, and H. Lukefahr, Cryogenics **26**, 467 (1986).
- Lichtenberger, A. W., C. P. McClay, R. J. Mattauch, and M. J. Feldman, IEEE Trans. MAG-25, 1247 (1989).
- Lobb, C. J., David W. Abraham, and M. Tinkham, Phys. Rev. B **27**, 150 (1983).
- Louanasmaa, O. V., *Experimental Principles and Methods below 1K*, Academic Press, London (1974).
- Martinis, John M., and R. L. Kautz, Phys. Rev. Lett. **63**, 1507 (1989).
- Martinis, J., M. Devoret, and J. Clarke, Phys. Rev. B **35**, 4682 (1987).
- McCumber, D. E., J. Appl. Phys. **42**, 3113 (1968).
- Mooij, J. E., B. J. van Wees, L. J. Geerligs, M. Peters, R. Fazio, and G. Schön, Phys. Rev. Lett. **65**, 645 (1990).
- Octavio, M., C. B. Whan, U. Geigenmüller, and C. J. Lobb, Phys. Rev. B **47**, 1141 (1993).
- Nakajima, K., and Y. Sawada, J. Appl. Phys. **52**, 5732 (1981).

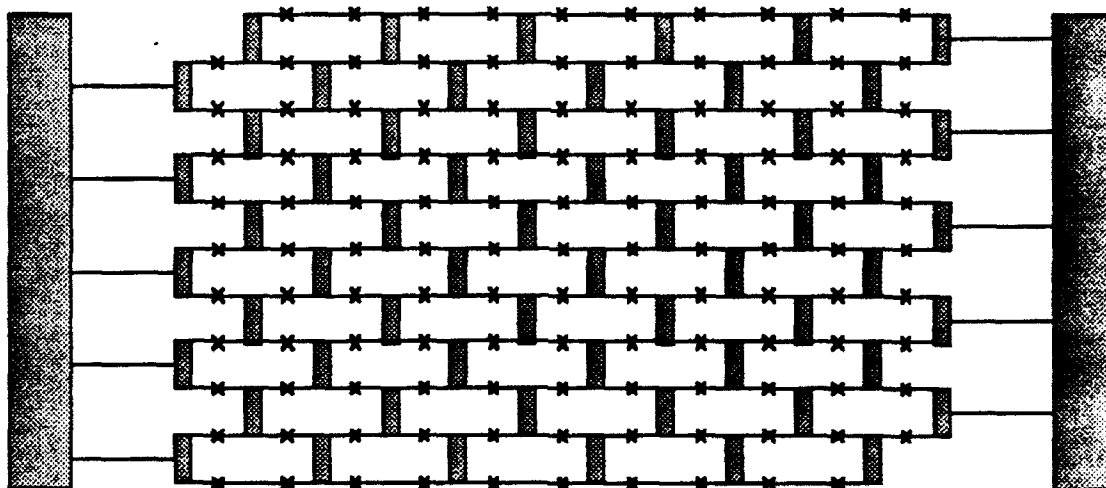
- Richardson, R. C., and E. N. Smith, eds., *Experimental Techniques in Condensed Matter Physics at Low Temperatures*, Addison-Wesley, New York (1988).
- Rzchowski, M. S., S. P. Benz, M. Tinkham, and C. J. Lobb, Phys. Rev. B **42**, 2041 (1990).
- Simánek, E., Phys. Rev. B **25**, 237 (1982).
- Smith, Walter F., Ph. D. Thesis, Harvard University (1989).
- Smith, W. F., T. S. Tighe, G. C. Spal ling, M. Tinkham, and C. J. Lobb, Phys. Rev. B **43**, 12267 (1991).
- Sohn, L. L., M. S. Rzchowski, J. U. Free, S. P. Benz, and M. Tinkham, Phys. Rev. B **44**, 925 (1991).
- Stewart, W. C., Appl. Phys. Lett. **12**, 277 (1968).
- Tien, P. K., and J. P. Gordon, Phys. Rev. **129**, 647 (1963).
- Tighe, T. S., A. T. Johnson, and M. Tinkham, Phys. Rev. B **44**, 10286 (1991).
- Tighe, T. S., M. T. Tuominen, J. M. Hergenrother, and M. Tinkham, Phys. Rev. B **47**, 1145 (1993).
- Tinkham, M., *Introduction to Superconductivity*, McGraw-Hill, New York (1975); reprinted by Krieger, Florida (1985).
- Tuominen, M. T., J. M. Hergenrother, T. S. Tighe, and M. Tinkham, Phys. Rev. Lett. **69**, 1997 (1992).
- van der Zant, H. S. J., C. J. Muller, L. J. Geerligs, C. J. P. M. Harmans, and J. E. Mooij, Phys. Rev. B **38**, 5154 (1988).
- van der Zant, H. S. J., H. A. Rijken, and J. E. Mooij, J. Low Temp. Phys. **82**, 67 (1991a).
- van der Zant, H. S. J., F. C. Fritschy, T. P. Orlando, and J. E. Mooij, Phys. Rev. Lett. **66**, 2531 (1991b).
- van der Zant, H. S. J., Ph. D. Thesis, Delft University of Technology (1991).
- van der Zant, H. S. J., F. C. Fritschy, W. J. Elion, L. J. Geerligs, and J. E. Mooij, Phys. Rev. Lett. **69**, 2971 (1992a).

- van der Zant, H. S. J., F. C. Fritschy, T. P. Orlando, and J. E. Mooij, *Europhys. Lett.* **18**, 343 (1992b).
- van der Zant, H. S. J., L. J. Geerligs, and J. E. Mooij, *Europhys. Lett.* **19**, 541 (1992c).
- Van Duzer, T., and C. W. Turner, *Principles of Superconducting Devices and Circuits*, Elsevier, New York (1981).
- Washburn, Sean, and Richard A. Webb, *Advances in Physics* **35**, 375 (1986).
- Widom, A., and S. Badjou, *Phys. Rev. B* **37**, 7915 (1988).
- Yoshikawa, N., T. Akeyoshi, M. Kojima, and M. Sugahara, *Jpn. J. Appl. Phys.* **26**, 949 (1987).
- Zaikin, A. D., to appear in *Trieste Proceedings* (1991).

APPENDIX A

SCHEMATIC DRAWINGS OF DIAMOND ARRAYS

(a)



(b)

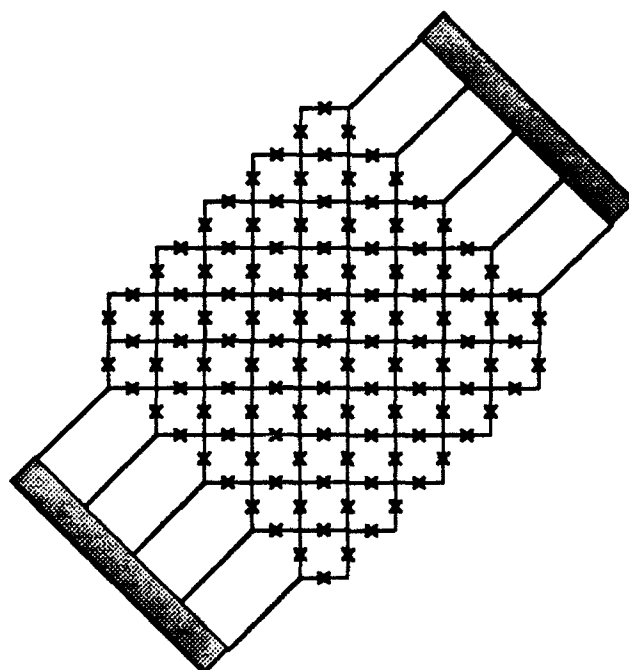


Figure A-1.

This figure gives two schematic drawings of the design and dimensions of samples #3, and #5, the "10 by 10 diamond" arrays. The top drawing (a) shows the array as fabricated, while the lower drawing (b) shows a more intuitive *electrically equivalent* configuration.

APPENDIX B

LINE LOSS IN MICROWAVE INJECTION SET-UP IN DILUTION REFRIGERATOR

In Chapter 7 we find it important to estimate the actual microwave power reaching the array. To do so requires a knowledge of the line losses and reflections of the microwave injection set-up. Figures B-1(a) and (b) show this set-up in detail (see also Fig. 3-13). As shown in (a), microwaves are generated by a source at the top of the dilution refrigerator. Traveling along coaxial cable, the microwaves pass through two fixed attenuators; a 15 dB attenuator thermally anchored to the 1K pot, and another 10 dB attenuator thermally anchored to the mixing chamber. The microwaves then pass through dc blocking capacitors, shown in both Figs. B-1(a) and (b). Figure B-1(b) shows the method of feeding the microwaves into the sample. From the blocking capacitors, the two microwave lines connect to the V+ and V- leads of the sample, which is mounted on a header. The microwaves then pass through thin-film gold pads on the header, and connect from the header pads to the sample pads by short sections of gold wire. The total length of *non*-coaxial conductors through which the microwaves must travel is roughly 2 inches.

To measure the losses we perform two experiments. First, we measure the line loss due to the coaxial cables and the fixed attenuators by measuring the throughput between the microwave source and testing point A, seen in Fig. B-1(a). Fixing the microwave output power, typically at 0 dBm, we sweep the frequency and record the transmitted power by the spectrum analyzer (Hewlett Packard 8562A, with frequency range 1 kHz -

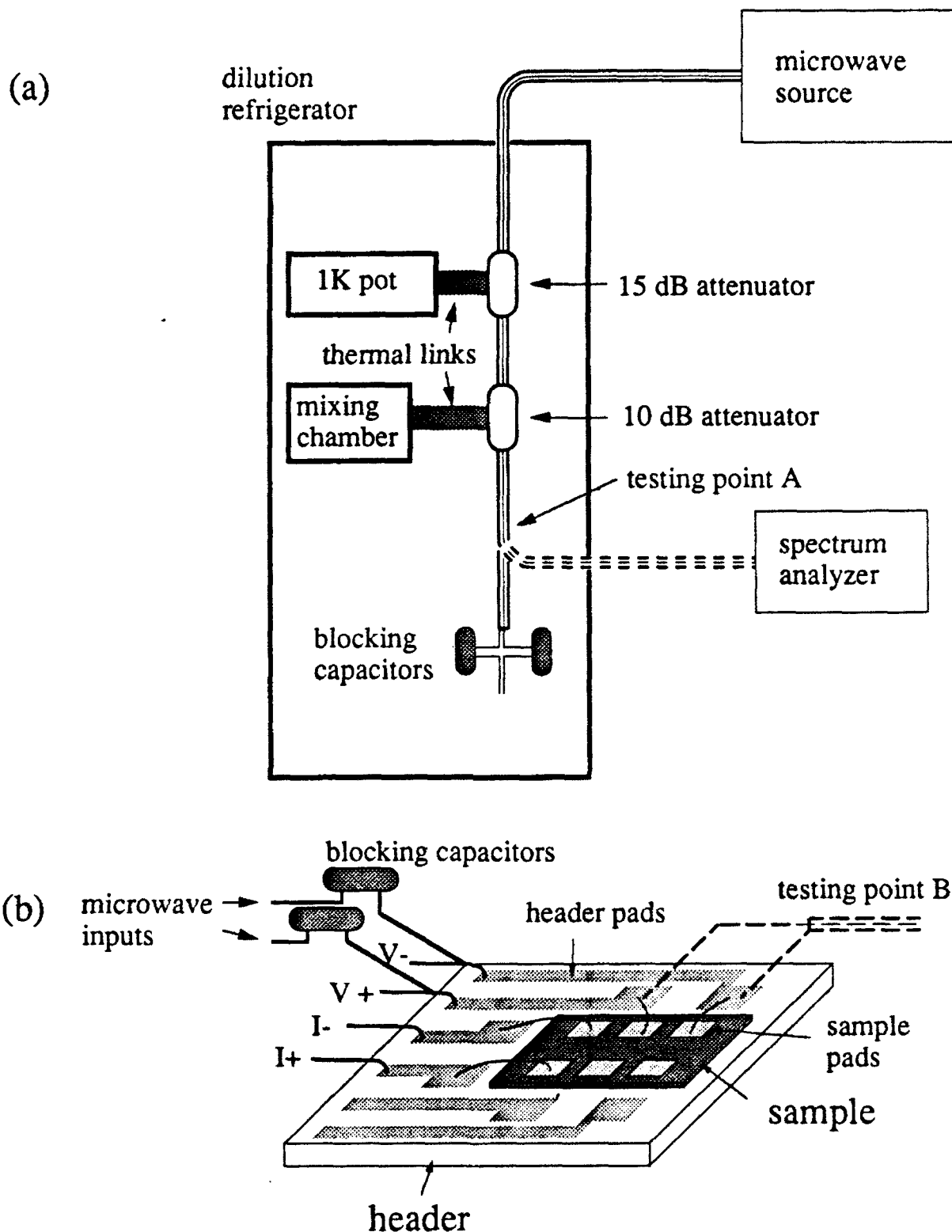


Figure B-1.

Schematic drawings of (a) the upper portion and (b) the lower portion of the microwave injection set-up. In (a), we show the path of the microwaves from the source at the top of the dilution refrigerator through the fixed attenuators to the blocking capacitors, as well as the position of testing point A (used only when the dilution refrigerator is opened up, allowing access). Drawing (b) shows the sample and the header on which the sample is mounted, as well as the wiring used to feed in the microwaves [the blocking capacitors are the same ones as in (a)]. Also shown is the location of testing point B.

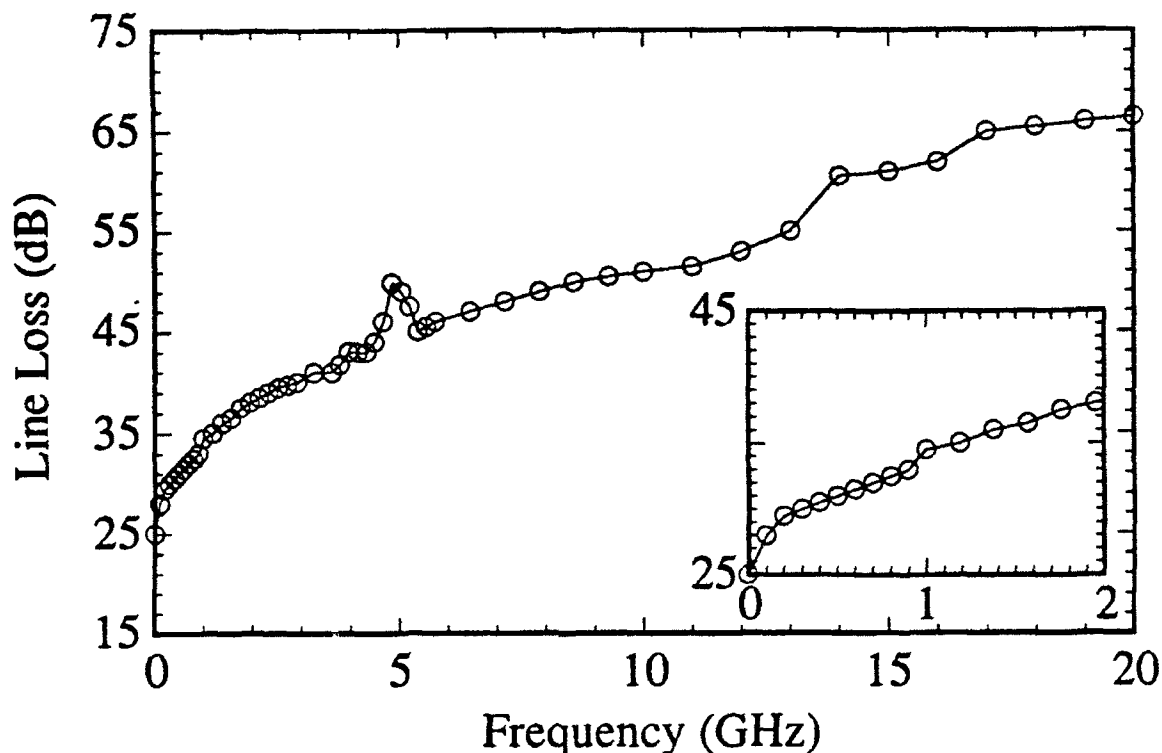


Figure B-2.

Measured loss of microwave power through the coaxial cables and the fixed attenuators vs. frequency. With the exception of a peak at 5 GHz, the loss shows a monotonic increase with increasing frequency. The inset shows an expanded view of data for frequencies below 2 GHz.

22 GHz).¹ The difference between the output power of the source and the measured power at testing point A gives the line losses due to absorption and the fixed attenuators. Figure B-2 shows this loss vs. the microwave frequency from 10 MHz to 20 GHz. With the exception of a peak at 5 GHz, the loss monotonically increases with increasing frequency. The inset shows an expansion of the results for frequencies below 2 GHz. This near-monotonic increase is markedly different from the response of the sample in the actual measurements, which as Fig. 7-5 shows, is in the form of a series of peaks.

¹In taking these measurements, we actually reverse the locations of the source and spectrum analyzer (physically lifting the source to the top of the refrigerator is a difficult task). The determination of the loss should not depend on the direction of the microwave transmission, however.

Therefore, the resonances which cause these peaks most likely do not come from this portion of the microwave injection set-up.

Next, we attempt to measure the losses from testing point A [Fig. B-1(a)] to testing point B [Fig. B-1(b)], where the microwaves travel through non-coaxial conductors. This will help determine the losses due to the blocking capacitors and the header wiring, though it will not give us the losses in the on-chip leads. Experimentally, we sweep the frequency for a fixed output power, and measure the transmitted power with a spectrum analyzer as before. The difference between the output and measured powers gives the losses. However, in this test experiment our results are complicated by the existence of *two* methods that the microwaves may travel from the source to the spectrum analyzer; by direct coupling as described above, and by radiative coupling, in which the signal is radiated from one portion of *unshielded* wiring and picked up by another.

Figure B-3 shows the losses from testing point A to testing point B for frequencies from 50 MHz to 20 GHz (the inset shows an expanded view of the results for frequencies below 1 GHz). We show data for both the direct and radiative coupling schemes. To measure the radiative coupling, we simply clip, right off of the header, the wire connecting the center pin of the source and analyzer coaxial cables and repeat the measurements as with the direct coupling. As described below, the radiative coupling is sensitive to the relative positions of the wires, coaxial cables, and header. In clipping the wire we attempt not to disturb anything else.

As Fig. B-3 shows, for frequencies below 1 GHz the losses with direct coupling are generally less than 10 dB, while the radiative coupling losses decrease from ~ 60 dB at 50 MHz to ~ 10 dB at 1 GHz. Above 1 GHz, the losses of the two coupling mechanisms generally increase, although they show a complicated pattern. From 1 to 10 GHz, the radiative losses are often on the order of or greater than the direct coupling losses, and above 10 GHz the two curves track together. This suggests that for these higher frequencies, the microwave transmission is dominated by radiative coupling. Therefore,

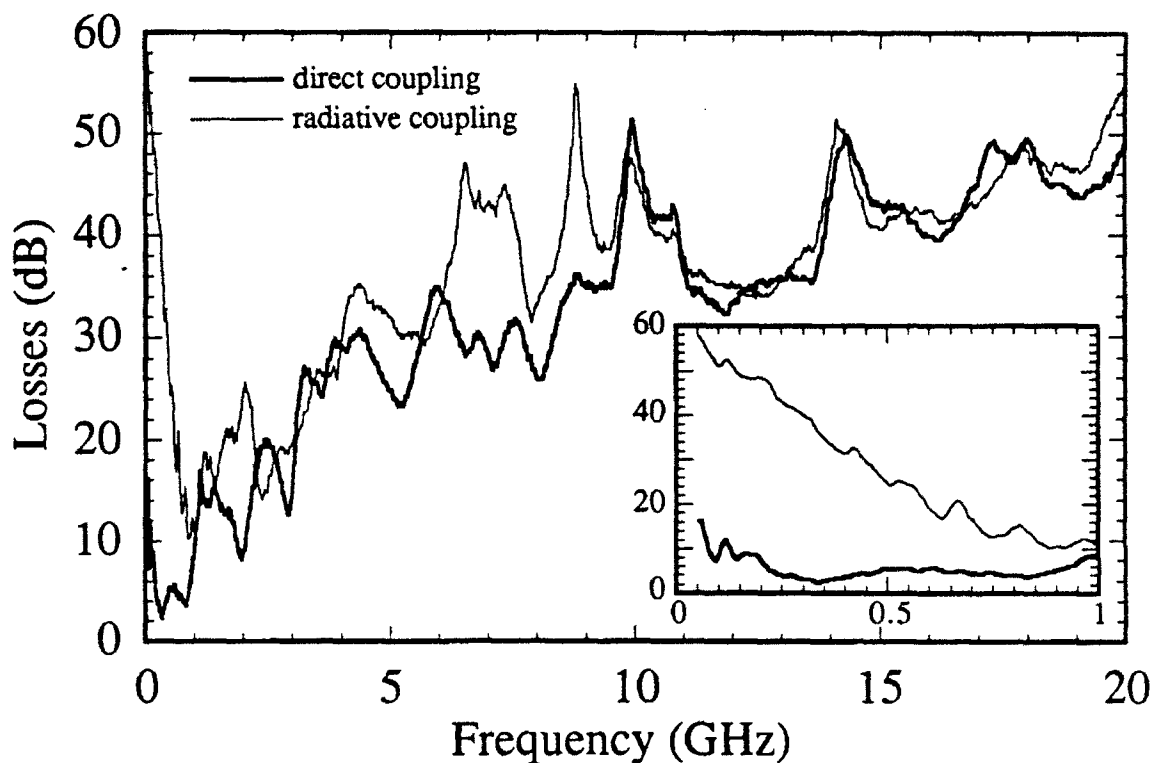


Figure B-3.

Losses from testing point A [Fig. B-1(a)] to testing point B [Fig. B-1(b)] as a function of frequency from 50 MHz to 20 GHz (the inset shows the results for frequencies under 1 GHz). The heavier and lighter lines represent the losses in the direct and radiative coupling schemes, respectively, as described in the text.

in this case we cannot make a good estimation of the direct coupling losses. For example, if the direct coupling losses at a frequency of 20 GHz were 100 dB, we would still measure ~ 50 dB because of the signal carried in the radiative channel. This suggests that in the actual experiments, the array may act as an antenna, being more influenced by the radiated microwaves than by those fed in through the leads.

The higher frequency data in Fig. B-3 are also difficult to interpret because different relative positions of the wires, header, and coaxial cables lead to different traces. For example, with direct coupling at a frequency of 6.2 GHz (the frequency used in Fig. 7-2), by moving the header to different positions we can change the losses from 25 to 40 dB.

This can be explained only if radiative coupling is the dominant mode of transmission. Such facts lead to large uncertainties when attempting to estimate the microwave power reaching the array in the actual experiments.

For frequencies below 1 GHz, however, it is possible to make a reasonable estimation of the power reaching the sample. As the inset in Fig. B-3 shows, at these frequencies direct coupling is the dominant mode of transmission. For example, at a frequency of 662 MHz, used in Fig. 7-3, the direct coupling losses are ~ 5 dB while that for radiative coupling are ~ 20 dB. We use this value of loss at 662 MHz, in addition with the ~ 30 dB of losses from the upper portion of the microwave injection set-up (Fig. B-2) for a total of ~ 35 dB in Chapter 7.

APPENDIX C

LIST OF NAMES USED TO IDENTIFY SAMPLES

Each of the ten samples discussed has at least two names; one used only in this thesis and a general name given at the time of measurement. In addition, different names are used in Tighe, *et al.* (1991) and Tighe, *et al.* (1993). For aid in cross-checking this thesis with raw data or the two references, we list all of the names used in Table C-1.

Table C-1. List of sample names used.

name used in thesis	general name	name in Tighe, <i>et al.</i> (1991)	name in Tighe, <i>et al.</i> (1993)
1	9		
2	11		
3	7		
4	13	A	
5	5		
6	14	B	
7	16		
8	18		1
9	17		2
10	19		3

ACKNOWLEDGMENTS

As with most every doctoral candidate, I have relied on the tremendous support of family, friends, and colleagues in finishing this degree program. First and foremost, I am grateful to my parents and family, whose unflagging support and prayers kept me motivated and with a positive attitude, and to my fiancée Melissa Allen, who provided me with a shining example by her commitment to excellence. Melissa and her family also share in the credit of making my time in Boston that much more enjoyable.

Professor M. Tinkham has been an excellent advisor for the past four years and I have greatly benefited as a physicist from working with him. Especially noteworthy are his management style of giving his students a large amount of freedom in choosing their pursuits and his habit of eating lunch with the group almost every day, allowing for easy accessibility--a rare gift in an advisor. I also had the privilege of working with Professor Chris Lobb, a delightful teacher, diligent experimentalist, and all-around good guy.

The older graduate students in the lab all contributed to my scientific growth. Walter Smith taught me almost everything I know about dilution refrigerators and fabrication techniques, as well as introduced me to the fields of Quantum Conductance Fluctuations and mesoscopic physics. Marco Iansiti got me interested in mesoscopic junction arrays, as well as tutored me in the basics of Josephson junctions which helped me pass my oral exam. I thank Charlie Johnson, another mentor and collaborator, for all of his guidance. I greatly benefited from our discussions on single junctions. In addition to many things, Sam Benz provided me, by example, with the vital advice that one not be afraid of machines or of tearing them apart to fix them. I thank Gabe Spalding and Li Ji, good friends and coworkers, for all of their help in initiating me into the group.

I am also indebted to the younger graduate students. Ashraf Hanna, scientist and entrepreneur extraordinaire, is a close friend and fellow, if sometimes unwilling, practical

joker. Our daily noontime stroll to Harvard Square always provided me with relief from the day's anxieties. I feel very fortunate to have overlapped with Lydia Sohn, who blessed us with her charm and unstoppable laughter and always kept us in dessert heaven. Niraj Anand is in many ways the model graduate student, and I regret not having him as an office mate. I have enjoyed the company of Rich Fitzgerald, the lab rf guy, who was of great help in making the microwave measurements. Jack Hergenrother has been a tremendous coworker and collaborator. I have learned much from his scientific attention to detail. Also, his amusing anecdotes and trivia were always welcomed at lunch-time. The lab's new additions, Chuck Black and Herb Shea, show promise of holding up the group's tradition of outstanding science and camaraderie.

In addition to the graduate students, several others have helped me greatly. Two postdocs, Mark Rzechowski and Mark Tuominen, have served as tremendous resources in designing experiments, making measurements, and interpreting the results. Their expertise and willingness to help has been invaluable. While writing this work, I appreciated the empathy of another postdoc, Mark Itzler, who just completed his thesis. Dave Carter has done an outstanding job managing the clean room, and deserves credit for the continual upgrading of the facilities and purchase of the large amount of new equipment. He has also been a good friend and sounding board to us all.

Several undergraduates have helped with the array project. Dave Ephron assisted in making the first arrays, as well as helping with several of the early measurements. Jiufeng Tu helped me greatly with the microwave measurements. Also, several people in the building have been of assistance. Tom Rosado and Matt Toomey in the stockroom have always been of great help, as have Yuan Lu and Clive Hayzelden in the microscopy lab. Elizabeth Hemingway has made all of our lives here a little more pleasant with her Thursday afternoon teas.

This research is supported in part by National Science Foundation Grant Nos. DMR-89-12927 and DMR-92-07956, Office of Naval Research Grant No. N00014-89-J-1565, and Joint Services Electronics Program Grant No. N00014-89-J-1023. I am also grateful for a National Defense Science and Engineering Graduate Fellowship.